

**DEVELOPMENT OF A PHYSICAL THEORY MODEL FOR THE
SIMULATION OF
HYSTERETIC BEHAVIOR OF STEEL BRACES**

**A THESIS SUBMITTED TO
THE GRADUATE SCHOOL OF NATURAL AND APPLIED SCIENCES
OF
MIDDLE EAST TECHNICAL UNIVERSITY**

BY

ERTUĞRUL EMRE ÇALIK

**IN PARTIAL FULFILLMENT OF THE REQUIREMENTS
FOR
THE DEGREE OF MASTER OF SCIENCE
IN
ENGINEERING SCIENCES**

APRIL 2007

Approval of the Graduate School of Natural and Applied Sciences

Prof. Dr. Canan Özgen
Director

I certify that this thesis satisfies all the requirements as a thesis for the degree of
Master of Science

Prof. Dr. Turgut Tokdemir
Head of Department

This is to certify that we have read this thesis and that in our opinion it is fully
adequate, in scope and quality, as a thesis for the degree of Master of Science.

Assoc. Prof. Dr. Murat Dicleli
Supervisor

Examining Committee Members

Prof. Dr. M.Ruşen GEÇİT (METU, ES) _____

Assoc. Prof. Dr. Murat DİCLELİ (METU, ES) _____

Prof. Dr. M.Polat SAKA (METU, ES) _____

Assoc. Prof. Dr. Cem TOPKAYA (METU, CE) _____

Assist. Prof. Dr. Ferhat AKGÜL (METU, ES) _____

I hereby declare that all information in this document has been obtained and presented in accordance with academic rules and ethical conduct. I also declare that, as required by these rules and conduct, I have fully cited and referenced all material and results that are not original to this work.

Name, Last name : Ertuğrul Emre ÇALIK

Signature :

ABSTRACT

DEVELOPMENT OF A PHYSICAL THEORY MODEL FOR THE SIMULATION OF HYSTERETIC BEHAVIOR OF STEEL BRACES

Çalık, Ertuğrul Emre

M.S., Department of Engineering Sciences

Supervisor: Assoc.Prof. Dr. Murat Dicleli

April 2007, 158 pages

Bracing members are considered to be effective earthquake-resistant elements as they improve the lateral strength and stiffness of the structural system and contribute to seismic energy dissipation by deforming inelastically during severe earthquake motions. However, the cyclic behavior of such bracing members is quite complex because it is influenced by both buckling and yielding.

This thesis presents simple but an efficient analytical model that can be used to simulate the inelastic cyclic behavior of steel braces. This model achieves realism and efficiency by combining analytical formulations with some semi-empirical formulas developed on the basis of a study of experimental data. A brace is idealized as a pin-pin ended member with a plastic hinge located at mid-length of a brace. Input parameters of the model are based on only material properties such as steel yield strength and modulus of elasticity as well as geometric properties including cross-sectional area, moment of inertia, etc. The obtained results are verified by the experimental and available analytical results.

Keywords: earthquake; inelastic buckling; cyclic load; steel brace;

ÖZ

ÇELİK ÇAPRAZ ELAMANLARIN DÖNGÜSEL YÜKLER ALTINDAKİ DAVRANIŞLARINI SİMULE EDEN TEORİK BİR MODEL

Çalık, Ertuğrul Emre

M.S., Mühendislik Bilimleri Bölümü

Danışman: Doç. Dr. Murat Dicleli

Nisan 2007, 158 sayfa

Çelik çapraz elemanlar, deprem esnasında enerji emen ve yapıya rijitlik ve dayanım sağlayan etkili elemanlardır. Ancak bu tür çapraz elemanlar basınç altında burkulmaya ve çekmede akmaya maruz kaldıklarından dolayı döngüsel yükler altında oldukça kompleks bir davranış gösterirler.

Bu çalışma, çelik çapraz elemanların elastik olmayan döngüsel davranışlarını simule edebilecek basit ama etkili bir analitik model sunmaktadır. Bu model analitik formüllerle beraber deneysel verilerden elde edilen yarı empirik formülleri birleştirerek gerçek davranışı yansıtır. Çapraz eleman iki ucu serbest olarak kabul edilir ve orta noktasında bir plastic mafsala sahiptir. Model için gerekli olan parametreler elemanın malzeme özelliklerinden (akma dayanımı, elastisite modülü vs.) ve geometrik özelliklerinden (kesit alanı, atalet momenti vs.) elde edilir. Bu model kullanılarak elde edilen sonuçlar deneysel sonuçlarla ve mevcut analitik modellerin sonuçlarıyla karşılaştırılarak doğrulanmıştır.

Keywords: deprem; elastik olmayan burkulma; döngüsel yük; çelik çapraz eleman;

ACKNOWLEDGMENTS

I would like to thank my supervisor Assoc.Prof.Dr. Murat Dicleli for his guidance, for his support and patience during the long hours of this study, despite all the unfortunate events that have occurred throughout the process.

I express my special thanks to Assoc.Prof.Dr. Hakan Tarman for sparing his time and his all help. I would also like to thank my dear colleagues Özge Erdemli, Erkan Doğan, Ali Sinan Dike, and Volkan İşbuğa for cooperation and friendship, and helping me in all the possible ways.

I would sincerely thank to Kani Şahin for his endless friendship, making my stay in ANKARA happy and memorable and being always right beside me.

I dedicate this dissertation to each and every member of my family who always offered their advice, love, care and support. My family's absolute unquestionable belief in me, have been a constant source of encouragement and have helped me achieve my goals.

TABLE OF CONTENTS

ABSTRACT.....	iv
ÖZ.....	v
ACKNOWLEDGMENTS.....	vi
TABLE OF CONTENTS.....	vii

CHAPTERS

1. INTRODUCTION.	1
1.1 Introduction.....	1
1.2 Background Information and Literature Review.....	3
1.2.1 Review of Experimental Research.....	3
1.2.1.1 Black et al. (1980).....	5
1.2.2 Review of Analytical Brace Hysteretic Models.....	6
1.2.2.1 Finite Element Model.....	6
1.2.2.2 Phenomenological Model.....	7
1.2.2.3 Physical Theory Model.	11
1.3 Research Objective and Scope.....	15
1.4 Thesis Outline.	15
2. BEHAVIOR OF BRACES.	17
2.1 Cyclic Axial Load Response.....	17
2.2.1 Definition of Hysteretic Zones.....	18
2.2.2 Baushinger Effect versus Behavior of Braces.....	20

2.2.3	Hysteretic Properties of Braces.....	22
2.2.3.1	Effect of Brace Slenderness.....	23
2.2.3.2	Effect of End Conditions.....	25
2.2.3.3	Effect of Section Shape.....	26
3.	DERIVATION OF MOMENT-AXIAL FORCE RELATIONSHIPS.....	28
3.1	Calculation of Reduced Plastic Moment Capacity due to axial Load.....	28
3.1.1	W Section.....	31
3.1.1.1	Axial Force Effect Confined within the Web Area.....	33
3.1.1.2	Axial Force Effect Penetrated into the Flanges.....	35
3.1.2	Structural T Section.....	38
3.1.3	Double Channel Section.....	40
3.1.3.1	Axial Force Effect Confined within the Web Area.....	41
3.1.3.2	Axial Force Effect Penetrated into the Flanges.....	44
3.1.4	Double Angle Section.....	47
3.1.5	Box Section.....	48
3.1.5.1	Axial Force Effect Confined within the Web Area.....	50
3.1.5.2	Axial Force Effect Penetrated into the Flanges.....	52
3.1.6	Pipe Section.....	55
3.2	Comparison of the Moment Axial Force Relationships.....	59
4.	ANALYTICAL SIMULATION OF HYSTERETIC BEHAVIOR OF STEEL BRACES.....	63
4.1	Proposed Analytical Model.....	63
4.1.1	Derivation of Brace Initial Eccentricity.....	64

4.2 Analytical Formulations.....	68
4.2.1 Zone 1.....	70
4.2.2 Zone 2.....	71
4.2.3 Brace Growth Effect.....	73
4.2.4 Zone 3.....	85
4.2.5 Zone 4.....	89
4.2.6 Zone 5.....	93
4.2.7 Zone 6.....	98
4.2.7.1 Formulation of the Tangent Modulus.....	100
5. COMPARISON OF ANALYTICAL AND EXPERIMENTAL RESULTS.....	109
5.1 Selection of the Braces for Verification Purposes.....	109
5.2 Experimental Displacement Histories Applied on the Braces.....	110
5.3 Comparison of Analytical and Experimental Results.....	110
5.3.1 Comparison of Hysteresis Loops.....	110
5.3.2 Comparison of the Hysteresis Envelopes.....	113
5.4 Comparison of the Proposed Analytical Model with the Available Models	113
6. CONCLUSIONS.....	146
REFERENCES.....	148
APPENDICES	
A. DATA USED FOR THE GENERATION OF GROWTH FACTOR AND MODULUS OF ELASTICITY EQUATIONS.....	152

CHAPTER 1

INTRODUCTION

1.1 Introduction

The most common form of seismic resistant construction is based on ductile design. Steel structures are designed for ductility, where the seismic energy during an earthquake is dissipated in plastic hinges that occur at the ends of the steel frame beams or within braces and shear links. In this manner a structure may sustain local damage, but should not collapse during severe earthquakes.

In steel construction, moment-resisting structural steel frames are widely used as being highly efficient in absorbing earthquake energy demands. For buildings having wide facades, such a structural system is economical and has been shown to be very satisfactory for resisting lateral forces caused by earthquakes. However, in some instances, as in the case of frames with narrow bay widths, moment-resisting frames tend to be somewhat flexible. Although such frames are still safe from collapse during a severe earthquake, they can develop costly non-structural damage. Consequently, the use of diagonally braced steel frames provides a practical alternative to moment resisting frames in such applications. Such frames are frequently used in order to increase the structure's lateral strength and stiffness. Since the overall performance of a conventionally braced frame depends mainly on the performance of the brace, the focus of this study is on the bracing member itself.

During a severe earthquake, the lateral deflections of the frame cause the brace to alternately stretch and buckle. It is this action, the hysteretic behavior of the brace that is responsible for the dissipation of the earthquake input energy and in a large measure for the performance of the frame. However, the hysteretic behavior of such

braces involves complex physical phenomena such as; yielding in tension, progressive lengthening of the brace called growth effect and buckling in compression, which also includes the deterioration of the compressive load capacity, due to Bauschinger effect and the residual kink within the brace itself. Because of the complexity of this hysteretic behavior, it is difficult to predict the seismic response of braced frame structures for design purposes.

Many experimental and analytical studies have been conducted on the inelastic cyclic behavior of steel braces. The experimental studies provided a wide range of data which have been used to develop analytical models to simulate the inelastic behavior of braces under severe cyclic load reversals. The developed analytical models can be categorized in three groups; finite element, phenomenological, and physical theory models. Finite element models provide a realistic representation of the brace axial force-deformation behavior. However, they are computationally expensive. On the other hand, phenomenological models are computationally more efficient than finite element models. Yet, they usually involve numerous empirical coefficients and thus can be applied only to specific braces for which test data is available. Physical theory models combine the advantages of both finite element and phenomenological models. That is, while they are relatively more universally applicable and accurate than phenomenological models, they are also more computationally efficient than finite element models. However, most of the existing physical theory models are either developed for a specific brace type or fail to simulate the Bauschinger effect, the degradation in the axial stiffness (growth effect) and the axial force versus transverse deformation of the brace. In some of these models approximate regression analyses were used to account for the plastic condition of a specific brace. Moreover, some of the better physical theory models are very difficult to use in practice as they involve numerous implicit parameters that require extra computations to define the cyclic buckling behavior of a particular brace. Therefore, a physical theory model that is almost as accurate as a finite element model but easily applicable in practice is required.

Accordingly, this study presents a simple, yet an efficient and a universally applicable physical theory model that can be used to simulate the complex inelastic cyclic behavior of steel braces. The model is verified by comparing analytical calculations to experimental data for several individual steel braces with various properties.

1.2 Background Information and Literature Review

The inelastic behavior of braces subjected to axial cyclic loading has been investigated by numerous researchers in the last three decades. As mentioned earlier, these investigations have included both experimental and analytical studies. These studies are summarized below.

1.2.1 Review of Experimental Research

Many experiments have been conducted on inelastic behavior of axially loaded steel braces. However, most of these experiments have dealt with members subjected to monotonically increasing compression. Only a few experiments have been performed on the cyclic inelastic behavior of steel braces.

Wakabayashi et al (1973, 1977, and 1980) have performed numerous experiments to study the inelastic cyclic behavior of steel braces. In these experiments more than 30 small-scale specimens were tested. All of these specimens had identical 15×15 mm square solid cross sections but various effective slenderness ratios. In addition, tests on steel braces restrained against rotation at both ends have been conducted. Twenty-one specimens having square solid cross section and eight specimens having H-shaped cross section were investigated. These specimens had relatively short lengths ranging between 193 to 928 mm. From the test data the inelastic cyclic behavior of braces was obtained and studied.

Sherman (1976) tested axially loaded struts and beam-column tubes used in existing offshore oil platforms in the as-received condition. The test results were used to model hysteretic behavior of braces using finite element techniques for further studying the behavior of offshore platforms under dynamic loads. Kahn and Hanson (1976) conducted a series of cyclic experimental tests on 25×12 mm solid steel bars. The lengths of the bars were varied to produce slenderness ratios of 85, 120, and 210. It was found that the dynamic hysteretic response was nearly identical to the static response.

Jain et al. (1978) have performed experiments on 18 specimens made from 25.4×25.4 mm hollow cold-rolled steel tubes. Various effective slenderness ratios were used in the tests. It was concluded that the inelastic hysteretic behavior of steel members was significantly influenced by their effective slenderness ratio.

Popov et al. (1980) tested four tubular steel braces, representative of one-six scale offshore construction. The tests were conducted to investigate the effects of material properties, diameter to wall thickness ratios and effective length of the braces. It was concluded that local buckling can be expected in such members having thin wall thicknesses. It was also found that the axial load versus axial displacement curves obtained for the fixed-end specimens were considerably different than those obtained for the pinned-end ones.

Black et al. (1980) investigated the hysteretic behavior of 24 axially loaded steel braces, having a variety of cross-sectional shapes and slenderness ratios frequently encountered in practice. Various loading histories were applied. Since, some of the formulations, which are derived in this study, are based on the data of the tests conducted by Black et al (1980), a detailed description of the tests and related conclusions are presented in a specific sub-section below.

1.2.1.1 Black et al. (1980)

Black et al. (1980) conducted cyclic axial reversed loading experiments on 24 structural steel braces with a wide range of cross-section geometries. The individual specimens were selected from standard structural steel shapes primarily on the basis of two criteria: (i) the slenderness ratios of the test specimens are similar to those used in practice and (ii) the shapes and proportions of the test specimens need to represent typical braces in current use. The maximum size of the members was set by the capacity of the available double-acting hydraulic cylinder.

Included within the 24 selected specimens were six different cross-sectional shapes: wide-flanges, thin and thick-walled square tubes, thin and thick-walled round pipes, structural tees, and fabricated double angles, and double channels. The built-up specimens were of special interest to see if the two elements would effectively act as a single member during extreme inelastic cycling loading. The material for all the rolled sections conformed to ASTM specifications for A36 steel; for pipes, to A53 Grade B steel; for square tubes, to A501 steel.

To assess the effect of end restraint on brace behavior, two boundaries on the possible end conditions were considered; eighteen of the specimens were pinned at both ends and had slenderness ratios of 40, 80 and 120; the remaining six specimens were pinned at one end and fixed at the other and had slenderness ratios of 40 and 80.

The test set up is demonstrated in Fig. 1.1. The test brace was welded to (44 mm-57 mm) thick end plates with full penetration welds. The specimen was attached to the end fixtures with large high-strength bolts. The specimen length from pin to pin included heavy end support clevises containing roller bearings and attachment flanges. Preliminary calculations showed that these end details would not significantly affect the buckling behavior of a specimen. From the test data, Black et al. (1980) obtained relations between the applied axial force P and the axial displacement δ . The P - δ curves trace out the hysteretic loops for each brace.

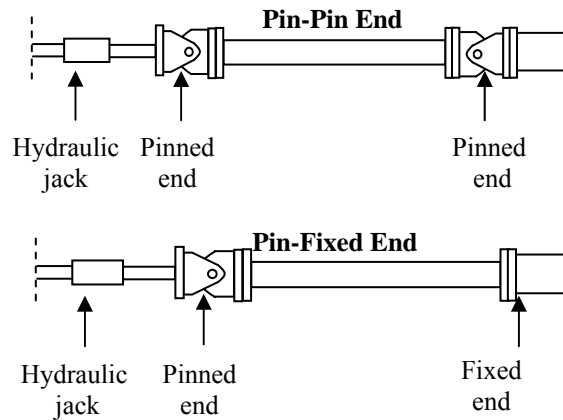


Fig. 1.1 Test set up of Black et al. (1980)

1.2.2 Review of Analytical Brace Hysteretic Models

Several analytical models have been developed to represent cyclic axial load-deformation behavior of steel braces. These models can be divided into three different general types. The finite element, the phenomenological, and the physical theory brace models. The summary of literature review conducted on each modeling type is presented below.

1.2.2.1 Finite Element Model

The technique employed in detailed finite element modeling is to subdivide a brace longitudinally into a series of elements as shown in Fig.1.2. While providing the most realistic representation of brace's behavior, the finite element model usually demands computations too costly to be applied to practical analyses of large-scale braced structures. This model has been employed by several investigators. Fujimoto et al (1972) subdivided the cross-section of the longitudinal elements into fibers with elasto-plastic properties. Marshall (1974) and Sherman and Erzurumlu (1976) used a

series of beams and nonlinear springs to model brace behavior. Riahi et al (1979) developed a general purpose three dimensional beam-column element with end plastic hinges and geometric stiffness that are connected in series to model brace buckling. Powell (1980) employed elements with the critical cross-sections subdivided into fibers to predict the inelastic behavior of piping systems.

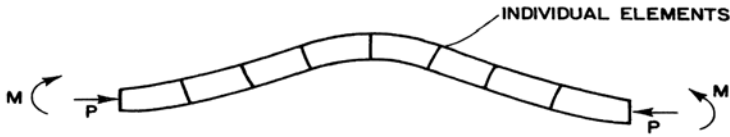


Fig. 1.2 Finite Element Model

1.2.2.2 Phenomenological Model

The basis of these models is to pre-define the shape of the axial force-axial deformation response of a truss element that represents the brace by employing either mathematical or empirical results (Fig.1.3). Phenomenological models are computationally efficient, but usually involve numerous empirical coefficients and thus can be applied only to specific braces for which test data are available.

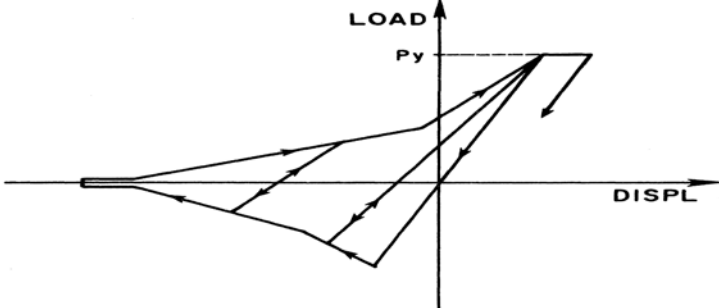


Fig. 1.3 Phenomenological Model

Models of this type have been developed by Higginbotham (1973), Nilforsoushan (1973), Singh (1977), Marshall (1978), Roeder (1977), Jain (1978), Maison (1980). Higginbotham (1973) curve-fit the analytical results by employing second order polynomial equations to describe phases C-D, D-F and F-G of brace response shown in Fig.1.4.

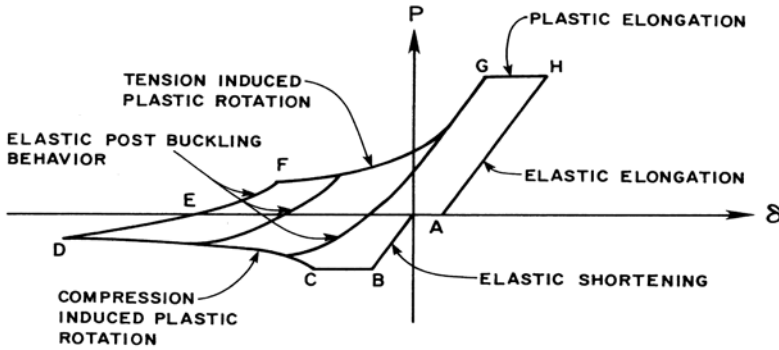


Fig. 1.4 Higginbotham (1973) Model

Nilforsoushan (1973) developed a model with nine piece-wise linear segments to define the brace hysteretic loops shown in Fig.1.5. The strength and stiffness in each segment were defined by a set of input empirical parameters.

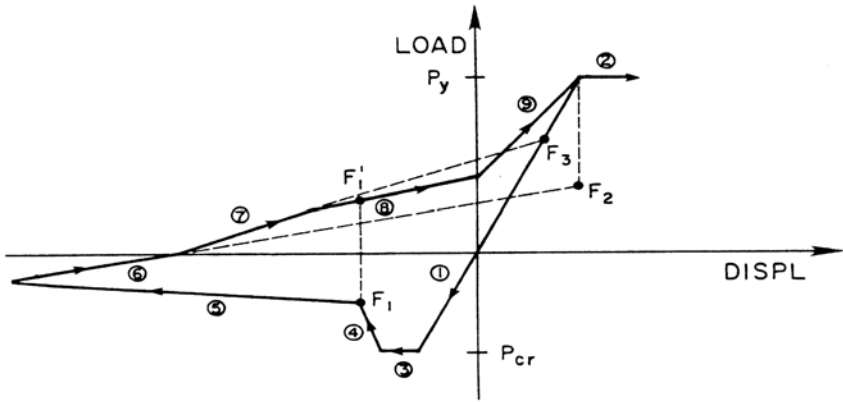


Fig. 1.5 Nilforsoushan (1973) Model

Singh (1977) developed a simpler five segments piece-wise linear model which could give a realistic fit for members with high ($Kl/r > 120$) slenderness ratios as shown in Fig.1.6.

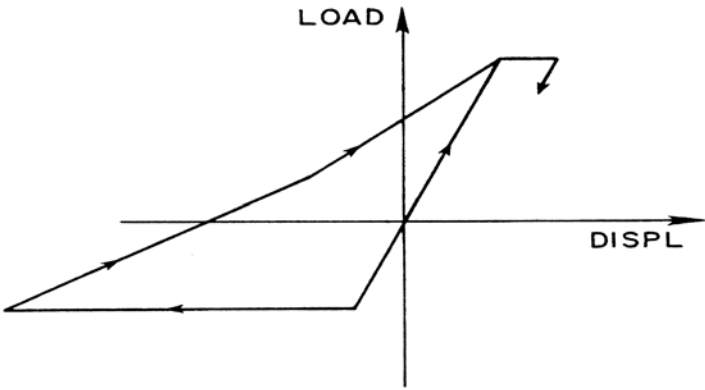


Fig. 1.6 Singh (1977) Model

Marshall (1978) employed a seven segment piece-wise linear model with an algorithm defining failure of a brace based on estimating the onset of local buckling. The model is presented in Fig.1.7

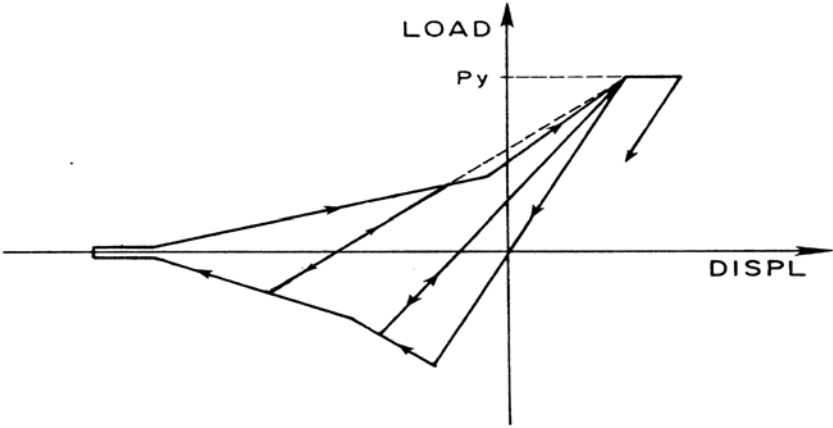


Fig. 1.7 Marshall (1978) Model

Jain (1978) developed a six segment model for members with high slenderness. This model has two buckling loads, one for the first cycle and one for subsequent cycles as shown in Fig.1.8. The model also incorporates a feature to account for observed growth in brace length during buckling and re-straightening.

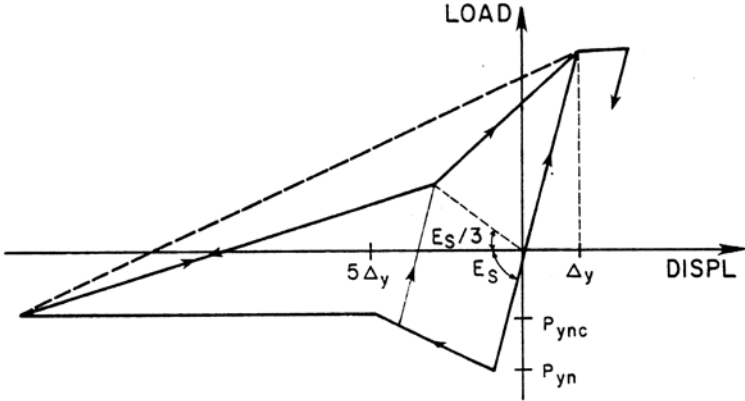


Fig. 1.8 Jain (1978) Model

Roeder (1977), using a nine segment model similar to that of Nilforsoushan's, introduced a feature to permit gradual deterioration of the buckling load between two bounds. The model is displayed in Fig.1.9.

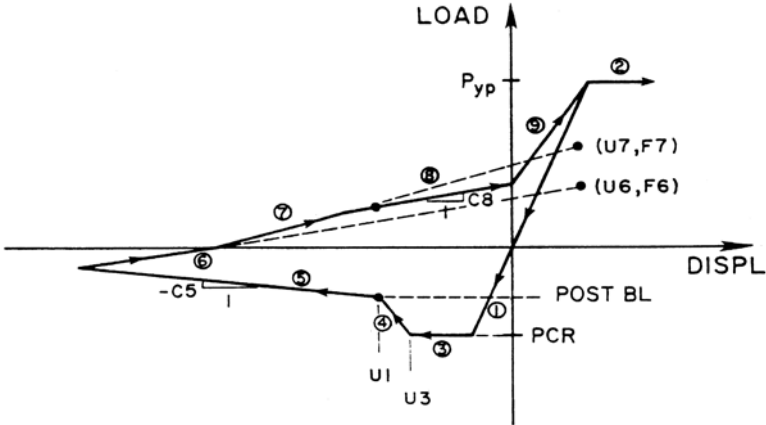


Fig. 1.9 Roeder (1977) Model

Maison (1980) also employed a nine segment model with buckling load deterioration capabilities similar to that of Roeder's. This model also accounted for the hysteretic growth in brace length during buckling and re-straightening as shown in Fig.1.10

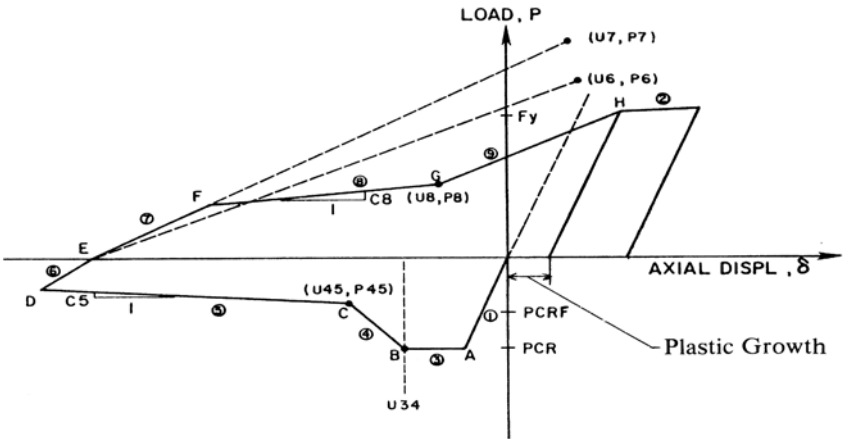


Fig. 1.10 Maison (1980) Model

1.2.2.3 Physical Theory Model

Physical theory models as shown in Fig.1.11 account for the interaction between bending and an axial effects and are formulated based on physical considerations that influence inelastic brace behavior. Unlike phenomenological models, input parameters for physical theory models are generally based on material properties and common geometric or derived engineering properties of a member (e.g, the yield strength, the cross-sectional area, cross sectional moment of inertia, plastic section modulus, etc.). However, the geometric representation of a brace is considerably simpler than used for a finite element model shown in Fig.1.2. Thus, physical theory models combine the realism of finite element models with the computational simplicity of phenomenological models.

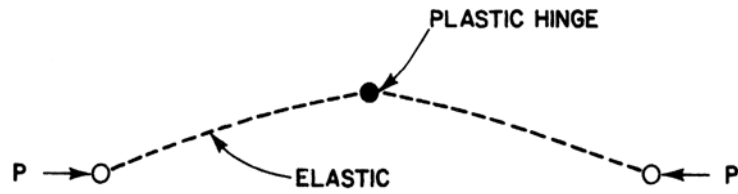


Fig. 1.11 Physical Theory Model (Ikeda and Mahin, 1984)

Several physical theory models have been developed to simulate the inelastic buckling behavior of steel braces. Geometrically, these models consist of a bracing member that usually has a plastic hinge at mid-length connecting two elastic beam segments as shown in Fig. 1.12.

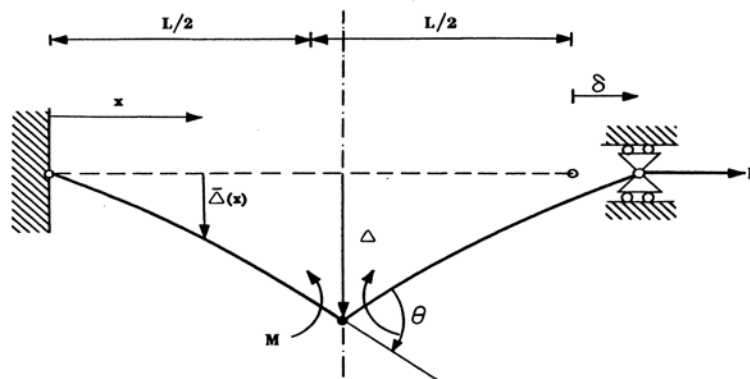


Fig. 1.12 Typical Member Geometry of Point Hinge Model (Ikeda and Mahin, 1980)

One of the first physical theory solutions of post-buckling axial force-axial displacement relationship for slender braces was proposed by Higginbotham (1973).

For braces with high slenderness ratios ($Kl/r > 120$), Higginbotham's analytical model predicts the behavior of the first cycle of experimental results with reasonable accuracy. During later cycles, however, Higginbotham's model does not consider the deterioration of buckling loads and results overestimate observed behavior. Furthermore, since the solution of the analytical model includes elliptic integrals, it entails costly computation.

Nirforoushan (1973) developed a quite similar but simpler model and used it to arrive at parameters for his phenomenological model. Singh (1977) also developed a model having assumptions similar to those of Higginbotham's. However, he used the energy method in formulating the basic equations and assumed sine curves for the deflected shapes of the two beam segments under compression.

Nonaka (1973, 1977) and Gugerli (1982) developed models close to Singh's model. Their models, however, included axial and rotational deformation components at the plastic hinge. They solved the beam-column equation directly. The resultant basic equations contained trigonometric functions for compressive axial forces and hyperbolic functions for tensile forces.

Fujiwara (1979 and 1980) formulated a similar model employing the same assumptions for the plastic hinge and the beam segments.

Wakabayashi *et al* (1974, 1976) developed a more general plastic hinge model. The brace model consisted of two flexurally rigid and axially elastic truss bars and an inelastic hinge at the center. Since the truss bars were flexurally rigid, complex functions were not needed to specify their deflected shape thereby greatly simplifying the computations.

Zayas *et al* (1981) formulated a physical theory brace model using the displacement method. Their model included lateral mid-length deflection as a second degree of freedom which is removed by elastic condensation during the formulation of the

element axial stiffness. The deflected shape of the beam segments was represented by cubic Hermitian polynomials (Hilberland, 1956). Based on this idealization, the tangent stiffness matrix could be easily formulated.

Soroushian and Alawa (1991) developed a physical theory model for steel braces. The model incorporates simplified theoretical formulations based on some assumptions on the experimentally observed physical behavior of steel struts. Some semi-empirical techniques were used in the model to account for the partial plastification and degradation of plastic hinge under cyclic load, softening and yielding along the element length, and possibility of straight element buckling. The model uses displacement as input, and involves a limited number of degrees of freedom.

Remennikov and Walpole (1997) formulated a brace model using plastic-hinge located at the mid-length. Step-wise regression analysis was employed, to approximate the plastic condition for steel channel sections. The proposed model combines the analytical formulation of plastic hinge behavior under cyclic load, with empirical formulae based on a study of experimental data. Also the developed model accounts for the Bauschinger effect and the degradation in axial brace stiffness with cyclic loading.

Jin and El-Tawil (2003) developed a physical model which accounts for the gradual spread of plasticity along the length of the brace and within the cross section, simulates the degradation of axial stiffness with cycling, and has no restrictions on the boundary conditions. The model is of the distributed macro-type and makes use of a bounding surface plasticity model applied at the cross section level to relate stress resultants to generalized cross section strains, i.e., centroidal axial strain and curvatures.

Dicleli and Mehta (2007) developed a nonlinear structural model to simulate the cyclic behavior of steel braces using the nonlinear finite element based software ADINA (2004). The model is aimed at simulating the inelastic cyclic behavior of

braces for design purposes. The nonlinear cyclic axial force-deformation simulation in ADINA is done for braces with box sections. However, the developed nonlinear model may be applicable to braces with various sections. The developed model does not consider the Bauschinger and the growth effects, but it is very easy to use in practice.

1.3 Research Objective and Scope

The main objective of this study is to develop a physical theory model to accurately simulate the inelastic cyclic behavior of steel braces including Bauschinger effect, growth effect, residual kink as well as brace axial force versus transverse displacement relationship. To achieve the above stated objective a physical theory model is developed and verified using the available experimental test results on brace inelastic cyclic behavior in the literature. The physical theory model developed in this study combines the analytical formulation of the plastic hinge formed at the vertex of the deformed brace, axial force-axial displacement relationship of the brace and axial force-transverse displacement of the brace with some semi-empirical dimensionless formulae developed on the basis of available experimental data to simulate the Bauschinger and growth effects.

The scope of this study is limited to braces with pin ended connections. Local buckling and low cycle fatigue effects are beyond the scope of this study. Consequently, the physical theory model developed as part of this study is more suitable for braces with slenderness ratios larger than 80 since local buckling effects are generally associated with braces with lower slenderness ratios.

1.4 Thesis Outline

Chapter 1 of the thesis contains introductory information, literature review as well as research objectives and scope.

Chapter 2 investigates the inelastic cyclic behavior of steel braces based on the available experimental data. How this behavior is affected by different parameters (slenderness ratio, section shape, etc.) is also examined.

Chapter 3 develops the moment-axial force (M - P) interaction relationships for six different brace section shapes. The developed M - P interactions are used in the analytical formulation of the inelastic cyclic behavior of braces.

Chapter 4 introduces a general physical theory model to simulate the inelastic cyclic behavior of braces. Using this model, analytical formulations for different zones of brace axial force-deformation hysteresis is obtained.

Chapter 5 presents a comparison of the analytical hysteresis loops (axial force versus axial deformation (P - δ) and axial force versus transverse deformation (P - Δ) curves) obtained using the developed analytical model with the corresponding experimental data and some of the analytical models available in the literature.

Chapter 6 presents the summary and conclusions obtained from this research study.

CHAPTER 2

BEHAVIOR OF BRACES

2.1 General

Prior to introducing the analytical model, it is important to study the actual behavioral characteristics of steel braces in order to identify important features to be simulated by the analytical model. These behavioral properties are described below.

2.2 Cyclic Axial Load Response

The behavior of axially loaded members is commonly expressed in terms of an axial load (P), an axial deformation (δ), and a transverse displacement (Δ), at the mid-length of the brace as shown in Fig.2.1. The sign convention used throughout this study is such that axial tension forces and deformations are positive, and axial compression forces and deformations are negative.

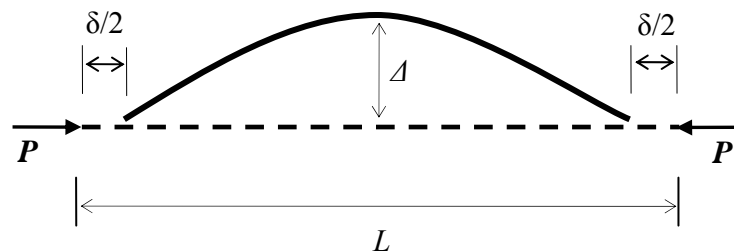


Fig. 2.1 Deformation of brace under axial load

To study the inelastic cyclic behavior of steel braces, the axial force-deformation hysteresis can be broken in to six zones as shown in Fig.2.2a. The definition of these zones is closely related to the physical interpretation of the behavior. A typical cyclic axial force-deformation behavior of a steel brace is demonstrated in Fig. 2.2b.

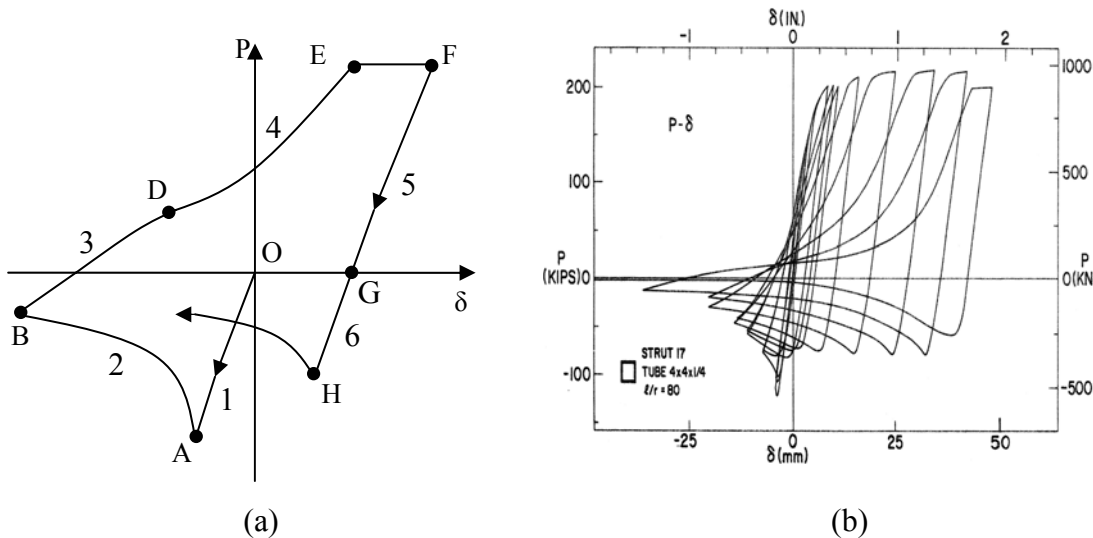


Fig. 2.2 Inelastic axial response of a brace under cyclic axial loading (a) Definition of different zones (b) A sample P - δ curve from the experimental data of Black et al. (1980)

2.2.1 Definition of Hysteretic Zones

The first zone shown in Fig 2.2a is generated by monotonically applying a compressive strain to a brace from point O to point A . The behavior of this first zone depends on the slenderness ratio and initial imperfection of the brace. If the brace is sufficiently slender and perfectly straight, the brace buckles elastically. Due to the

initial imperfection, the brace shows a small amount of lateral deflection as shown in Fig.2.1.

Zone 2 is dominated by the inelastic bending of the brace due to the $P-\Delta$ moment induced by the compressive axial load, P . This zone is characterized by very large lateral deflections at the mid-length of the brace and by a plastic hinge in the center region of the brace formed at the verge of buckling. The magnitude of P monotonically decreases with the increasing magnitude of the deformation. The magnitude of the load must decrease because the $P-\Delta$ moment cannot exceed the brace's plastic moment capacity. Cyclic reversal is shown to take place at point B where the compressive load is decreased. Immediately after decreasing the compressive load, the inelastically strained portion of the brace will again begin to behave elastically.

Zone 3 corresponds to elastic unloading and tension loading of the brace. The slope of this zone is much smaller than that of Zone 1 due to the large permanent lateral deflection at the mid-length of the brace, which results in a curved rather than a straight member.

Zone 4 represents a zone of continued elastic bending with the brace lengthening while an increasing tensile load is applied. During the application of a tensile force of an increasing magnitude, the brace elongates and gradually straightens. This is accompanied by an increasing stiffening of the brace due to the gradual reduction in the transverse deflection of the brace. During this process, the $P-\Delta$ moments rotate the initially formed plastic hinge in the opposite sense of direction.

Point E of Fig.2.2a is the point at which the brace is fully straightened. If the tensile force were removed at this point, the brace would remain essentially straight and be slightly longer than its original length. The internal bending moment is essentially zero when point E is reached, and any elongation beyond this point is a purely uniaxial elongation. Between points E and F is a plastic uniaxial elongation region

for the brace. This zone is characterized by a nearly constant tensile load with increasing elongation. If the unloading occurs before point E is reached, then the plastic uniaxial elongation does not exist.

Point F in Fig.2.2a is a load reversal point. Thus, zone 5 consists of elastic unloading. The elongation decreases linearly with decreasing tensile load, and the slope is essentially the same as that of Zone 1. Within the region beyond Point G, which is described as Zone 6, the brace is compressed by axial force and buckled again at Point H. However, this buckling load is smaller than that of Point A due to the Bauschinger effect and the residual kink remaining within the brace if unloading at Point E occurs before the axial yield capacity of the brace is reached.

2.2.2 Bauschinger Effect versus Behavior of Braces

Bauschinger effect is a natural property of steel that affects the cyclic axial force-deformation behavior of steel braces. After steel has been stressed beyond its elastic limit and into the plastic range, a number of phenomena can be observed during repeated unloading, reloading and stress reversal. First, for the typical stress-strain relationship of a steel coupon shown in Fig.2.3, unloading to $\sigma = 0$ and reloading to the previously attained maximum stress level will be elastic with a stiffness equal to the original stiffness, E (modulus of elasticity). Then as also shown in the same figure, upon stress reversal to $\sigma = -\sigma_y$, a sharp corner in the stress strain curve is not found at the onset of yielding; instead, stiffness softening occurs gradually with yielding initiating earlier than otherwise predicted (Bruneau et al., 1998). This behavior is called the Bauschinger effect.

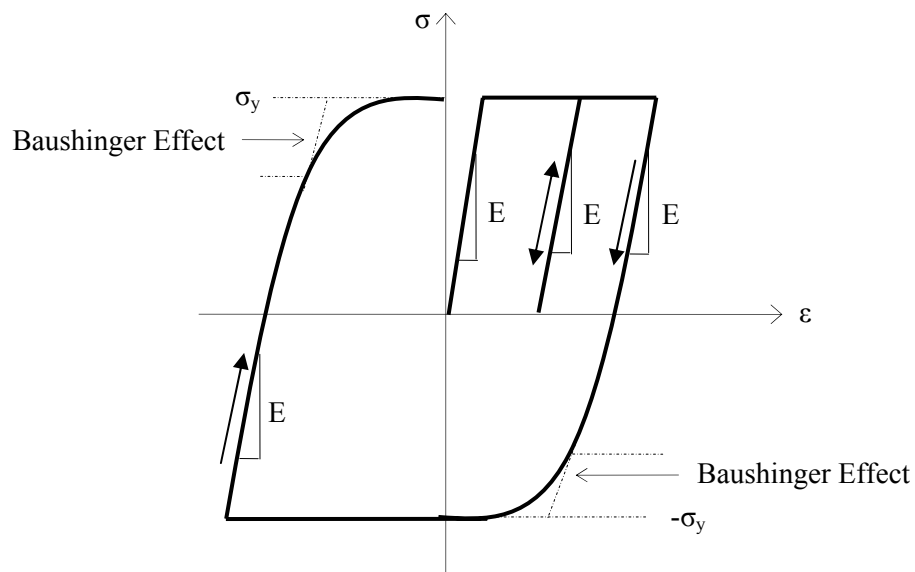


Fig. 2.3 Baushinger effect

Popov and Black (1981) conducted cyclic axial force deformation tests of a steel coupon taken from a wide flange steel brace made of ASTM (American Standards for Testing Materials) A36 mild steel. The cyclic test results are shown in Fig.2.4. As observed from the figure, the Baushinger effect is a function of the cyclic loading history. That is, the softening of the material stiffness (modulus of elasticity) increases with increasing number of load reversals. For the cyclic axial force-deformation relationship of a brace defined earlier, comparing Figs 2.2 and 2.3 it is clearly observed that Zones 4 and 6 are affected by the Baushinger effect. The Baushinger effect results in softening of the slope of Zone 4 in the vicinity of the transition to Zone 5 and a smaller buckling load (Point H) than that of the initial cycle (Point A) due to the softening of the modulus of elasticity. Further details are given in the subsequent sections.

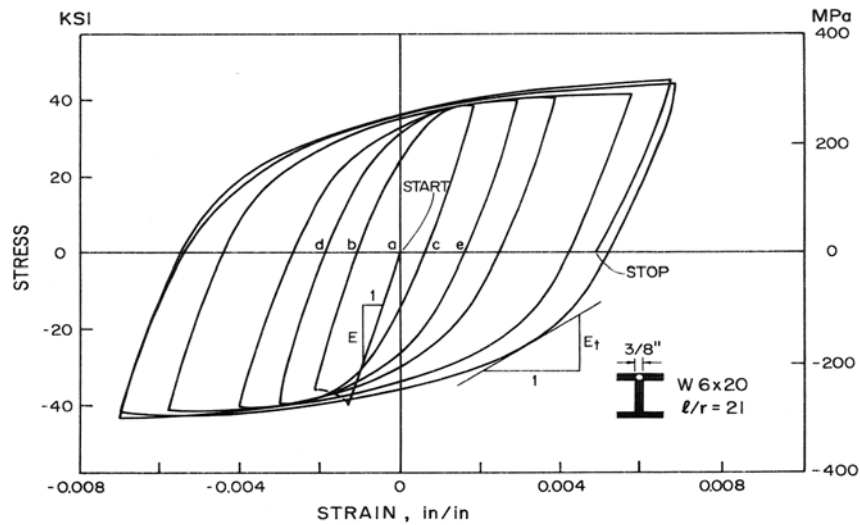


Fig. 2.4 Hysteretic curve from a cyclic coupon test (Black et al. 1980)

2.2.3 Hysteretic Properties of Braces

The most important results from cyclic experiments with braces subjected to repeated buckling and stretching relate the applied axial load P to the axial displacement δ . The P - δ curves trace out the hysteretic loops. The areas enclosed by such curves are a measure of hysteretic behavior and energy dissipation during an earthquake. The most important feature of the hysteretic behavior of braces is the indication that once a brace had buckled, during subsequent cycles the same capacity in compression cannot be reached as shown in Fig.2.5. This reduction in the buckling capacity can be attributed to the presence of a residual lateral displacement at the mid-length of a brace. Moreover, since the critical section at the mid-length of a brace experienced severe stress reversals, the influence of the Bauschinger effect on reducing the steel's tangent modulus becomes pronounced resulting in even smaller buckling load levels. However, while during the consecutive inelastic cycles the maximum compressive loads tend to decrease, the ability of a member to resist tension remains essentially constant regardless of previous cyclic history.

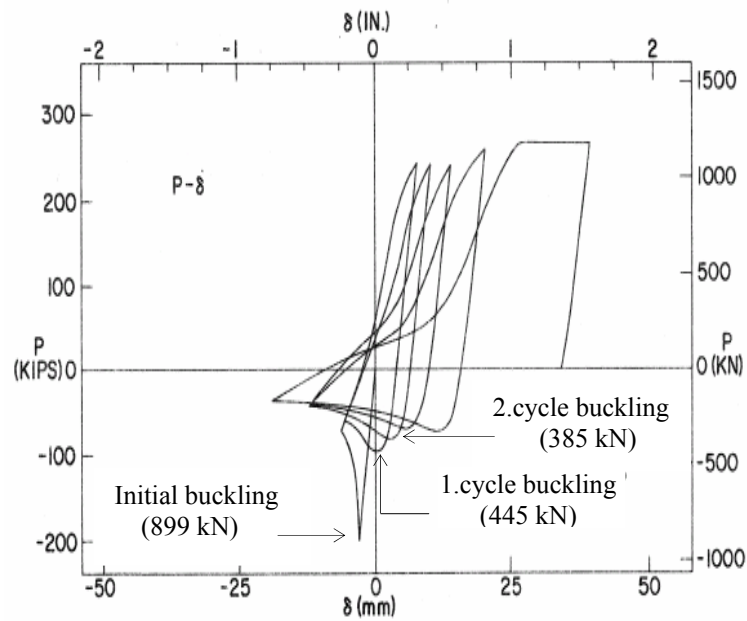


Fig. 2.5 Deterioration of buckling loads

In the earlier studies (both experimental and analytical) researchers have identified three key parameters that affect the hysteretic behavior of a bracing member. These are; slenderness ratio, end condition, and section shape. These three key parameters are discussed next.

2.2.3.1 Effect of Brace Slenderness

The cyclic response of a component loaded axially in compression depends principally on its slenderness. The slenderness ratio (λ) is a function of the brace end condition (k), the brace length (L), and the radius of gyration (r).

$$\lambda = \frac{kL}{r} \tag{2.1}$$

Braces are often described as either slender (large λ), intermediate, or stocky (small λ). The hysteresis loops for braces with different slenderness ratios vary significantly. The hysteretic loops for braces with large values of Kl/r showed a more rapid deterioration in their compressive strengths than those with small values of Kl/r . The ratio of a member's initial capacity in compression to that in tension is similarly a function of the braces slenderness ratio, being larger for the more stocky braces. This is evident in the normalized axial load versus normalized axial displacement envelope plots presented in Fig.2.6 for braces with slenderness ratios equal to 40, 80, and 120. In addition, braces with very small slenderness ratios exhibit a buckling behavior very close to the range of plastic action, and braces with large slenderness ratios exhibit a buckling behavior very near to that of elastic buckling.

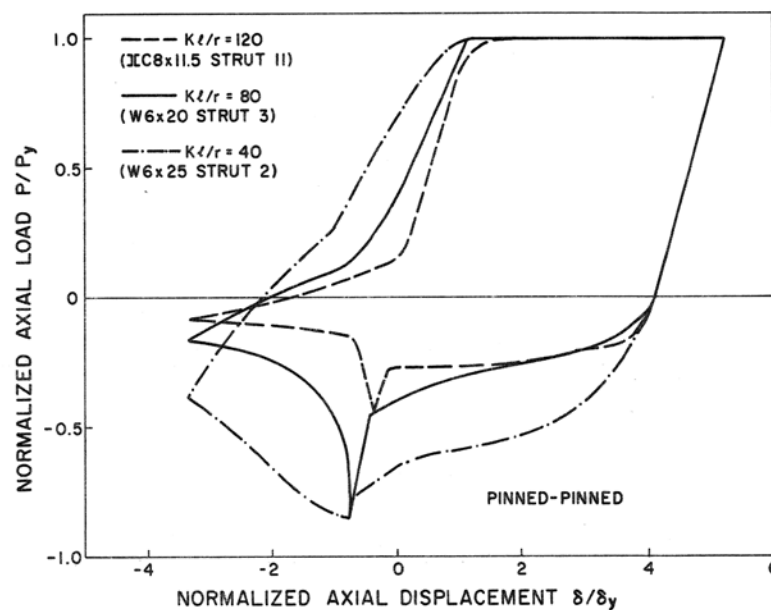


Fig. 2.6 Hysteretic envelopes for braces with different Kl/r 's (Black et al.1980)

2.2.3.2 Effect of End Conditions

The effect of brace end-restraints on the hysteretic behavior of axially loaded braces was examined by Black et al (1980). Normalized force-displacement envelopes were used to compare the hysteretic behavior of braces with identical slenderness ratios but differing lengths due to end conditions. Sample hysteretic envelopes for braces with different end condition are presented in Fig.2.7a (I section brace) and Fig.2.7b (circular tube brace). From Fig.2.7, the similarity of the hysteretic loops for the two cases considered strongly support the extension of the effective length approach to other end conditions for evaluating the cyclic inelastic response of bracing members.

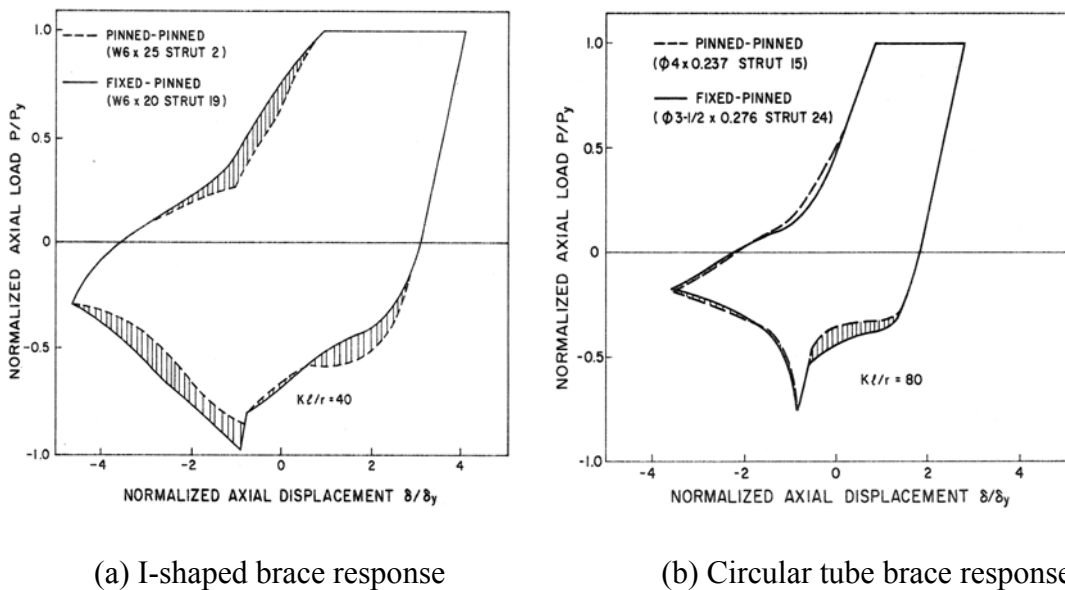


Fig. 2.7 Hysteretic curves for braces with different end conditions (Black et al. 1980)

2.2.3.3 Effect of Section Shape

The effect of cross-section shape on the hysteretic behavior of a brace has been studied independently by several groups of investigators. Jain et al. (1978) tested small tubes of square section, angles and bars of rectangular cross-section. It was concluded that differences in the hysteresis loop characteristics of different section types can be attributed to their different susceptibility to local buckling; thin walled sections being more likely to fail prematurely by early local buckling. Closed sections are less likely to suffer torsional buckling, but their strength deteriorates faster with cycling because of the distortion of the cross section. Black et al.(1980) tested a variety of full sized steel sections (wide-flanges, double angles, T sections, pipes and square tubes) with slenderness values equal to 40,80, and 120. It was noted that cyclic loading reduces the buckling strength of braces, and that the effect of cross section shape on the hysteretic characteristics is most noticeable in small slenderness sections where occurrence of local buckling is predominant. Sample hysteretic envelopes from Black et al. (1980) for different braces each with a slenderness ratio equal to 80, are presented in Fig.2.8a and Fig.2.8b.

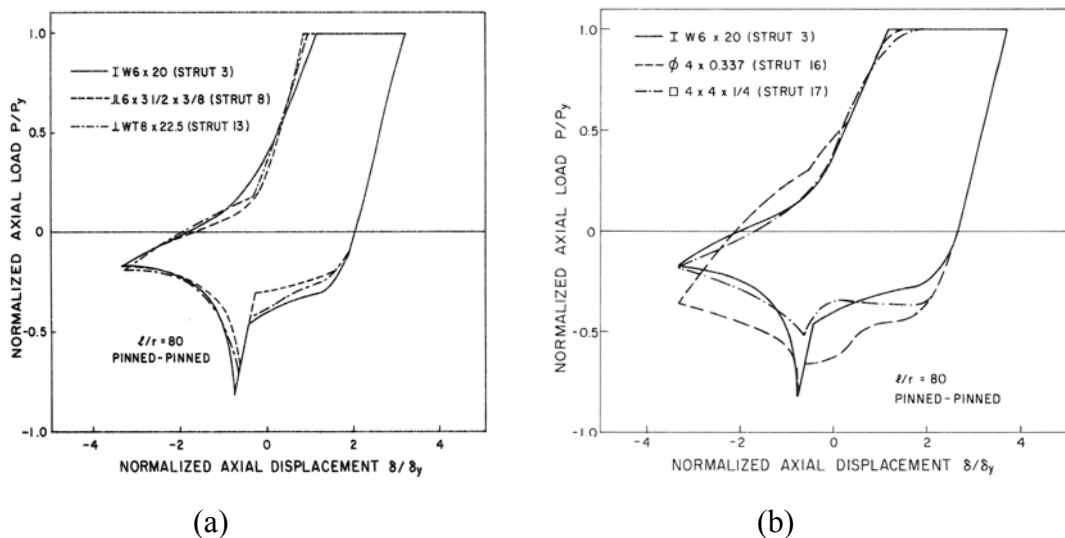


Fig. 2.8 Hysteretic curves for braces with different cross-section shapes (Black et al 1980)

Furthermore, Gugerli (1982) tested the effect of section shape and scale effect on the hysteretic characteristics of rectangular tube and wide-flange sections. It was found that the hysteresis loops of both section types were similar but fracture was more critical than local buckling in limiting the resistance and energy dissipating capacity of the braces. The fracture life of tubes was smaller than that of wide-flanges in these experiments.

CHAPTER 3

DERIVATION OF MOMENT-AXIAL FORCE RELATIONSHIPS FOR STEEL BRACE SECTIONS

The main objective of this chapter is to derive analytical equations defining the relationships between the moment and axial force for six different brace section shapes used in practice. The derived equations will be used in the next chapter within the analytical formulations defining the inelastic cyclic axial force-deformation behavior of braces.

3.1 Calculation of Reduced Plastic Moment Capacity due to Axial Load

If a member is subjected to the combined action of bending moment and axial force, the plastic moment capacity of the member is reduced from the full value of M_p , which is the largest plastic bending moment that the section can carry, to a lesser value which is designated as the reduced plastic moment, M_{pr} . For the calculation of M_{pr} a number of simplifying assumptions are made as follows;

1. Plane sections remain plain.
2. Member instability (flange local buckling, web local buckling and lateral-torsional buckling) is avoided.
3. The elasto-perfectly plastic model is used for the stress strain relationship of steel (Fig.3.1).

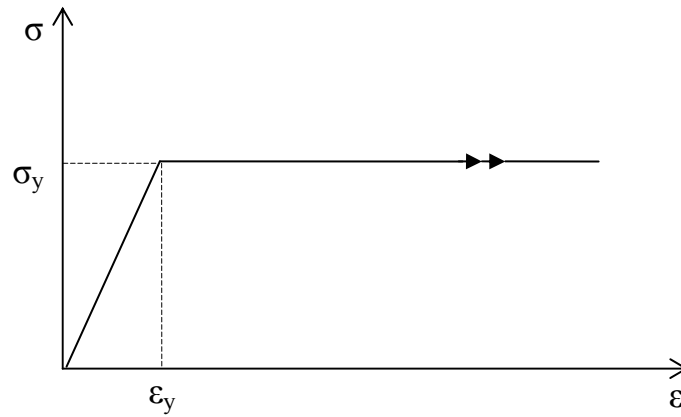


Fig. 3.1 Elasto-perfectly plastic model for steel.

The value of the reduced plastic moment M_{pr} is a property of the cross section. It is independent of the slenderness ratio and it is immaterial of the axial force as being compressive or tensile for steel. Fig.3.2 shows the stress-distribution in a bisymmetrical section at various stages of deformation caused by axial force and moment, as the moment increases.

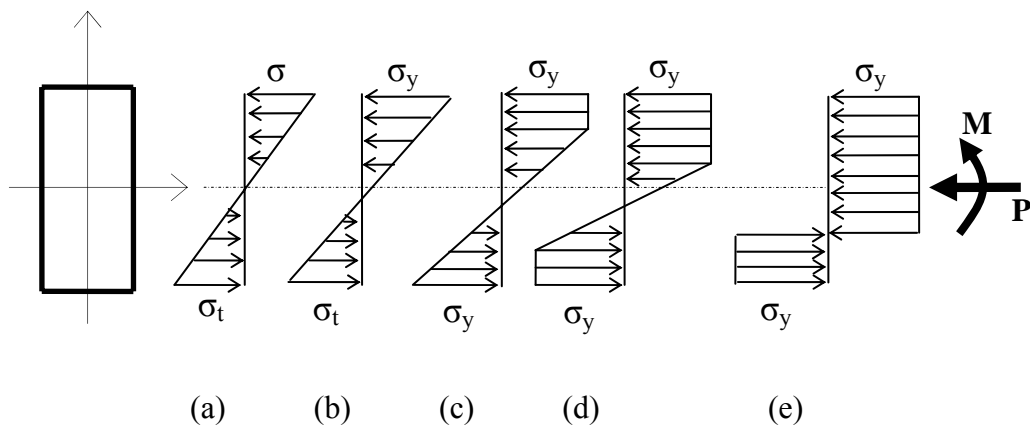


Fig. 3.2 The combined action of M and P

When full plastification of the section occurs, a portion of the cross-sectional area carries the axial force. Therefore, the stress block on the compression side is larger than that on the tension side as shown in Fig.3.2e. Furthermore, as shown in Fig.3.3, the total stress distribution may be divided into two parts; a part that is associated with the axial load (Fig.3.3c) and another part that corresponds to the bending moment (Fig.3.3b). Also note that Fig.3.3b represents the fully plastic moment, M_p . M_p can be calculated as follows,

$$M_p = Cx + Tx \tag{3.1}$$

where, C is the resultant compressive force, T is the resultant tensile force, and x is the distance between these forces and the axis of symmetry. The second order moment, M , which is produced by the axial force about the neutral axis, reduces the plastic moment capacity. Thus,

$$M_{pr} = M_p - M \tag{3.2}$$

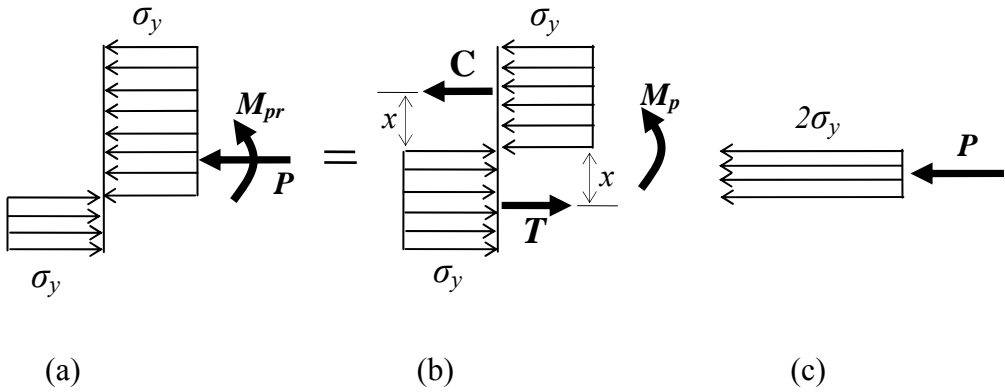


Fig. 3.3 The analysis of the stress distribution

In the following sections, the moment-axial force interaction relationships (the reduced plastic moment capacity) for various section shapes (W, T, square tube, rectangular tube, double-channel, and double-angle) are presented. In pin-pin ended braces, buckling occurs about the weak axis of the section so calculations are presented only about this axis.

3.1.1 W Section

The distribution of fully plastic stresses on the cross-section of a W section is demonstrated in Fig. 3.4 below.

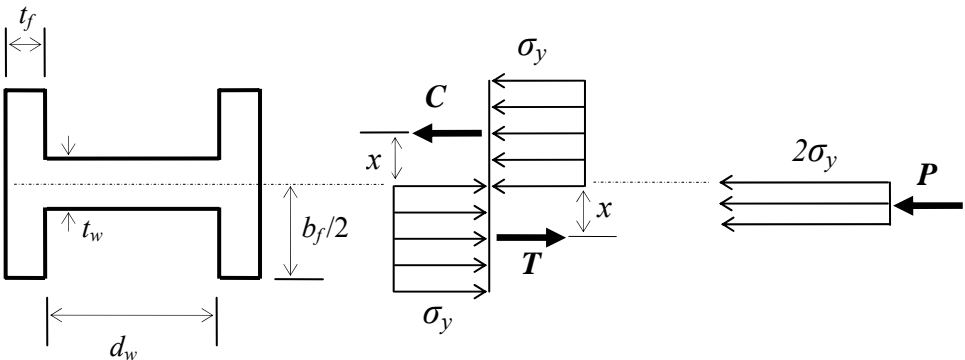


Fig. 3.4 Plastic stress distribution in W section

For a W section, the compression (C) and tensile (T) force resultants of the stress block when the section attains its full plastic moment capacity in the absence of axial load are calculated as:

$$C = T = \sigma_y \frac{A}{2} \tag{3.3}$$

where σ , is the yield stress of steel and A is the area of the cross section expressed as;

$$A = 2b_f t_f + t_w d_w \quad (3.4)$$

In the above equation, b_f , t_f , t_w , and d_w are respectively the width of the flange, the thickness of the flange, the thickness of the web and the depth of the web. Substituting Eqn. (3.4) in to Eqn. (3.3),

$$C = T = \left(b_f t_f + \frac{t_w d_w}{2} \right) \sigma_y \quad (3.5)$$

The distance between the forces and axis of symmetry, x , can be calculated as follows,

$$x = \frac{b_f t_f \frac{b_f}{4} + d_w \frac{t_w}{2} \frac{t_w}{4}}{b_f t_f + \frac{t_w d_w}{2}} \quad (3.6)$$

Substituting Eqn. (3.5) and Eqn. (3.6) into Eqn. (3.1), the plastic moment capacity, M_p , of this section is obtained as;

$$M_p = \left(\frac{b_f^2 t_f}{2} + \frac{t_w^2 d_w}{4} \right) \sigma_y \quad (3.7)$$

For the case where an axial force is also acting on the cross-section, one must consider two possible cases for the weak axis bending of W sections;

1. The effect of the axial force P is confined within the web area
2. The effect of the axial force P has penetrated into the flange area

3.1.1.1 Axial Force Effect Confined Within the Web Area

Fig. 3.5 below demonstrates the stress distribution on one side of the centroid of the cross-section due to the applied axial load. Note that the intensity of the stress block is set at $2\sigma_y$. The moment of this half stress block about the centroid of the cross-section represents the part of the plastic moment capacity consumed by the axial load. This is done to facilitate the calculation of the reduced plastic moment capacity of the section.

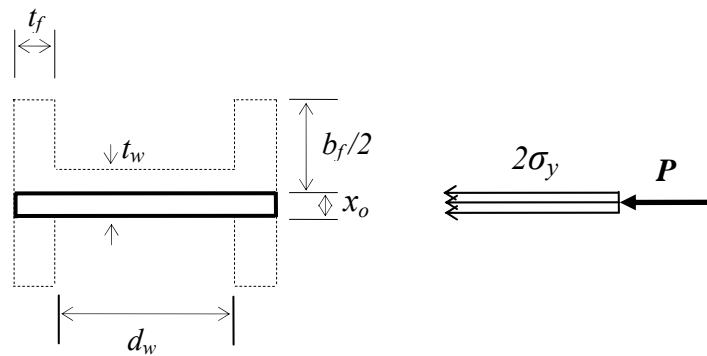


Fig. 3.5 Axial force effect is confined to web (W section)

If the effect of the axial force P is only confined to the web area, the relationship between the moment and axial force can be calculated as follows (Fig.3.5);

$$P = 2\sigma_y x_o (d_w + 2t_f) \quad (3.8)$$

where x_o is a distance that describes whether the axial force is confined within the web area or is penetrated into the flanges. The moment, M , of this axial force about the axis of symmetry is obtained as:

$$M = P \frac{x_0}{2} \quad (3.9)$$

Substituting Eqn. (3.8) into Eqn. (3.9)

$$M = x_0^2 (d_w + 2t_f) \sigma_y \quad (3.10)$$

Now, substituting the above equation into Eqn. (3.2), the reduced plastic moment capacity of the section is obtained as;

$$M_{pr} = M_p - x_0^2 (d_w + 2t_f) \sigma_y \quad (3.11)$$

Next, the axial yield force, P_y is defined as follows;

$$P_y = \sigma_y A \quad (3.12)$$

From Eqns. (3.12) and (3.8), x_0 can be expressed in the following form;

$$x_0 = \frac{A}{2(d_w + 2t_f)} \left(\frac{P}{P_y} \right) \quad (3.13)$$

Substituting Eqn. (3.13) into Eqn. (3.11), the reduced plastic moment capacity of the section is obtained as a function of the axial load to yield axial load ratio as;

$$M_{pr} = M_p - \frac{A^2}{4(d_w + 2t_f)} \left(\frac{P}{P_y} \right)^2 \sigma_y \quad (3.14)$$

It is to be noted that the plastic section modulus, Z is expressed as;

$$Z = \frac{M_p}{\sigma_y} \quad (3.15)$$

Substituting Eqn. (3.15) into the Eqn. (3.14) and rearranging, the following final expression for the reduced plastic moment capacity of the section is obtained as follows;

$$\frac{M_{pr}}{M_p} = 1 - \frac{A^2}{4(d_w + 2t_f)Z} \left(\frac{P}{P_y} \right)^2 \quad (3.16)$$

3.1.1.2 Axial Force Effect Penetrated into the Flanges

If the axial force is penetrated into the flange, a procedure similar to that used in the previous section can be applied to calculate the reduced plastic moment capacity of the section. Fig. 3.6 below demonstrates the stress distribution on one side of the centroid of the cross-section due to the applied axial load. This stress distribution with an intensity of $2\sigma_y$ is again used to facilitate the calculation of the reduced plastic moment capacity of the section due to the presence of the axial load.

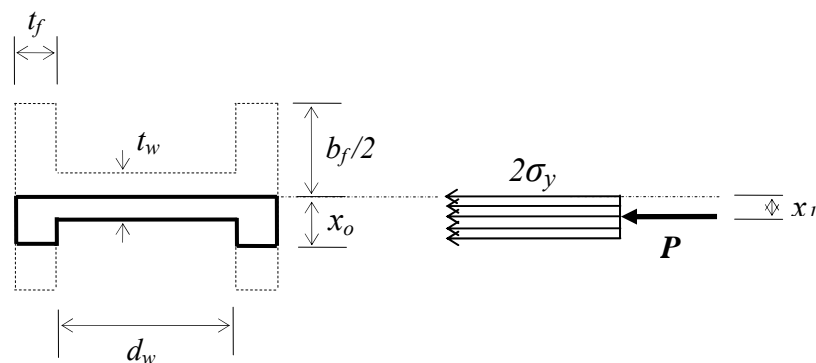


Fig. 3.6 Axial force effect has penetrated into t flange (W section)

From Fig.3.6

$$P = 2\sigma_y \left(2t_f x_0 + \frac{t_w d_w}{2} \right) \quad (3.17)$$

The distance between the axial force and axis of symmetry, x_1 is expressed as;

$$x_1 = \frac{2t_f x_0 \frac{x_0}{2} + d_w \frac{t_w}{2} \frac{t_w}{4}}{2t_f x_0 + \frac{td_w}{2}} \quad (3.18)$$

The moment, M , which is produced by the axial load is then calculated as follows;

$$M = Px_1 \quad (3.19)$$

Substituting Eqns. (3.17) and (3.18) into Eqn. (3.19), the moment produced by the axial load is calculated as;

$$M = \left(2t_f x_0^2 + \frac{d_w t_w^2}{4} \right) \sigma_y \quad (3.20)$$

Substituting Eqns. (3.7) and (3.20) into Eqn. (3.2), the reduced plastic moment capacity of the section is expressed as;

$$M_{pr} = \left(\frac{b_f^2 t_f}{2} + \frac{d_w t_w^2}{4} \right) \sigma_y - \left(2t_f x_0^2 + \frac{d_w t_w^2}{4} \right) \sigma_y \quad (3.21)$$

Simplifying the above equation, M_{pr} is expressed as;

$$M_{pr} = \frac{t_f}{2} (b_f^2 - 4x_0^2) \sigma_y \quad (3.22)$$

Now, the axial yield force, P_y , of the section is calculated as:

$$P_y = \sigma_y A \quad (3.23)$$

From Eqns. (3.23) and (3.17), x_0 can be expressed in the following form;

$$x_0 = \frac{A}{4t_f} \left(\frac{P}{P_y} - \frac{d_w t_w}{A} \right) \quad (3.24)$$

Also note that the area of the web, A_w is equal to;

$$A_w = t_w d_w \quad (3.25)$$

Now, substituting Eqn (3.25) in to Eqn. (3.24), x_0 is expressed as;

$$x_0 = \frac{A}{4t_f} \left(\frac{P}{P_y} - \frac{A_w}{A} \right) \quad (3.26)$$

Next, substituting Eqn. (3.26) into Eqn. (3.22), M_{pr} is expressed as;

$$M_{pr} = \frac{t_f b_f^2}{2} \left[1 - \frac{A^2}{4t_f^2 b_f^2} \left(\frac{P}{P_y} - \frac{A_w}{A} \right)^2 \right] \sigma_y \quad (3.27)$$

The area of the flange, A_f is presented in terms of the section properties as follows;

$$A_f = 2b_f t_f = A - A_w \quad (3.28)$$

From the above equation

$$b_f^2 t_f^2 = \frac{(A - A_w)^2}{4} \quad (3.29)$$

Substituting Eqn. (3.29) in to Eqn. (3.27), M_{pr} is expressed as;

$$M_{pr} = \frac{b_f^2 t_f^2}{2} \left[1 - \frac{\left(\frac{P}{P_y} - \frac{A_w}{A} \right)^2}{\left(1 - \frac{A_w}{A} \right)^2} \right] \sigma_y \quad (3.30)$$

Finally, substituting Eqn. (3.15) in to the above equation and rearranging, M_{pr} is obtained as follows;

$$\frac{M_{pr}}{M_p} = \frac{b_f^2 t_f^2}{2Z} \left[1 - \frac{\left(\frac{P}{P_y} - \frac{A_w}{A} \right)^2}{\left(1 - \frac{A_w}{A} \right)^2} \right] \quad (3.31)$$

3.1.2 Structural T Section

The expressions obtained for the W sections are slightly modified to obtain the reduced moment capacity of T sections. It is assumed that the reduced plastic moment capacity of a T section about its weak axis is equivalent to that of a W section with identical web depth and a flange thickness equal to half of that of a T section as shown in Fig 3.7. Thus, replacing the thickness of the flange (t_f) by ($t_f/2$), in Eqns. (3.16) and (3.31), the relationships between the moment and axial force (reduced plastic moment capacity) for a T section are calculated as;

$$\frac{M}{M_p} = 1 - \frac{A^2}{4(d_w + t_f)Z} \left(\frac{P}{P_y} \right)^2 \quad (3.32)$$

for the case where the axial force is confined within the web and;

$$\frac{M_{pr}}{M_p} = \frac{b_f^2 t_f}{4Z} \left[1 - \frac{\left(\frac{P}{P_y} - \frac{A_w}{A} \right)^2}{\left(1 - \frac{A_w}{A} \right)^2} \right] \quad (3.33)$$

for the case where the axial force has penetrated into the flanges.

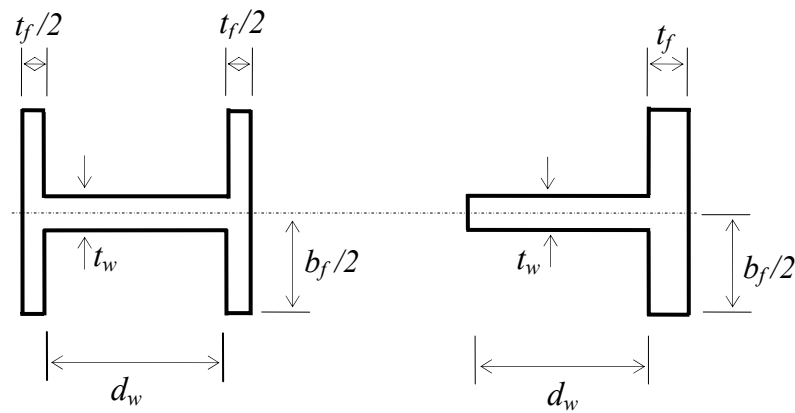


Fig. 3.7 W and T sections

3.1.3 Double Channel Section

The distribution of fully plastic stresses on the cross-section of a double channel section is demonstrated in Fig. 3.8 below

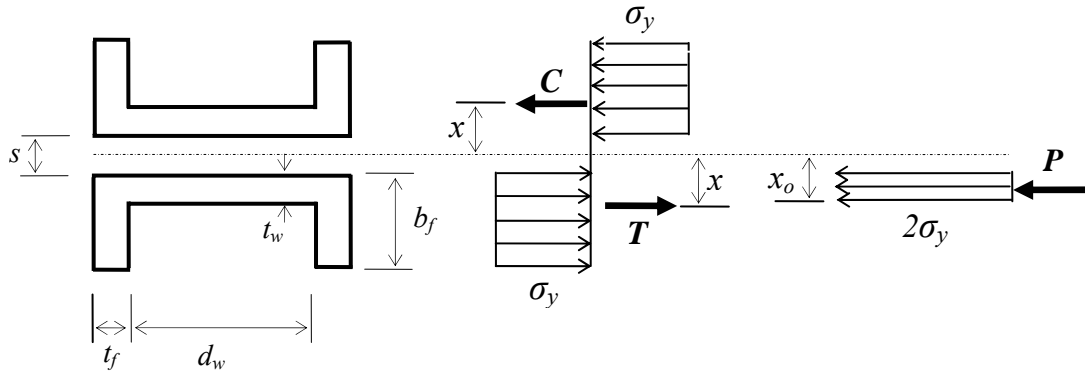


Fig. 3.8 Plastic stress distribution in double-channel section

For a double-channel section, the compression (C) and tensile (T) force resultants of the stress block when the section attains its full plastic moment capacity in the absence of axial load are calculated as:

$$C = T = \sigma_y A \quad (3.34)$$

where A is the area of one channel and expressed as;

$$A = 2b_f t_f + t_w d_w \quad (3.35)$$

Substituting the above equation into Eqn. (3.34)

$$C = T = (2b_f t_f + t_w d_w) \sigma_y \quad (3.36)$$

The distance between the forces and axis of symmetry, x , can be calculated as follows,

$$x = \frac{t_w d_w \left(\frac{t_w}{2} + \frac{s}{2} \right) + 2b_f t_f \left(\frac{b_f}{2} + \frac{s}{2} \right)}{t_w d_w + 2b_f t_f} \quad (3.37)$$

Substituting Eqns. (3.36) and (3.37) into Eqn. (3.1), the plastic moment capacity, M_p , of this section is obtained as;

$$M_p = [t_w d_w (t_w + s) + 2b_f t_f (b_f + s)] \quad (3.38)$$

For the case where an axial force is also acting on the cross-section, one must consider two possible cases for the weak axis bending double channel sections;

1. The effect of the axial force P is confined within the web area
2. The effect of the axial force P has penetrated into the flange area

3.1.3.1 Axial Force Effect Confined Within the Web Area

Fig. 3.9 below demonstrates the stress distribution on one side of the centroid of the cross-section due to the applied axial load. Note that the intensity of the stress block is set at $2\sigma_y$. The moment of this half stress block about the centroid of the cross-section represents the part of the plastic moment capacity consumed by the axial load. This is done to facilitate the calculation of the reduced plastic moment capacity of the section.

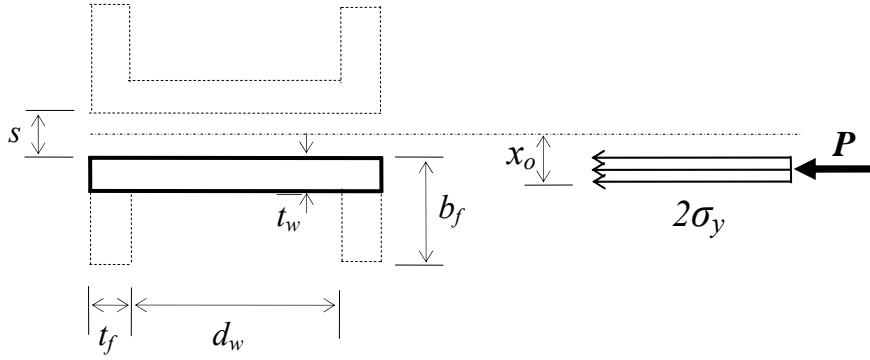


Fig. 3.9 Axial force effect is confined to web (Double channel)

If the effect of the axial force P is only confined to the web area, the relationship between the moment and axial force can be calculated as follows (Fig.3.9);

$$P = 2\sigma_y \left(x_0 - \frac{s}{2} \right) (d_w + 2t_f) \quad (3.39)$$

The moment, M , of the axial force about the axis of symmetry is obtained as

$$M = P \left(x_0 + \frac{s}{4} \right) \quad (3.40)$$

Substituting Eqn.(3.39) into the Eqn.(3.40)

$$M = \sigma_y \left(x_0 - \frac{s}{2} \right) \left(x_0 + \frac{s}{4} \right) (d_w + 2t_f) \quad (3.41)$$

Now, substituting Eqn. (3.41) into Eqn. (3.2), the reduced plastic moment capacity of the section is obtained as;

$$M_{pr} = M_p - \left(x_0 - \frac{s}{2}\right) \left(x_0 + \frac{s}{2}\right) (d_w + 2t_f) \sigma_y \quad (3.42)$$

Next, the axial yield force, P_y is defined as follows;

$$P_y = \sigma_y A \quad (3.43)$$

From Eqns. (3.43) and (3.39), x_0 can be expressed in the following form;

$$x_0 = \frac{s}{2} + \frac{A}{2(d_w + 2t_f)} \left(\frac{P}{P_y}\right) \quad (3.44)$$

Substituting Eqn. (3.44) into Eqn. (3.42), the reduced plastic moment capacity of the section is obtained as a function of the axial load to yield axial load ratio as;

$$M_{pr} = M_p - \left[\frac{A}{2} \left(\frac{P}{P_y}\right)\right] \left[s + \frac{A}{2(d_w + 2t_f)} \left(\frac{P}{P_y}\right) \right] \sigma_y \quad (3.45)$$

Finally, substituting Eqn. (3.15) in to the above equation and rearranging, the relationship between M_{pr} and P is obtained as follows;

$$\frac{M_{pr}}{M_p} = 1 - \frac{\left[\frac{A}{2} \left(\frac{P}{P_y}\right)\right] \left[\frac{A}{2(d_w + 2t_f)} \left(\frac{P}{P_y}\right) + s \right]}{Z} \quad (3.46)$$

3.1.3.2 Axial Force Effect Penetrated into the Flange

If the axial force is penetrated into the flange, a procedure similar to that used in the previous sections can be applied to calculate the reduced plastic moment capacity of the section. Fig. 3.10 below demonstrates the stress distribution on one side of the centroid of the cross-section due to the applied axial load. This stress distribution with an intensity of $2\sigma_y$ is again used to facilitate the calculation of the reduced plastic moment capacity of the section due to the presence of the axial load.

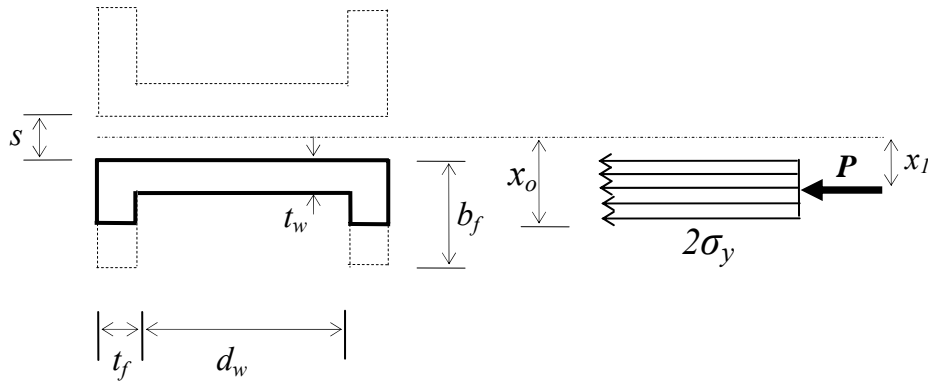


Fig. 3.10 Axial force effect has penetrated into flange (double channel)

From Fig. 3.10

$$P = 2\sigma_y \left[t_w d_w + 2 \left(x_0 - \frac{s}{2} \right) t_f \right] \quad (3.47)$$

The distance between the axial force and axis of symmetry, x_l is expressed as

$$x_1 = \frac{d_w t_w \left(\frac{t_w}{2} + \frac{s}{2} \right) + 2 \left(x_0 - \frac{s}{2} \right) t_f \left(\frac{x_0}{2} + \frac{s}{4} \right)}{d_w t_w + 2 \left(x_0 - \frac{s}{2} \right) t_f} \quad (3.48)$$

The moment, M , which is produced by the axial load is then calculated as follows;

$$M = P x_1 \quad (3.49)$$

Substituting Eqns. (3.47) and (3.48) into Eqn. (3.49), the moment produced by the axial load is calculated as;

$$M = \left[d_w t_w (t_w + s) + 2 \left(x_0 - \frac{s}{2} \right) \left(x_0 + \frac{s}{2} \right) t_f \right] \sigma_y \quad (3.50)$$

Substituting Eqns. (3.38) and (3.50) into Eqn. (3.2), the reduced plastic moment, M_{pr} is obtained as follows:

$$M_{pr} = \left[2 b_f t_f (b_f + s) - 2 \left(x_0 - \frac{s}{2} \right) \left(x_0 + \frac{s}{2} \right) t_f \right] \sigma_y \quad (3.51)$$

Now, the axial yield force, P_y , of the section is calculated as;

$$P_y = \sigma_y A \quad (3.52)$$

From Eqn. (3.47) and Eqn.(3.52), x_0 can be expressed in the following form;

$$x_0 = \frac{A}{4 t_f} \left(\frac{P}{P_y} - \frac{d_w t_w}{A} \right) + \frac{s}{2} \quad (3.53)$$

Also note that the area of the web, A_w is equal to;

$$A_w = t_w d_w \quad (3.54)$$

Now, substituting Eqn. (3.54) into Eqn. (3.53), x_0 can be expressed as;

$$x_0 = \frac{A}{4t_f} \left(\frac{P}{P_y} - \frac{A_w}{A} \right) + \frac{s}{2} \quad (3.55)$$

Next, substituting Eqn. (3.55) into Eqn.(3.51), M_{pr} is expressed as;

$$M_{pr} = \left\{ 2bt_f(b+s) - \frac{A}{2} \left(\frac{P}{P_y} - \frac{A_w}{A} \right) \left[s + \frac{A}{4t_f} \left(\frac{P}{P_y} - \frac{A_w}{A} \right) \right] \right\} \sigma_y \quad (3.56)$$

The area of the flange, A_f , is presented in terms of the section properties as follows;

$$A_f = A - A_w = 4bt_f \quad (3.57)$$

From the above equation the thickness of the flange, t_f is expressed as;

$$t_f = \frac{A - A_w}{4b} \quad (3.58)$$

Substituting Eqn. (3.58) into Eqn. (3.56), the reduced moment capacity of the section is expressed as;

$$M_{pr} = \left\{ \frac{A - A_w}{2} (s+b) - \frac{A}{2} \left(\frac{P}{P_y} - \frac{A_w}{A} \right) \left[s + b \left(\frac{\frac{P}{P_y} - \frac{A_w}{A}}{1 - \frac{A_w}{A}} \right) \right] \right\} \sigma_y \quad (3.59)$$

Finally, substituting Eqn. (3.15) into the above equation and rearranging, the relationship between the M_{pr} and M_p is obtained as follows;

$$\frac{M_{pr}}{M_p} = \frac{A}{2Z} \left\{ \left(1 - \frac{A_w}{A} \right) (s + b) - \left(\frac{P}{P_y} - \frac{A_w}{A} \right) \left[s + b \frac{\left(\frac{P}{P_y} - \frac{A_w}{A} \right)}{\left(1 - \frac{A_w}{A} \right)} \right] \right\} \quad (3.60)$$

3.1.4 Double Angle Section

The expressions obtained for the double-channel sections are slightly modified to obtain the reduced plastic moment capacity of double-angle sections. It is assumed that the reduced plastic moment capacity of a double-angle section about its weak axis is equivalent to that of a double-channel section with identical web depth and a flange thickness equal to half of that of a double-angle section as shown in Fig 3.11. Thus, replacing the thickness of the flange (t_f) by ($t_f/2$), in Eqns. (3.46) and (3.60), the relationships between the moment and axial force (reduced plastic moment capacity) for a double-angle section are calculated as;

$$\frac{M_{pr}}{M_p} = 1 - \frac{\left[\frac{A \left(\frac{P}{P_y} \right)}{2} \right] \left[\frac{A}{2(d_w + t_f)} \left(\frac{P}{P_y} \right) + s \right]}{Z} \quad (3.61)$$

for the case where the axial force is confined within the web and;

$$\frac{M_{pr}}{M_p} = \frac{A}{2Z} \left\{ \left(1 - \frac{A_w}{A} \right) (s + b) - \left(\frac{P}{P_y} - \frac{A_w}{A} \right) \left[s + b \frac{\left(\frac{P}{P_y} - \frac{A_w}{A} \right)}{\left(1 - \frac{A_w}{A} \right)} \right] \right\} \quad (3.62)$$

For a box section, the compression (C) and tensile (T) force resultants of the stress block when the section attains its full plastic moment capacity in the absence of axial load are calculated as;

$$C = T = \sigma_y \frac{A}{2} \quad (3.63)$$

Where A is the area of the box section expressed as;

$$A = 2t(b + d) \quad (3.64)$$

Substituting Eqn. (3.64) into Eqn. (3.63),

$$C = T = t(b + d)\sigma_y \quad (3.65)$$

The distance between the forces and the axis of symmetry, x , can be calculated as follows,

$$x = \frac{bt\left(\frac{t}{2} + \frac{d}{2}\right) + 2\frac{d}{2}t\frac{d}{4}}{(b + d)t} \quad (3.66)$$

Substituting Eqns. (3.63) and (3.64) into Eqn. (3.1), the plastic moment capacity, M_p , of this section is obtained as;

$$M_p = \left[bt(t + d) + \frac{d^2t}{2} \right] \sigma_y \quad (3.67)$$

For the case where an axial force is also acting on the cross-section, one must consider two possible cases for box sections;

1. The effect of the axial force P is confined within the web area
2. The effect of the axial force P has penetrated into the flanges

3.1.5.1 Axial Force Effect Confined Within the Web Area

Fig. 3.13 below demonstrates the stress distribution on one side of the centroid of the cross-section due to the applied axial load. Note that the intensity of the stress block is set at $2\sigma_y$. The moment of this half stress block about the centroid of the cross-section represents the part of the plastic moment capacity consumed by the axial load. This is again done to facilitate the calculation of the reduced plastic moment capacity of the section.

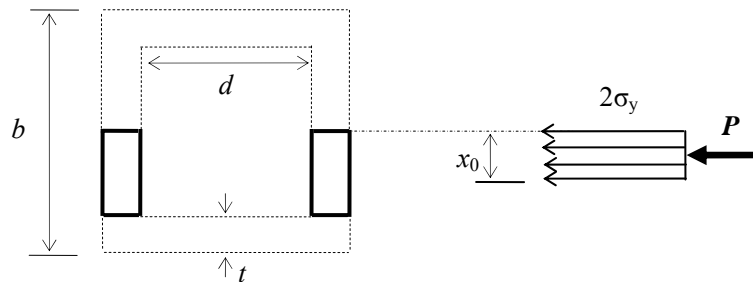


Fig. 3.13 Axial force effect is confined to the web (Box Section)

If the effect of the axial force, P is only confined to the web area, the relationship between the moment and axial force can be calculated as follows (Fig.3.5);

$$P = 4\sigma_y x_0 t \quad (3.68)$$

The moment, M , of the axial force P about the axis of symmetry is obtained as;

$$M = P \frac{x_0}{2} \quad (3.69)$$

Substituting Eqn. (3.68) into Eqn. (3.69)

$$M = 2x_0^2 t \sigma_y \quad (3.70)$$

Now, substituting the above equation into Eqn. (3.2), the reduced plastic moment capacity of the section is obtained as;

$$M_{pr} = M_p - 2x_0^2 t \sigma_y \quad (3.71)$$

Next, the yield force, P_y is defined as follows;

$$P_y = \sigma_y A \quad (3.72)$$

From Eqns. (3.68) and (3.72), x_0 can be expressed in the following form;

$$x_0 = \frac{A}{4t} \left(\frac{P}{P_y} \right) \quad (3.73)$$

Substituting Eqn. (3.73) into Eqn. (3.71), the reduced plastic moment capacity of the section is obtained as a function of the axial load to yield axial load ratio as;

$$M_{pr} = M_p - \frac{A^2}{8t} \left(\frac{P}{P_y} \right)^2 \sigma_y \quad (3.74)$$

Finally, substituting Eqn. (3.15) into the above equation and rearranging, the relationship between M_{pr} and P is obtained as follows;

$$\frac{M_{pr}}{M_p} = 1 - \frac{A^2}{8tZ} \left(\frac{P}{P_y} \right)^2 \quad (3.75)$$

3.1.5.2 Axial Force Effect Penetrated into the Flanges

If the axial force has penetrated into the flange, a procedure similar to that used in the previous sections can be applied to calculate the reduced plastic moment capacity of the section. Fig. 3.14 below demonstrates the stress distribution on one side of the centroid of the cross-section due to the applied axial load. This stress distribution with an intensity of $2\sigma_y$ is again used to facilitate the calculation of the reduced plastic moment capacity of the section due to the presence of the axial load.

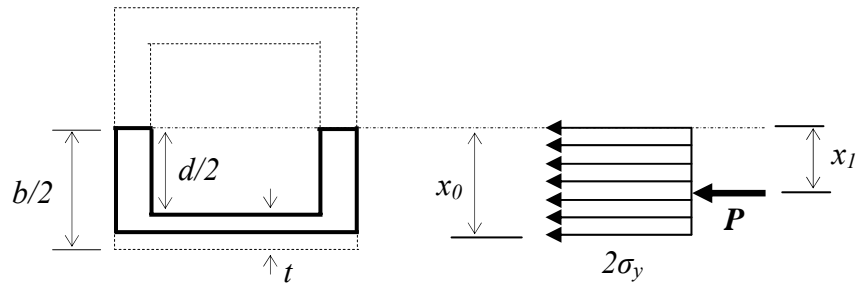


Fig. 3.14 Axial force effect has penetrated into the flange (box section)

From Fig. (3.14)

$$P = 2\sigma_y \left[b \left(x_0 - \frac{d}{2} \right) + dt \right] \quad (3.76)$$

Distance between the axial force and axis of symmetry, x_1 is expressed as;

$$x_1 = \frac{dt\left(\frac{d}{4}\right) + \frac{b}{2}\left(x_0 - \frac{d}{2}\right)\left(x_0 + \frac{d}{2}\right)}{b\left(x_0 - \frac{d}{2}\right) + dt} \quad (3.77)$$

The moment, M , which is produced by the axial load is then calculated as follows;

$$M = Px_1 \quad (3.78)$$

Substituting Eqns. (3.76) and (3.77) into Eqn. (3.78), the moment produced by the axial load is calculated as;

$$M = \left[\frac{d^2t}{2} + b\left(x_0 - \frac{d}{2}\right)\left(x_0 + \frac{d}{2}\right) \right] \sigma_y \quad (3.79)$$

Substituting Eqns. (3.79) and (3.67) into Eqn. (3.2), the reduced plastic moment capacity of the section is expressed as;

$$M_{pr} = \left[bt(t+d) - b\left(x_0^2 - \frac{d^2}{4}\right) \right] \sigma_y \quad (3.80)$$

Note that the thickness, t of the section is equal to;

$$t = \frac{b-d}{2} \quad (3.81)$$

Substituting Eqn. (3.81) into Eqn. (3.80), the reduced plastic moment capacity of the section is expressed as;

$$M_{pr} = b\left(\frac{b}{2} - x_0\right)\left(\frac{b}{2} + x_0\right) \sigma_y \quad (3.82)$$

Now, the axial yield force P_y of the section is calculated as;

$$P_y = \sigma_y A \quad (3.83)$$

From Eqns. (3.76) and (3.83), x_0 can be expressed in the following form;

$$x_0 = \frac{d^2}{2b} + \frac{A}{2b} \left(\frac{P}{P_y} \right) \quad (3.84)$$

Next, substituting Eqn. (3.84) into Eqn. (3.82), the reduced plastic moment capacity of the section is expressed as;

$$M_{pr} = b \left[\frac{b^2 - d^2}{2b} - \frac{A}{2b} \left(\frac{P}{P_y} \right) \right] \left[\frac{b^2 + d^2}{2b} + \frac{A}{2b} \left(\frac{P}{P_y} \right) \right] \quad (3.85)$$

Also note that the area A of the box section is expressed as;

$$A = b^2 - d^2 \quad (3.86)$$

From the above equation, the following relationship can be built;

$$2b^2 - A = b^2 + d^2 \quad (3.87)$$

Substituting Eqns. (3.86) and (3.87) into Eqn. (3.85), M_{pr} is expressed as

$$M_{pr} = \frac{A}{2} \left(1 - \frac{P}{P_y} \right) \left[b - \frac{A}{2b} \left(1 - \frac{P}{P_y} \right) \right] \sigma_y \quad (3.88)$$

Finally, substituting Eqn. (3.15) into the above equation and rearranging, the relationship between the M_{pr} and P is obtained as follows;

$$\frac{M_{pr}}{M_p} = \frac{A}{2Z} \left(1 - \frac{P}{P_y} \right) \left[b - \frac{A}{2b} \left(1 - \frac{P}{P_y} \right) \right] \quad (3.89)$$

3.1.6 Pipe Section

The distribution of fully plastic stresses on the cross-section of a pipe section is demonstrated in Fig. 3.15 below

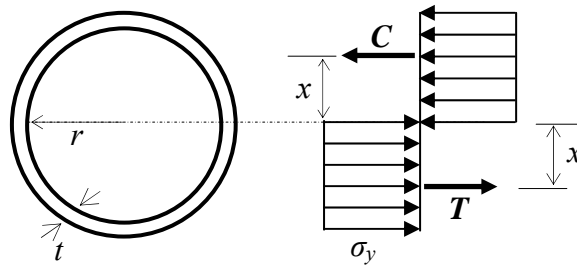


Fig. 3.15 Bending effect (Pipe section)

For a pipe section, the compression (C) and tensile (T) force resultants of the stress block when the section attains its full plastic moment capacity in the absence of axial load are calculated as;

$$C = T = \sigma_y \frac{A}{2} \quad (3.90)$$

where A is the area of the cross section expressed as;

$$A = 2\pi r t \quad (3.91)$$

In the above equation r is the radius of pipe. Substituting Eqn. (3.91) into Eqn. (3.90)

$$C = T = \pi r t \sigma_y \quad (3.92)$$

The distance between the forces and the centroid of the section is expressed as;

$$x = \frac{2r}{\pi} \quad (3.93)$$

Substituting Eqns. (3.92) and (3.93) into Eqn. (3.1), the plastic moment capacity, M_p , of this section is obtained as;

$$M_p = 4r^2 t \sigma_y \quad (3.94)$$

The portion of the plastic moment capacity which is consumed by the axial force (Fig. 3.16), P , can be calculated as follows;

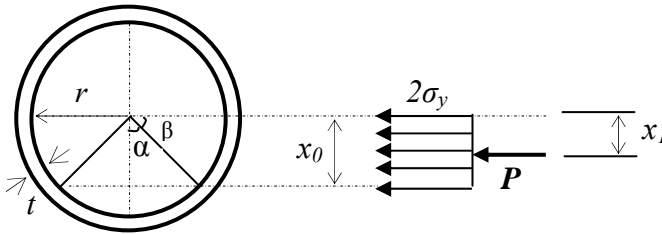


Fig. 3.16 Axial force effect (Pipe section)

From Fig. (3.16), the axial force P is obtained as:

$$P = 4\beta r t \sigma_y \quad (3.95)$$

Next, the yield axial force, P_y , is defined as follows;

$$P_y = \sigma_y A \quad (3.96)$$

From Eqns. (3.91) and (3.92), the angle, β , is expressed as follows;

$$\beta = \frac{\pi}{2} \frac{P}{P_y} \quad (3.97)$$

The distance between the axial force and the centroid is obtained as;

$$x_1 = \frac{\frac{2r}{\pi} (\pi r t) - 2\alpha r t \left(\frac{r \sin(\alpha)}{\alpha} \right)}{\pi r t - 2\alpha r t} \quad (3.98)$$

Simplifying the above equation, x_1 is expressed as;

$$x_1 = \frac{r[1 - \sin(\alpha)]}{\frac{\pi}{2} - \alpha} \quad (3.99)$$

The moment, M , which is produced by the axial load is then calculated as follows;

$$M = P x_1 \quad (3.100)$$

Substituting Eqns. (3.91) and (3.96) into the Eqn. (3.97)

$$M = \frac{r[1 - \sin(\alpha)]}{\frac{\pi}{2} - \alpha} 4\beta r t \sigma_y \quad (3.101)$$

Also note that, α is expressed as;

$$\alpha = \frac{\pi}{2} - \beta \quad (3.102)$$

Substituting Eqn. (3.102) into Eqn. (3.101), the moment due to the axial load is obtained as;

$$M = 4r^2t \left[1 - \sin\left(\frac{\pi}{2} - \beta\right) \right] \sigma_y \quad (3.103)$$

Next, substituting Eqn.(3.97) into Eqn.(3.103), M is expressed as;

$$M = 4r^2t \left[1 - \sin\left(\frac{\pi}{2} - \frac{\pi P}{2 P_y}\right) \right] \quad (3.104)$$

Simplifying the above equation, M is obtained as follows;

$$M = 4r^2t \left[1 - \cos\left(\frac{\pi P}{2 P_y}\right) \right] \quad (3.105)$$

Substituting Eqns. (3.94) and (3.105) into Eqn. (3.2), the reduced plastic moment capacity of the section is expressed as;

$$M_{pr} = 4r^2t\sigma_y - 4r^2t \left[1 - \cos\left(\frac{\pi P}{2 P_y}\right) \right] \sigma_y \quad (3.106)$$

Simplifying the above equation, M_{pr} is expressed as follows;

$$M_{pr} = 4r^2t \cos\left(\frac{\pi P}{2 P_y}\right) \sigma_y \quad (3.107)$$

Finally, substituting Eqn. (3.15) into the above equation and rearranging, the relationship between M_{pr} and P is obtained as follows;

$$\frac{M_{pr}}{M_p} = \cos\left(\frac{\pi P}{2 P_y}\right) \quad (3.108)$$

3.2 Comparison of the Moment Axial Force Interaction Relationships

A summary of moment axial force interaction relationship equations derived for various sections are given in Tables 3.1 and 3.2 for the cases where the axial force is confined within the web and penetrated in to the flanges respectively. Fig. 3.17 presents the moment-axial force interaction relationships for various section shapes with similar cross-sectional areas. The figure is plotted using the normalized equations derived above.

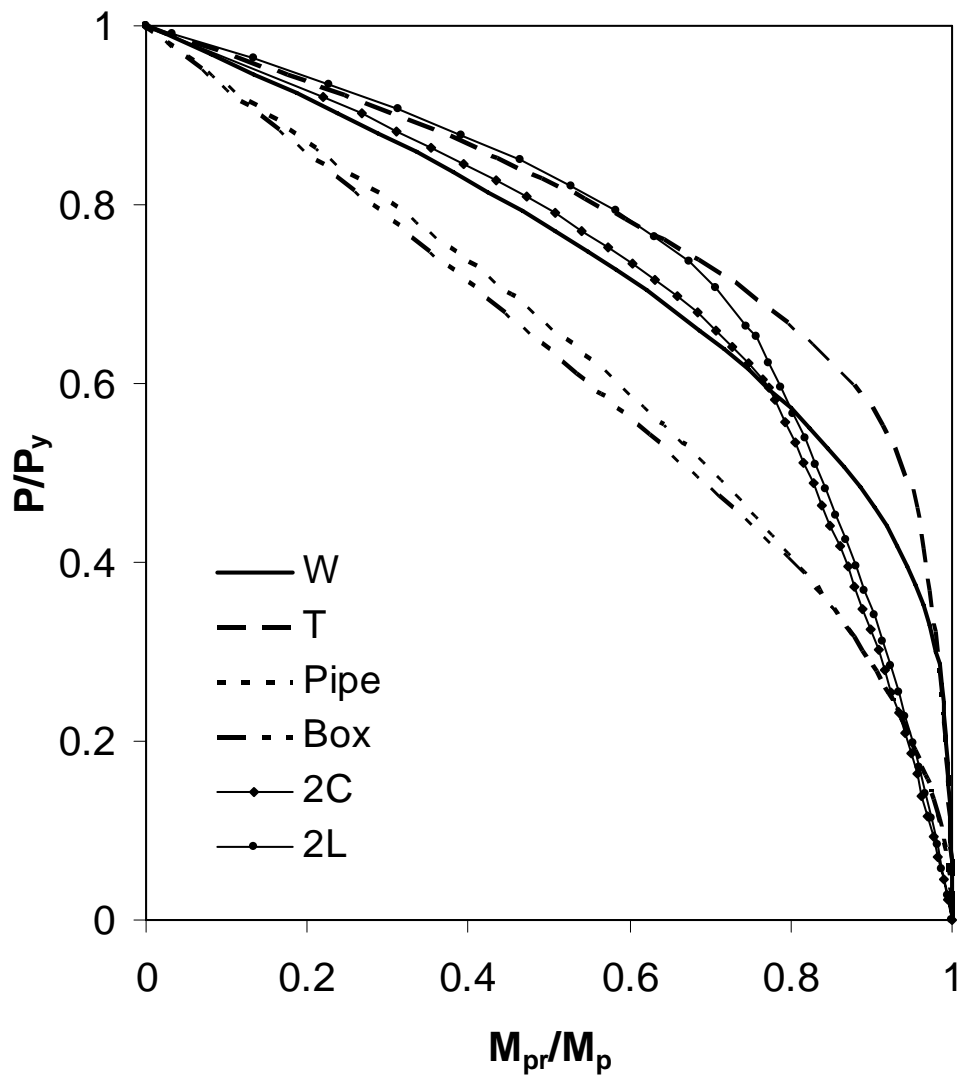


Fig. 3.17 Moment-Axial Force interaction diagram for various sections

Table 3.1 Weak axis bending, P - M_{pr} interaction relations for different sections
(Axial force is only confined to the web area)

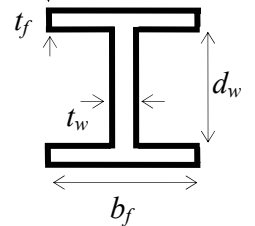
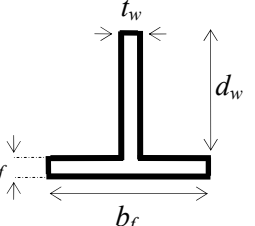
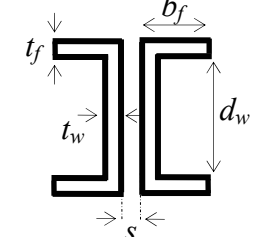
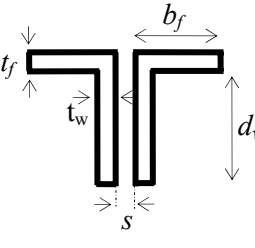
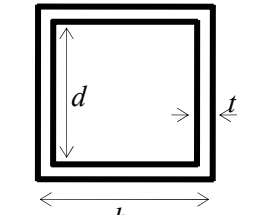
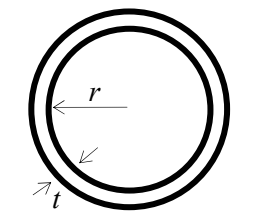
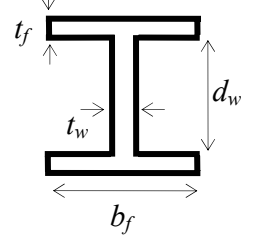
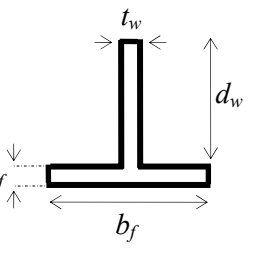
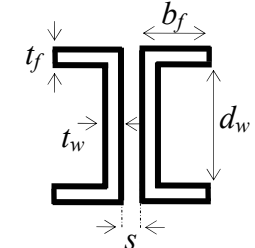
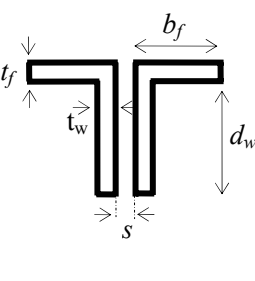
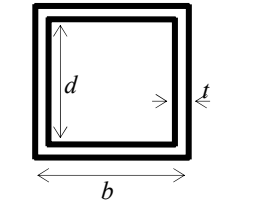
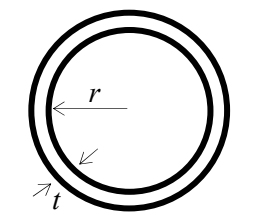
	$\frac{M_{pr}}{M_p} = 1 - \frac{A^2}{4(d_w + 2t_f)Z} \left(\frac{P}{P_y} \right)^2$
	$\frac{M_{pr}}{M_p} = 1 - \frac{A^2}{4(d_w + t_f)Z} \left(\frac{P}{P_y} \right)^2$
	$\frac{M_{pr}}{M_p} = 1 - \frac{\left[\frac{A}{2} \left(\frac{P}{P_y} \right) \right] \left[\frac{A}{2(d_w + 2t_f)} \left(\frac{P}{P_y} \right) + s \right]}{Z}$
	$\frac{M_{pr}}{M_p} = 1 - \frac{\left[\frac{A}{2} \left(\frac{P}{P_y} \right) \right] \left[\frac{A}{2(d_w + t_f)} \left(\frac{P}{P_y} \right) + s \right]}{Z}$
	$\frac{M_{pr}}{M_p} = 1 - \frac{A^2}{8tZ} \left(\frac{P}{P_y} \right)^2$
	$\frac{M_{pr}}{M_p} = \text{Cos} \left[\frac{\pi}{2} \left(\frac{P}{P_y} \right) \right]$

Table 3.2 Weak axis bending, P - M_{pr} interaction relations for different sections
(Axial force has penetrated into the flange area)

	$\frac{M_{pr}}{M_p} = \frac{b_f^2 t_f}{2Z} \left[1 - \frac{\left(\frac{P}{P_y} - \frac{A_w}{A} \right)^2}{\left(1 - \frac{A_w}{A} \right)^2} \right]$
	$\frac{M_{pr}}{M_p} = \frac{b_f^2 t_f}{4Z} \left[1 - \frac{\left(\frac{P}{P_y} - \frac{A_w}{A} \right)^2}{\left(1 - \frac{A_w}{A} \right)^2} \right]$
	$\frac{M_{pr}}{M_p} = \frac{A}{2Z} \left\{ \left(1 - \frac{A_w}{A} \right) \left(\frac{s}{2} + \frac{b_f}{2} \right) - \left(\frac{P}{P_y} - \frac{A_w}{A} \right) \left[\frac{s}{2} + \frac{b_f}{2} \left(\frac{\frac{P}{P_y} - \frac{A_w}{A}}{1 - \frac{A_w}{A}} \right) \right] \right\}$
	$\frac{M_{pr}}{M_p} = \frac{A}{2Z} \left\{ \left(1 - \frac{A_w}{A} \right) \left(\frac{s}{2} + \frac{b_f}{2} \right) - \left(\frac{P}{P_y} - \frac{A_w}{A} \right) \left[\frac{s}{2} + \frac{b_f}{2} \left(\frac{\frac{P}{P_y} - \frac{A_w}{A}}{1 - \frac{A_w}{A}} \right) \right] \right\}$
	$\frac{M_{pr}}{M_p} = \frac{A}{2Z} \left(1 - \frac{P}{P_y} \right) \left[b - \frac{A}{2b} \left(1 - \frac{P}{P_y} \right) \right]$
	$\frac{M_{pr}}{M_p} = \text{Cos} \left[\frac{\pi}{2} \left(\frac{P}{P_y} \right) \right]$

CHAPTER 4

ANALYTICAL SIMULATION OF HYSTERETIC BEHAVIOR OF STEEL BRACES

In this chapter, an analytical model is developed to enable the formulation of the inelastic buckling behavior of steel braces within each hysteretic zone. The model employs (i) a large displacement analysis procedure to account for the second order effects due to the presence of axial loads and transverse deformations of the brace and (ii) inelastic axial and bending behavior of the brace to simulate the plastic hinge formation at the mid-length of the brace upon inelastic buckling. In this study it is assumed that the plastic hinge has elasto-perfectly plastic mechanical properties and thus, forms instantaneously when the reduced plastic moment capacity of the section is attained at the buckling load. Moreover, the analytical model is developed for pin-pin ended braces. Thus, it may not be used to accurately simulate the inelastic cyclic buckling behavior of braces with other end conditions such as fixed-pinned or fixed-fixed.

4.1 Proposed Analytical Model

In the model, an initial eccentricity, e , is introduced at the end of the brace member to produce an initial imperfection that will produce buckling as demonstrated in Fig.4.1. Then, a plastic hinge with a moment-axial force interaction capability is placed at the mid-length of the brace element. The initial eccentricity is chosen such that when the axial load reaches the buckling load P_b of the brace, the reduced

plastic moment capacity M_{pr} corresponding to the buckling load is reached as well. Beyond this point, the axial load capacity of the member constantly decreases due to the combined effects of second order moments and moment-axial force interaction as the member folds. For the model to work as intended the initial eccentricity must be known. The derivation of this initial eccentricity is outlined in the diction below. In the derivation of the analytical equations, compressive loads (e.g. buckling load is negative) and axial shortenings are assumed to be negative.

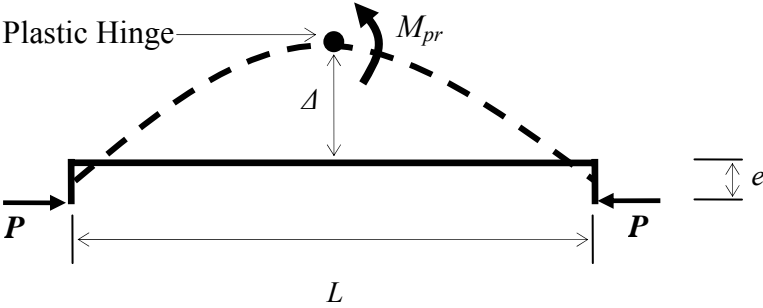


Fig. 4.1 Brace Buckling Model

4.1.1 Derivation of Brace Initial Eccentricity

It is assumed that the deformed shape of the brace prior to buckling can be approximated by a sinusoidal function of the form given in Eq. (4.1) and displayed in Fig. 4.2 below.

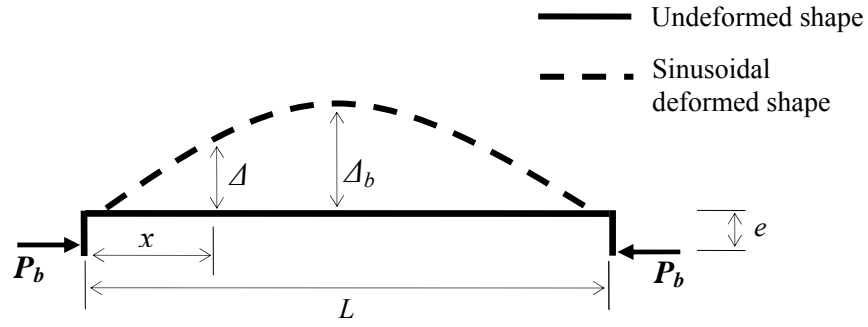


Fig. 4.2 Approximated deformed shape

From Fig. 4.2, the transverse displacement (Δ) at a location x from the left end of the brace can be expressed as the following form;

$$\Delta = \Delta_b \text{Sin}\left(\frac{\pi}{L} x\right) \quad (4.1)$$

where, Δ_b is the maximum transverse displacement at buckling. The displacement, Δ_b , can be calculated using the unit dummy load method (Popov, 1999).

$$\Delta_b = 2 \int_0^{L/2} \frac{Mm}{EI} dx \quad (4.2)$$

Where, E and I are respectively the modulus of elasticity and moment of inertia about the buckling axis of the brace. M is the second order moment at the buckling load and m is the moment due to the unit dummy load applied at the location and in the direction of the displacement to be calculated. From Fig. 4.3 M is expressed as;

$$M = -P_b \left[e + \Delta_b \text{Sin}\left(\frac{\pi}{L} x\right) \right] \quad (4.3)$$

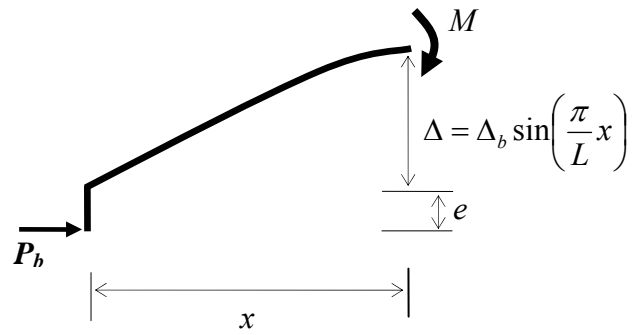


Fig. 4.3 Free body diagram for M

From Figs. 4.4a and 4.4b the moment, m , due to the unit dummy load is calculated as;

$$m = \frac{x}{2} \tag{4.4}$$

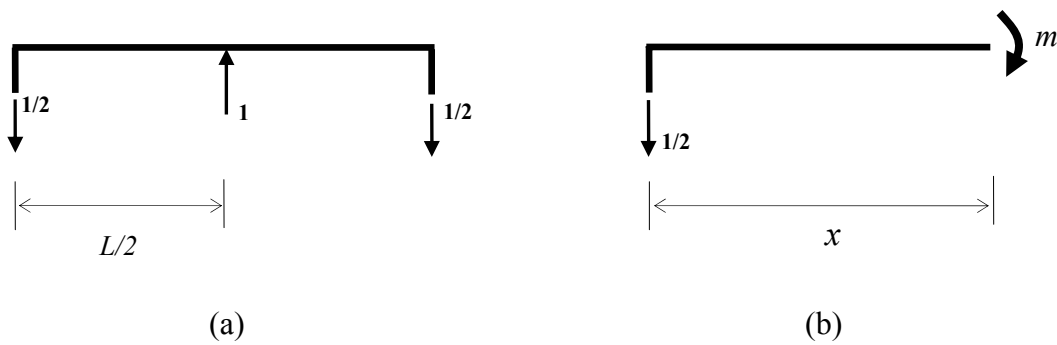


Fig. 4.4 (a) Unit dummy load at the center (b) Free body diagram due to the unit load.

Substituting the values of M and m from Eqns. (4.3) and (4.4) into Eqn. (4.2) and integrating;

$$\Delta_b = \frac{-L^2 P_b (e\pi^2 + 8\Delta_b)}{8\pi^2 EI} \quad (4.5)$$

Thus, from the above equation Δ_b is obtained as;

$$\Delta_b = -\frac{L^2 P_b}{8EI \left(1 + \frac{P_b L^2}{\pi^2 EI}\right)} e \quad (4.6)$$

When the axial load is equal to the buckling load, the second order moment at the vertex of the brace element is equal to the reduced plastic moment, M_{pr} , of the brace. Accordingly, from Fig. 4.2 the following expression is formulated;

$$-P_b(e + \Delta_b) = M_{pr} \quad (4.7)$$

From the above equation, e is expressed as:

$$e = -\frac{M_{pr}}{P_b} - \Delta_b \quad (4.8)$$

Substituting Eqn. (4.6) into Eqn. (4.8) and rearranging, e is obtained as follows;

$$e = -\frac{M_{pr}}{P_b \left(1 - \frac{L^2 P_b}{8EI \left(1 + \frac{L^2 P_b}{\pi^2 EI}\right)}\right)} \quad (4.9)$$

Note that in the above equations, P_b needs to be taken as negative since it is an axial compressive load.

4.2 Analytical Formulations

In this section, the brace axial force-displacement relationships are formulated for each one of the hysteretic zones defined in Chapter 2. In the derivation of the analytical equations for each hysteretic zone, the deformed shape of the brace which was earlier assumed to have a sinusoidal shape (Fig.4.2) is simulated by two line segments as illustrated in Fig.4.5. Actually, tests conducted by Black et al.(1980) confirm that the braces deform in the form of two line segments beyond buckling as illustrated Fig.4.6

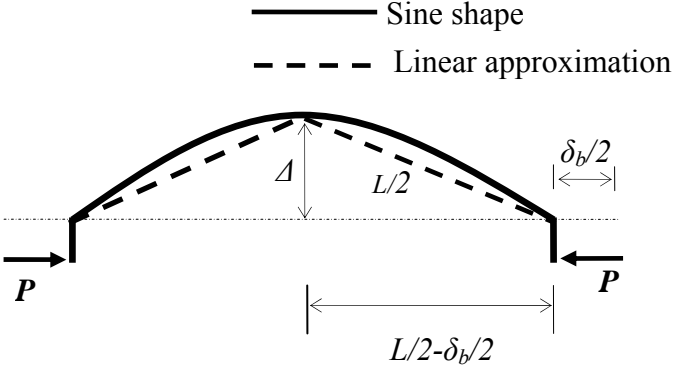


Fig. 4.5 Approximated sine shape by two linear segments.

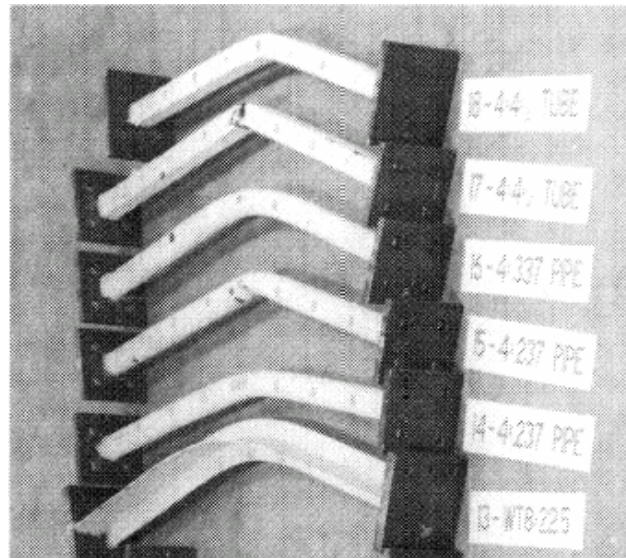


Fig. 4.6 Deformed braces after the completion of the tests (Black et al. 1980)

The total axial displacement δ of the brace results from shortening due to bending effect (δ_b) and axial displacement due to the applied axial force (δ_a). Accordingly;

$$\delta = \delta_a - \delta_b \quad (4.10)$$

Note that in the above equation the axial displacement due to the bending effect is presented as a negative value, since from the geometry of the brace buckling model shown in Fig. 4.5, under compressive or tensile axial load, the axial displacement from bending effect is always negative.

The axial displacement due to the axial force is expressed as;

$$\delta_a = \frac{PL}{AE} \quad (4.11)$$

From the geometry of the deformed brace in Fig. 4.5, the transverse displacement, Δ , of the brace can be obtained as;

$$\Delta = \sqrt{\left(\frac{L}{2}\right)^2 - \left(\frac{L - \delta_b}{2}\right)^2} \quad (4.12)$$

Using the above equation, the axial displacement due to the bending effect, δ_b , is expressed as;

$$\delta_b = L - \sqrt{L^2 - 4\Delta^2} \quad (4.13)$$

Next substituting Eqns. (4.11) and (4.13) into Eqn. (4.10), the total axial displacement, δ , of the brace is obtained as follows;

$$\delta = \frac{PL}{AE} - L + \sqrt{L^2 - 4\Delta^2} \quad (4.14)$$

The above equation will be used to obtain the cyclic axial force-displacement relationship of the brace for each hysteretic zone.

4.2.1 Zone 1

Zone 1 (Segment O-A, in Fig. 2.2a) is associated with the initial compressive loading of a brace which approaches the buckling load at point A. For this elastic range, using Eqn. (4.6) for any axial load level, the transverse displacement Δ can be obtained as follows;

$$\Delta = -\frac{L^2 P}{8EI \left(1 + \frac{P L^2}{\pi^2 EI}\right)} e \quad (4.15)$$

Substituting the above equation into Eqn. (4.14), axial displacement is expressed as;

$$\delta = \frac{PL}{AE} - L + \sqrt{L^2 - 4 \left[\frac{L^2 P}{8EI \left(1 + \frac{PL^2}{\pi^2 EI}\right)} e \right]^2} \quad (4.16)$$

4.2.2 Zone 2

Zone 2 (Segment A-B, in Fig 2.2a) is dominated by the inelastic bending of the brace due to the $P-\Delta$ moments generated by the compressive axial load P . The magnitude of P monotonically decreases with the increasing magnitude of transverse deformation as explained earlier in Chapter 2. To satisfy static moment equilibrium at the mid-length of the brace, the following relationship must be satisfied in reference to Fig.4.5;

$$-P(\Delta + e) = M_{pr} \quad (4.17)$$

Solving the above equation, Δ , is obtained as follows;

$$\Delta = -\frac{M_{pr}}{P} - e \quad (4.18)$$

Next, substituting Eqn. (4.18) into Eqn. (4.14), the axial displacement is expressed as;

$$\delta = \frac{PL}{AE} - L + \sqrt{L^2 - 4\left(-\frac{M_{pr}}{P} - e\right)^2} \quad (4.19)$$

The analytical results obtained for Zones 1 and 2 are compared with the experimental results of Black et al. (1980) in Figs. 4.7 and 4.8 for brace # 3 (W section, $KL/r=80$) and 11 (2C section, $KL/r=120$) respectively. Note that in these figures the first loading cycles are compared for Zones 1 and 2. In the figures, axial force versus axial displacement as well as axial force versus transverse displacement relationships of the analytical and experimental results for the first loading cycles are compared. As observed from the figures a fairly good agreement is found between the analytical and experimental results.

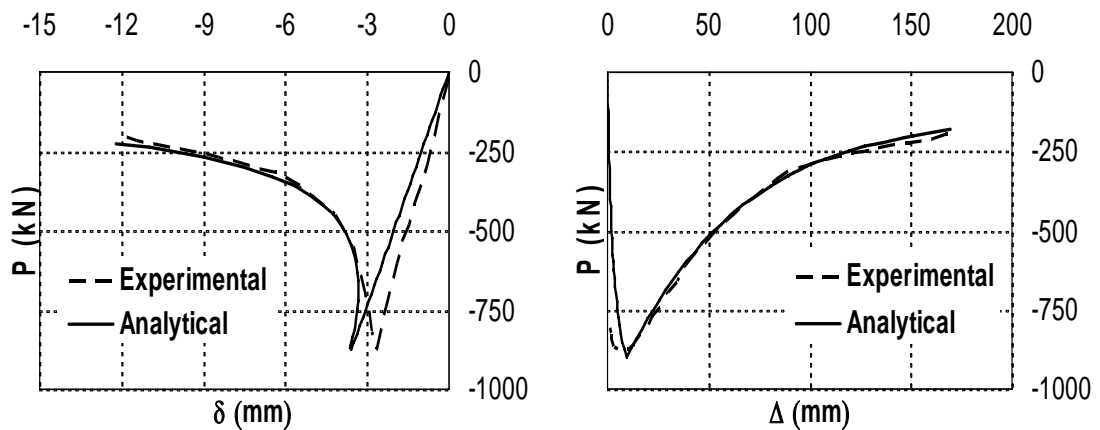


Fig. 4.7 Comparison of experimental and analytical results for Brace 3, Zones 1 and 2; (a) axial force versus axial displacement, (b) axial force versus transverse displacement

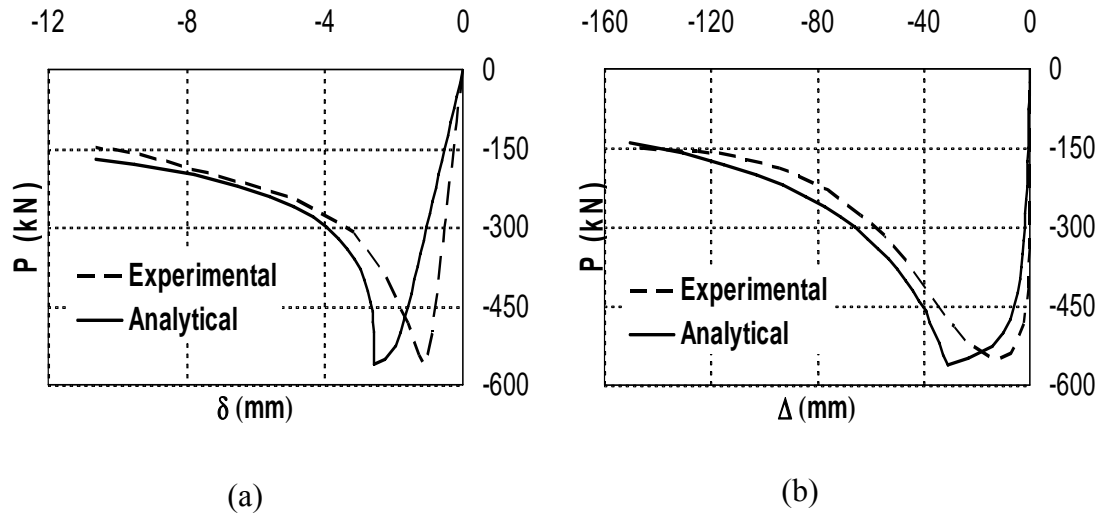


Fig. 4.8 Comparison of experimental and analytical results for Brace 11, Zones 1 and 2; (a) axial force versus axial displacement, (b) axial force versus transverse displacement

4.2.3 Brace Growth Effect

Starting from the end of Zone-2, the brace is subjected to elastic unloading and tension loading. During this process, the brace elongates gradually and straightens. Even though the brace for several cycles is subjected to the same magnitude of maximum tensile force which may be less than the yield force, the axial displacement continues to increase. This causes a progressive lengthening called brace growth. Brace growth effect must be included in the formulation of Zones 3 and 4 to obtain accurate results for the simulation of the inelastic cyclic axial force-displacement behavior of steel braces.

Brace growth phenomenon is shown in Fig.4.9. For the first cycle, although the axial behavior of the brace excluding the transverse deformation effects is totally elastic, there is an apparent translation from Point E', which is the axial displacement of the brace excluding the effect of brace growth, to Point E. For the second cycle, the brace growth corresponds to the distance from Point F to Point K only. Note that the distance between Points E and F is not considered as a growth effect. However, in this case, the plastic axial deformation between points E and F can not be fully recovered since upon unloading from Point F, the buckling of the brace takes place at Point G at an axial load level much smaller than the yield axial force level. This phenomenon, although not considered as a growth effect, contributes to the permanent elongation of the brace length and can directly be considered in the formulation of the axial force-deformation hysteretic relationship of the brace as an unrecovered plastic deformation.

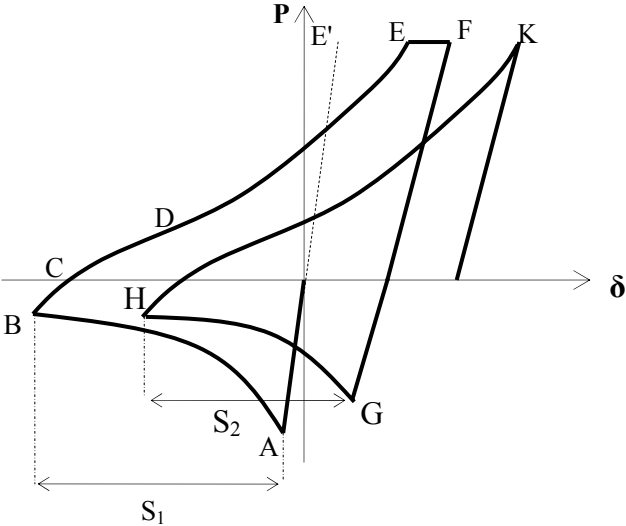


Fig. 4.9 Brace Growth idealization

According to Kahn et al. (1976), Popov et al. (1980), and Goel et al. (1981), the brace growth is proportional to the extent of shortening (S_1 or S_2 in Fig. 4.9) it experienced during previous cycles. Also Popov et al (1981) and Jin and El-Tawil (2003) concluded that the brace growth is directly related to the accumulated plastic strain energy. This energy depends on the cumulative axial plastic displacement in compression and cumulative axial plastic displacement in tension. Since the plastic axial displacement in compression is kinematically related to the transverse plastic displacement of the brace (Popov, 1981), the brace growth effect is assumed to be a function of the cumulative transverse plastic displacement in compression plus the cumulative axial plastic displacement in tension. For example in Fig. 4.9, the transverse displacement in region A-B is responsible for the growth effect between Points E and E' whereas the cumulative transverse displacements in regions A-B and G-H and the plastic axial displacement in region E-F are responsible for the growth effect between points F and K. Methods based on the cumulative plastic strain energy necessitate extra computational steps to include the growth effect in the hysteretic behavior of the braces. Consequently, defining the growth effect as a function of the transverse and plastic axial displacements simplifies the incorporation of this effect in the hysteretic behavior of the braces.

To include the growth effect in the analytical formulations of Zones 3 and 4, the normalized brace growth versus normalized cumulative plastic displacement relationships were calculated using the eleven pin-pin ended braces tested by Black et al. (1980). The properties of these braces are listed in Table 4.1. The test data and computations related to the brace growth effect are given in Appendix A. The normalized brace growth, F_G , called growth factor thereafter, is defined as the difference between the axial displacement, δ_i , at cycle i and the axial displacement δ_{i-1} , at cycle $i-1$ normalized with respect to the elastic displacement, δ_e , corresponding to an axial load range measured from the level of the axial load at the end of Zone 2 (P_2), to the level of the axial load where the growth is measured at the end of Zone 4 (P_4). Thus;

$$F_G = \frac{\delta_i - \delta_{i-1}}{\delta_e} \quad (4.20)$$

in Eqn. (4.20) δ_e is expressed as;

$$\delta_e = \frac{(P_4 - P_2)L}{AE} \quad (4.21)$$

The normalization of the growth effect using such an axial load range is performed since the growth effect influences the hysteretic curve between the end of Zones 2 and 4 as observed from Fig. 4.10.

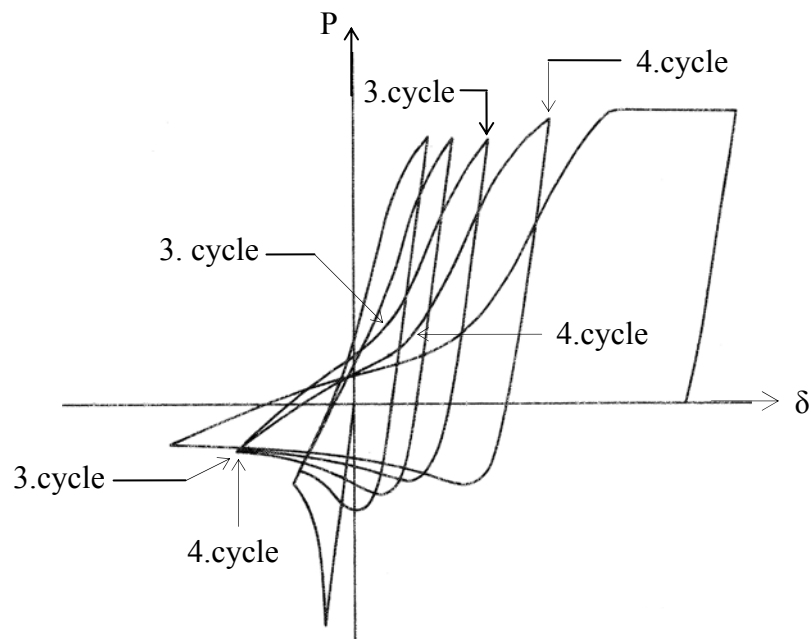


Fig. 4.10 Growth effect between the ends of Zones 2 and 4

The normalized cumulative plastic displacement, D_c , is defined as the cumulative plastic transverse deformation at the end of the compression cycle ($\Delta_2 - \Delta_b$) normalized with respect to the transverse displacement, Δ_b , of the brace at buckling (just before the plastic rotation at the vertex of the brace is initiated) plus the cumulative plastic deformation, δ_p , in tension normalized with respect to yield axial displacement, δ_y . Thus;

$$D_c = \sum_i^n \left(\frac{\Delta_2 - \Delta_b}{\Delta_b} + \frac{\delta_p}{\delta_y} \right) \quad (4.22)$$

In the above equation, Δ_2 is the transverse displacement at the end of the compression cycle (Zone 2) and n is the number of cycles.

The relationships between the growth factor and normalized cumulative plastic displacements are plotted in Fig.4.11, Fig.4.12, and Fig.4.13 for three different brace slenderness ratios of 40, 80 and 120 respectively. Note that the normalizations are performed to obtain a universally applicable relationship between the brace growth and cumulative plastic displacements.

Table 4.1 Properties of steel braces

Brace No	Brace Shape	σ_y (MPa)	P_y (kN)	P_{bu} (kN)	L(mm)	KI/r	e(mm)	Δ_b (mm)
1	W 8×20	278	1114	423	3810	120	12.2	47.3
2	W 6×25	291	1375	1170	1550	40	9.2	2.86
3	W 6×20	277	1050	899	3070	80	2.22	9.3
4	W 6×20	277	1050	894	3070	80	2.35	9.5
5	W 6×20	277	1050	676	3070	80	5.9	27.3
7	W 6×15.5	345	1018	894	1480	40	0.7	0.3
8	2L 6×3 ½ ×3/8	281	1236	877	2830	80	7.5	17
11	2C 8×11.5	245	1061	467	3000	120	1.5	31
13	WT 8×22.5	288	1238	872	3190	80	8.5	19.5
15	Pipe 4×0.237	327	667	489	3070	80	3.5	15.6
18	TS 4×4×0.5	565	2190	1210	2760	80	1.8	36

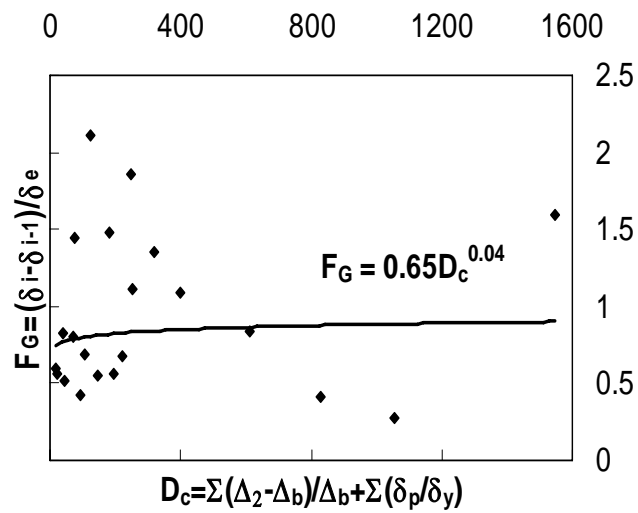


Fig. 4.11 Normalized growth factor versus normalized cumulative displacement relationship for $Kl/r = 40$.

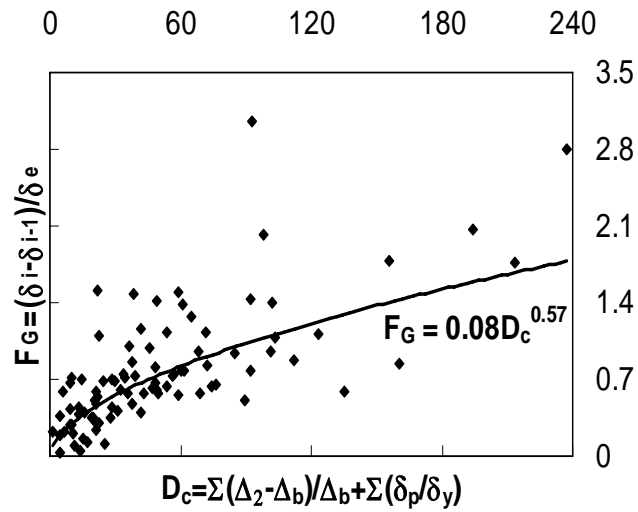


Fig. 4.12 Normalized growth factor versus normalized cumulative displacement relationship for $Kl/r = 80$.

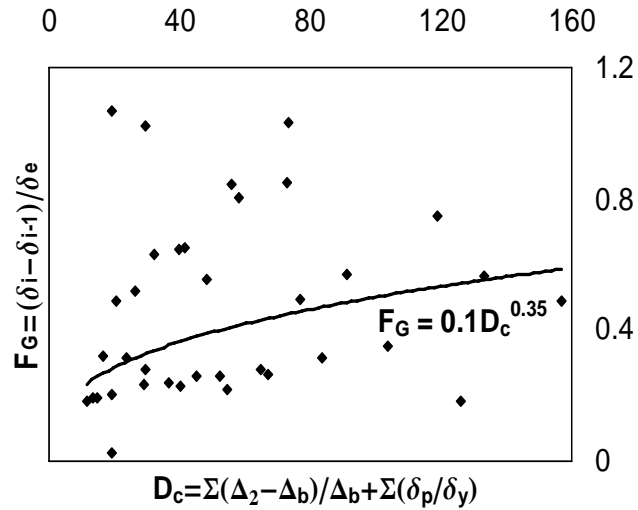


Fig. 4.13 Normalized growth factor versus normalized cumulative displacement relationship for $Kl/r = 120$

A nonlinear logarithmic regression analysis procedure is employed to obtain a relationship between the growth factor, F_G and the normalized cumulative plastic displacement, D_c of the brace. The obtained relationships for three different slenderness ratios are presented below;

For slenderness ratio of 40;

$$F_G = 0.65 D_c^{0.04} \quad (4.23)$$

For slenderness ratio of 80;

$$F_G = 0.08 D_c^{0.57} \quad (4.24)$$

For slenderness ratio of 120;

$$F_G = 0.1D_c^{0.35} \quad (4.25)$$

To obtain a universal relationship between the growth factor and the normalized cumulative plastic displacements of the brace that is applicable at any slenderness ratio (e.g. 75, 96) different than 40, 80 and 120, an analytical relationship between F_G , D_c and KL/r must be formulated. This could be achieved by conducting a two dimensional regression analyses of the available data. However, to decide on the type curve fitting technique, first, the relationship between the growth factor and the slenderness ratio at different normalized cumulative plastic displacement values are plotted in Fig 4.14(a) and (b) for $D_c=10$ and $D_c=100$ respectively. It is observed that the relationship between the growth factor and slenderness ratio at different normalized cumulative plastic displacement values are polynomial but not similar.

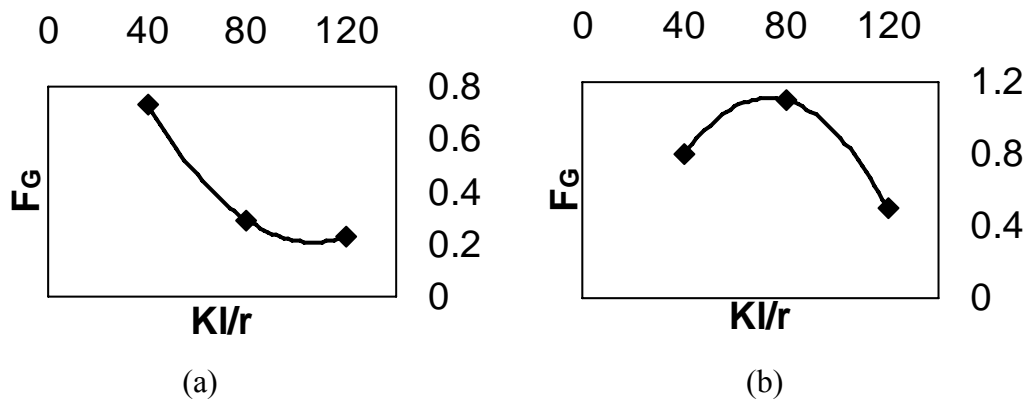


Fig. 4.14 Growth factor effect with different cumulative displacements (a) normalized cumulative displacement is equal to 10 (b) normalized cumulative displacement is equal to 100

Thus an adaptive polynomial curve fitting technique is used to obtain the growth factor as a function of the normalized cumulative plastic displacement and the slenderness ratio. For this purpose, the growth factor is assumed to have the following analytical form;

$$F_G = a + b\left(\frac{Kl}{r}\right) + c\left(\frac{Kl}{r}\right)^2 \quad (4.26)$$

From the above equation and Eqns. (4.23), (4.24) and (4.25), the growth factors at $KL/r= 40, 80,$ and 120 are expressed as follows;

$$a + b(40) + c(40)^2 = 0.67D_c^{0.04} \quad (4.27)$$

$$a + b(80) + c(80)^2 = 0.08D_c^{0.57} \quad (4.28)$$

$$a + b(120) + c(120)^2 = 0.1D_c^{0.35} \quad (4.29)$$

The above equations can be represented in matrix form as follows,

$$\begin{pmatrix} 1 & 40 & 1600 \\ 1 & 80 & 6400 \\ 1 & 120 & 14400 \end{pmatrix} \begin{pmatrix} a \\ b \\ c \end{pmatrix} = \begin{pmatrix} 0.67D_c^{0.04} \\ 0.08D_c^{0.57} \\ 0.1D_c^{0.35} \end{pmatrix} \quad (4.30)$$

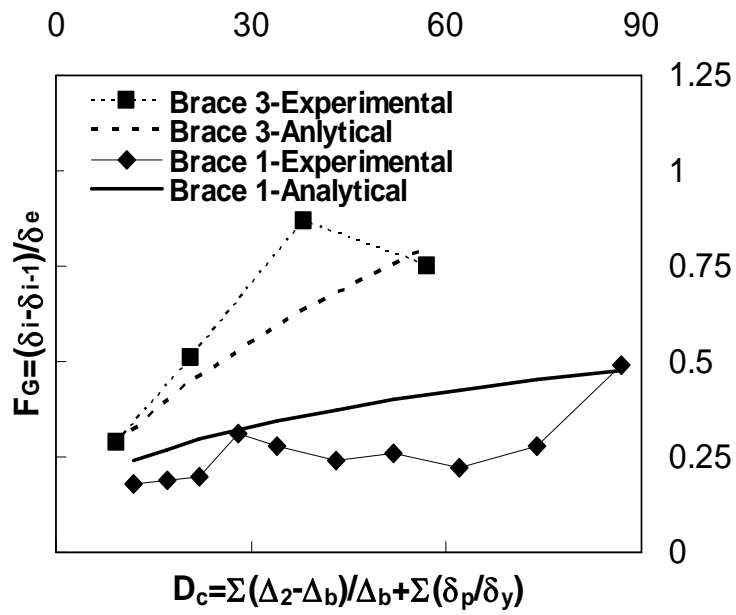
Using Gaussian- Elimination method (Burden and Faires, 2001), the coefficients, a , b and c of the polynomial equation (4.26) are calculated as follows;

$$a = 3 \times 0.67D_c^{0.04} - 3 \times 0.08D_c^{0.57} + 0.1 \times D_c^{0.35} \quad (4.31)$$

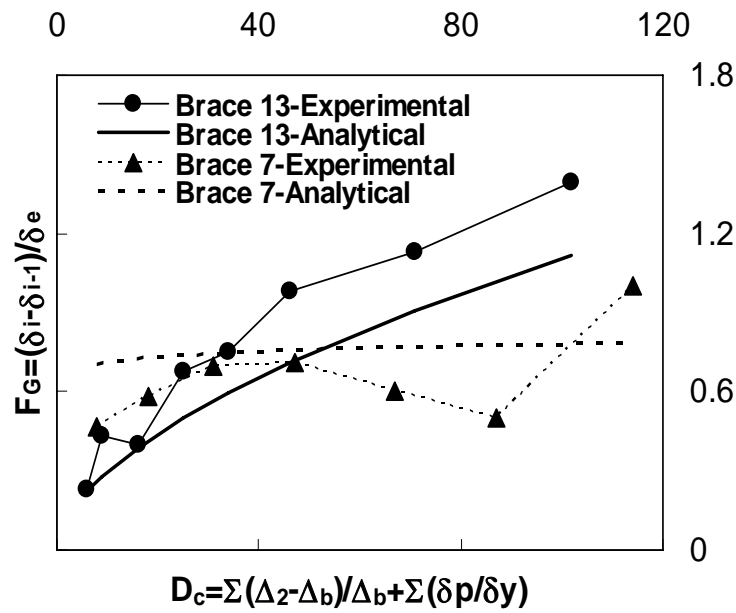
$$b = \frac{4 \times 0.08 D_c^{0.57} - \frac{5}{2} \times 0.67 D_c^{0.04} - \frac{3}{2} \times 0.1 D_c^{0.35}}{40} \quad (4.32)$$

$$c = \frac{0.1 \times D_c^{0.35} - 2 \times 0.08 D_c^{0.57} + 0.67 \times D_c^{0.04}}{3200} \quad (4.33)$$

The experimentally obtained and analytically calculated growth factors are compared in Fig. 4.15 for brace 1 ($KL/r=120$), brace 3 ($KL/r=80$), brace 7 ($KL/r=40$), and brace 13 ($KL/r=80$). It is observed that the growth factor is simulated reasonably well for braces with various slenderness ratios. However, the growth factors for braces with slenderness ratios of 80 and 120 are simulated better than that of the brace with slenderness ratio of 40.



(a)



(b)

Fig. 4.15 Comparison of experimental and analytical brace growth

Note that the coefficients a , b and c are functions of D_c . Thus, Eqn. (4.26) gives an exact match to Eqns. (4.23), (4.24) and (4.25) at slenderness ratios of 40, 80 and 120 respectively. Using Eqn.(4.26), the relationships between the growth factor F_G and the normalized cumulative plastic displacement D_c are presented in Fig. (4.16) for different slenderness ratios. It is observed that the growth effect is more pronounced at intermediate slenderness ratios.

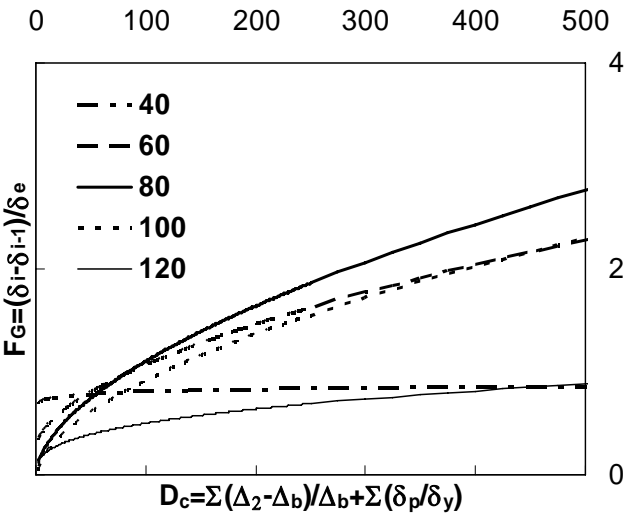


Fig. 4.16 F_G - D_c relations for different slenderness ratios

4.2.4 Zone 3

Zone 3 is associated with the elastic unloading of the brace. The deformed shape of the brace in this unloading stage due to bending effect is demonstrated in Fig. 4.17. The dashed line shows the deformed shape of the brace at the end of Zone 2, whereas the solid line shows the deformed shape of the brace when the compressive axial load is dropped to a lower magnitude upon unloading.

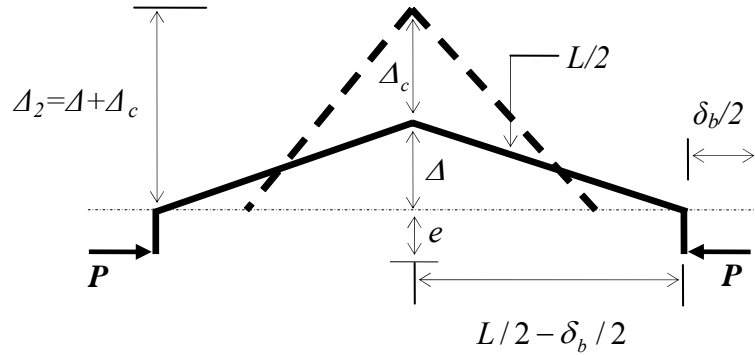


Fig. 4.17 Deformed brace shape in Zone-3 due to the bending effect

From the geometry of Fig.4.17, the transverse displacement, Δ , of the brace at any axial load level, P , is expressed as;

$$\Delta = \Delta_2 - \Delta_c \quad (4.34)$$

As mentioned earlier, in the above equation, Δ_2 is the transverse displacement at the end of Zone 2 where the unloading starts and Δ_c is the change in the transverse displacement due to the effect of unloading. The change in the transverse displacement can be calculated using the unit dummy load method (Popov,1999)

$$\Delta_c = 2 \int_0^{L/2} \frac{Mm}{EI} dx \quad (4.35)$$

To satisfy the static equilibrium of the free body diagram of the already buckled brace given in Fig. 4.17, the following expression must be satisfied

$$M = \left[e + \frac{2(\Delta_2 - \Delta_c)}{L} x \right] P_c \quad (4.36)$$

Where P_c is the change in the axial load level with reference to the axial load, P_2 , at the end of Zone 2 and is expressed as,

$$P_c = P - P_2 \tag{4.37}$$

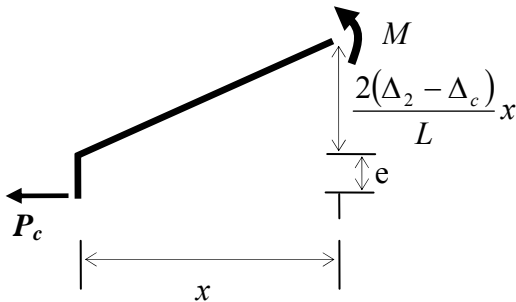


Fig. 4.18 Free Body Diagram for M

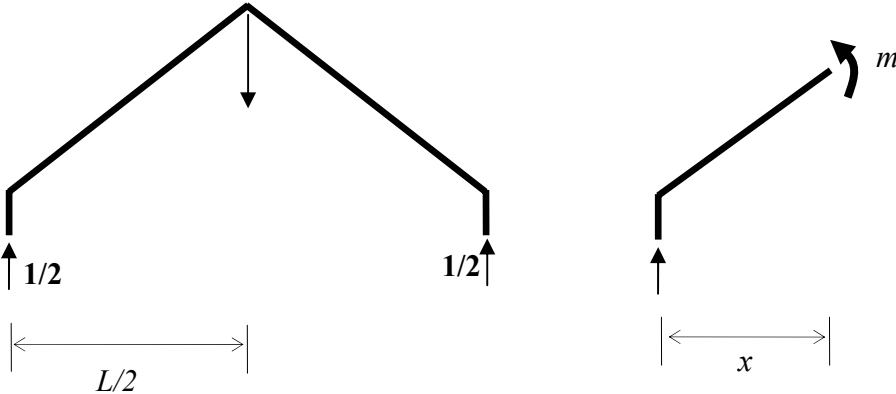


Fig. 4.19 Unit dummy load at center

From Fig.4.19, the unit dummy load moment due to a unit load applied at the vertex of the brace is expressed as;

$$m = \frac{x}{2} \quad (4.38)$$

Substituting Eqns. (4.36) and (4.38) into Eqn. (4.35), Δ_c is expressed as:

$$\Delta_c = \frac{2}{EI} \int_0^{L/2} \left[e + \frac{2(\Delta_2 - \Delta_c)}{L} x \right] P_c \frac{x}{2} dx \quad (4.39)$$

Integrating the above equation, Δ_c is obtained as;

$$\Delta_c = \frac{1.5e + \Delta_2}{\frac{12EI}{P_c L^2} + 1} \quad (4.40)$$

Substituting Eqn.(4.37) into Eqn.(4.40) Δ_c is obtained as a function of the known hysteresis parameters as follows;

$$\Delta_c = \frac{1.5e + \Delta_2}{\frac{12EI}{(P - P_2)L^2} + 1} \quad (4.41)$$

Next, substituting Eqn. (4.41) into Eqn. (4.34), the transverse displacement Δ , is expressed as;

$$\Delta = \Delta_2 - \frac{1.5e + \Delta_2}{\frac{12EI}{(P - P_2)L^2} + 1} \quad (4.42)$$

Substituting Eqn. (4.42) into Eqn. (4.14), the axial displacement, δ of the brace is obtained as follows;

$$\delta = \frac{PL}{AE} - L + \sqrt{L^2 - 4 \left[\Delta_2 - \frac{1.5e + \Delta_2}{\frac{12EI}{(P - P_2)L^2} + 1} \right]^2} \quad (4.43)$$

Zone 3 is affected by the brace growth effect. Thus, this effect must be included in Eqn. (4.43). To distribute the growth effect between the ends of Zones 2 and 4, proportional to the level of axial load, the growth factor, F_G is first multiplied by the elastic displacement δ_e , at any axial load range $P - P_2$ and then added to Eqn. (4.43). Accordingly the axial displacement versus force relationship for Zone 3 including the growth effect is defined as follows;

$$\delta = \frac{PL}{AE} - L + \sqrt{L^2 - 4 \left[\Delta_2 - \frac{1.5e + \Delta_2}{\frac{12EI}{(P - P_2)L^2} + 1} \right]^2} + F_G \left[\frac{(P - P_2)L}{AE} \right] \quad (4.44)$$

Note that Zone-3 ends when the second order moment due to the axial force is equal to the reduced plastic moment capacity, M_{pr} , of the brace. The following relationship can be used to determine the level of axial load, P_3 at which Zone 3 ends;

$$(\Delta + e)P_3 = M_{pr} \quad (4.45)$$

4.2.5 Zone 4

In this zone, unlike Zone 3, the behavior of the brace is plastic. That is, the product of the axial load and transverse displacement again becomes equal to the plastic moment capacity of the brace under the applied axial load. The deformed shape of

the brace in this reversed loading stage due to bending effect is demonstrated in Fig. (4.20)

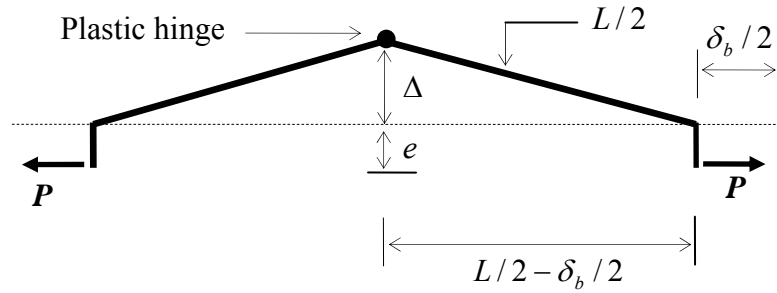


Fig. 4.20 Deformed brace shape in zone 4 due to bending effect

To satisfy static moment equilibrium at the mid-length of the brace within Zone 4, the following relationship must be satisfied;

$$(\Delta + e)P = M_{pr} \quad (4.46)$$

Solving Δ from the above equation

$$\Delta = \frac{M_{pr}}{P} - e \quad (4.47)$$

Note that when the axial force is equal to the yield force, P_y , the reduced plastic moment capacity of the brace must become zero due to the moment-axial force interaction relationship. Thus, the second order moment must be equal to zero to satisfy the state of static equilibrium presented analytically in Eqn. (4.46) when $P=P_y$. However, the presence of the initial eccentricity, e , makes this impossible.

For this reason, e must be multiplied by a factor that makes it gradually approach to zero at the yield axial load level of the brace. Accordingly Eqn (4.47) is modified to satisfy static equilibrium at the yield axial load level as follows;

$$\Delta = \frac{M_{pr}}{P} - e \left(\frac{P_y - P}{P_y - P_4} \right) \quad (4.48)$$

Substituting Eqn. (4.48) into Eqn. (4.14) with the growth effect, the following expression is obtained that defines the axial force-displacement relationship of the brace within Zone 4;

$$\delta = \frac{PL}{AE} - L + \sqrt{L^2 - 4 \left[\frac{M_{pr}}{P} - e \left(\frac{P_y - P}{P_y - P_4} \right) \right]^2} + F_G \left[\frac{(P - P_2)L}{AE} \right] \quad (4.49)$$

The analytical results obtained for Zones 1, 2, 3 and 4 are compared with the experimental results of Black et al. (1980) for braces 3 and 11 in Figs. 4.21 and 4.22 respectively. In the figures, axial force versus axial displacement as well as axial force versus transverse displacement relationships of the analytical and experimental results are compared. Although for Zones 1 and 2 the analytical and experimental results for the first loading cycles are compared, for Zones 3 and 4, the analytical and experimental results are compared for loading cycles 3 and 8 of Brace 3 and 11 respectively. As observed from the figures a fairly good agreement is found between the analytical and experimental results. It is to be noted that the sharp transition from Zone 3 to Zone 4 in the analytical plots results from the elasto-perfectly plastic moment curvature relationships used in the development of the equations. It is anticipated that this will not have a significant affect on the magnitude of the hysteretic energy dissipated per cycle. However, such a simplification facilitates the derivation of the analytical equations for each zone and makes the proposed hysteretic model easily applicable in practice.

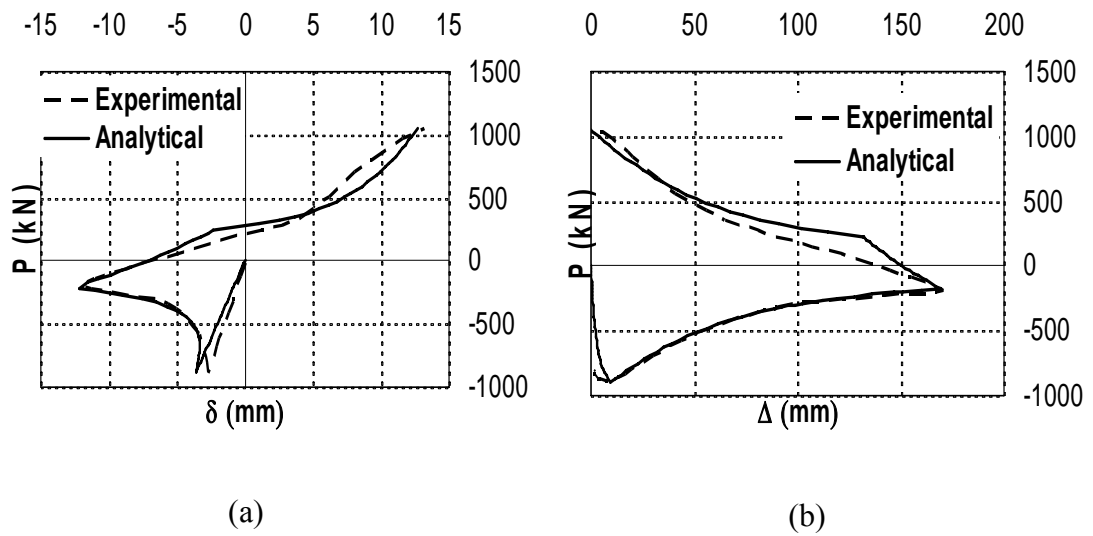


Fig. 4.21 Comparison of experimental and analytical results for Brace 3, Zones 1, 2, 3, and 4; (a) axial force versus axial displacement, (b) axial force versus transverse displacement

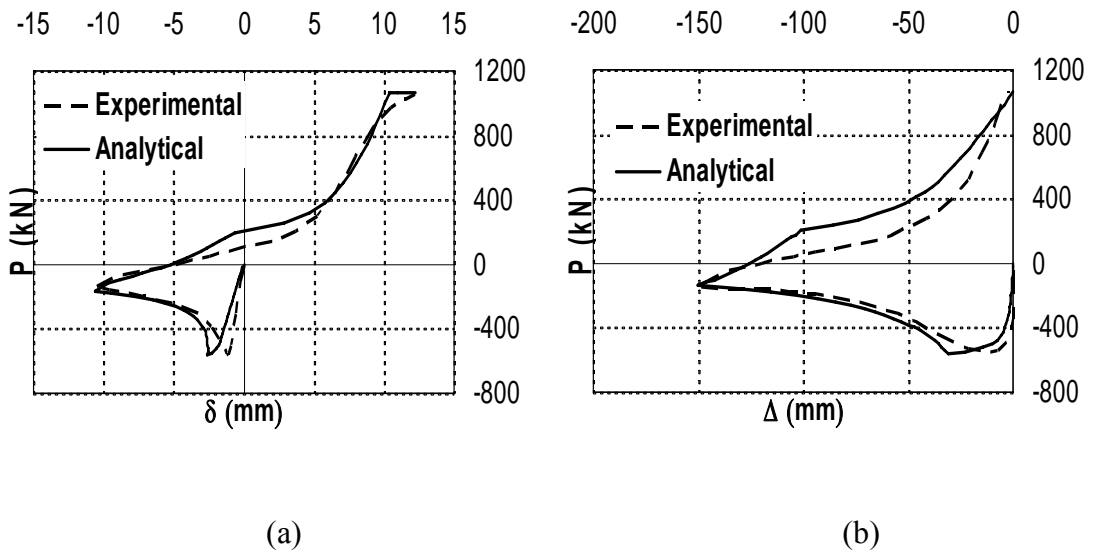


Fig. 4.22 Comparison of experimental and analytical results for Brace 11, Zones 1, 2, 3, and 4; (a) axial force versus axial displacement, (b) axial force versus transverse displacement

4.2.6 Zone 5

In Zone 5, the brace is unloaded elastically. Within this zone, the transverse deflection of the brace decreases to such an extent that the elastic deflections become relatively significant in relation to the plastic deflections. Consequently, the deformed shape of the brace becomes as shown in Fig.4.23. This deformed shape needs to be considered in the derivation of the equations to simulate the elastic unloading of the brace within this zone. The deformed shape of the brace consists of a plastic and an elastic part as shown in Fig.4.23

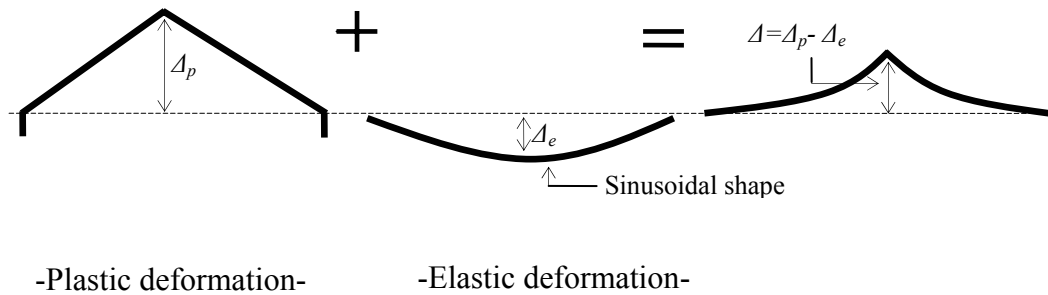


Fig. 4.23 Superposition of plastic and elastic parts for the deformed shape in zone 5

From Fig. 4.23, the maximum transverse deflection Δ is expressed as;

$$\Delta = \Delta_p - \Delta_e \quad (4.50)$$

Based on the above equation, the maximum transverse deflection, Δ_4 , of the brace at the end of Zone 4 is expressed as;

$$\Delta_4 = \Delta_{p4} - \Delta_{e4} \quad (4.51)$$

where, Δ_{p4} and Δ_{e4} are respectively, the maximum plastic and elastic transverse displacements at the end of Zone 4. Using unit dummy load method, the elastic transverse displacement is expressed as,

$$\Delta_{e4} = 2 \int_0^{L/2} \frac{Mm}{EI} dx \quad (4.52)$$

where,

$$M = M_{p4} - M_{e4} \quad (4.53)$$

In the above equation, M_{p4} and M_{e4} are the second order moments due to the plastic and elastic parts of the transverse deflections respectively.

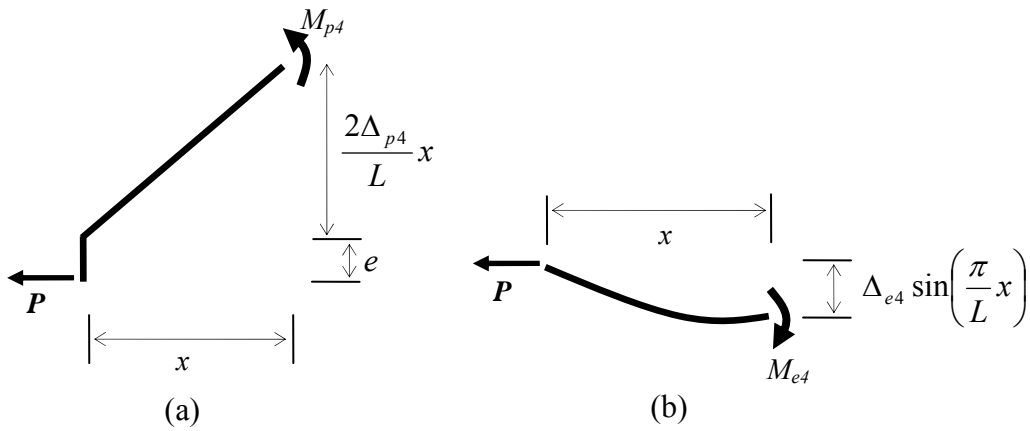


Fig. 4.24 Plastic and elastic second order moments

From Fig. 4.24, these second order moments, $M_{\Delta p4}$ and $M_{\Delta e4}$, are formulated as follows;

$$M_{p4} = \left[e + \frac{2\Delta_{p4}}{L} x \right] P_4 \quad (4.54)$$

$$M_{e4} = \left[\Delta_{e4} \sin\left(\frac{\pi}{L} x\right) \right] P_4 \quad (4.55)$$

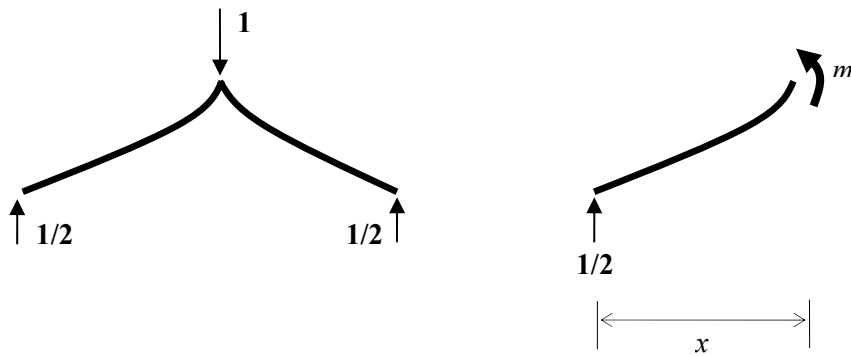


Fig. 4.25 Unit dummy load at center

From Fig.4.25, the moment due to the unit dummy load is expressed as;

$$m = \frac{x}{2} \quad (4.56)$$

Solving for Δ_{p4} from Eqn. (4.51) and substituting in Eqn. (4.54), M_{p4} is expressed as;

$$M_{p4} = \left[e + \frac{2(\Delta_{e4} + \Delta_4)}{L} x \right] P_4 \quad (4.57)$$

Substituting Eqns. (4.55) and (4.57) into Eqn. (4.53), the total second order moment due to the effect of the axial loading is expressed as;

$$M = \left[e + \frac{2(\Delta_{e4} + \Delta_4)}{L} x - \Delta_{e4} \sin\left(\frac{\pi}{L} x\right) \right] P_4 \quad (4.58)$$

Next, substituting Eqns. (4.56) and (4.58) into Eqn. (4.52), the elastic part of the transverse displacement is calculated as follows;

$$\Delta_{e4} = \frac{P_4 \left\{ -\frac{L^2 \Delta_e}{\pi^2} + \frac{L^2}{24} [3e + 2(\Delta_{e4} + \Delta_4)] \right\}}{EI} \quad (4.59)$$

In the expression above, Δ_{e4} is at both sides of the equation. Thus, solving for Δ_{e4} , the following equation is obtained for the elastic part of the transverse displacement;

$$\Delta_{e4} = \frac{\pi^2 L^2 P_4 (3e + 2\Delta_4)}{2L^2 P_4 (12 - \pi^2) + 24\pi^2 EI} \quad (4.60)$$

Next, substituting Eqn. (4.60) into Eqn. (4.51), the transverse displacement of the brace is expressed as follow;

$$\Delta_4 = \Delta_{p4} - \frac{\pi^2 L^2 P_4 (3e + 2\Delta_4)}{2L^2 P_4 (12 - \pi^2) + 24\pi^2 EI} \quad (4.61)$$

From the above equation, the plastic part of the transverse displacement Δ_{p4} is obtained as;

$$\Delta_{p4} = \Delta_4 + \frac{\pi^2 L^2 P_4 (3e + 2\Delta_4)}{2L^2 P_4 (12 - \pi^2) + 24\pi^2 EI} \quad (4.62)$$

It is to be noted that in Zone 5, the plastic part of the transverse displacement has a constant value. Consequently, the plastic transverse displacement, Δ_{p4} , at the end of

the Zone 4 is equal to the plastic transverse displacement at any applied axial load level within Zone 5. That is,

$$\Delta_p = \Delta_{p4} \quad (4.63)$$

Substituting the above equation into Eqn. (4.62), the following expression is obtained for the plastic part of the transverse displacement within Zone 5;

$$\Delta_p = \Delta_4 + \frac{\pi^2 L^2 P_4 (3e + 2\Delta_4)}{2L^2 P_4 (12 - \pi^2) + 24\pi^2 EI} \quad (4.64)$$

Then, from Eqn. (4.60), the elastic part of the transverse displacement, Δ_e , at any axial load level is obtained as;

$$\Delta_e = \frac{\pi^2 L^2 P (3e + 2\Delta_4)}{2L^2 P (12 - \pi^2) + 24\pi^2 EI} \quad (4.65)$$

Now, substituting Eqns. (4.64) and (4.65) into Eqn. (4.50), the transverse displacement of the brace is obtained as follows;

$$\Delta = \Delta_4 + \left[\frac{P_4}{2L^2 P_4 (12 - \pi^2) + 24\pi^2 EI} - \frac{P}{2L^2 P (12 - \pi^2) + 24\pi^2 EI} \right] \pi^2 L^2 (3e + 2\Delta_4) \quad (4.66)$$

Finally, substituting the above equation into Eqn.(4.14), the axial load-displacement relationship of the brace within Zone 5 is expressed as;

$$\delta = \frac{PL}{AE} - L + \sqrt{L^2 - 4 \left\{ \Delta_4 + \left[\frac{P_4}{2L^2 P_4 (12 - \pi^2) + 24\pi^2 EI} - \frac{P}{2L^2 P (12 - \pi^2) + 24\pi^2 EI} \right] \pi^2 L^2 (3e + 2\Delta_4) \right\}^2} \quad (4.67)$$

4.2.7 Zone 6

Within this zone, the axial compressive load is gradually increased from zero to a level where buckling is initiated again. In this zone, the buckling load capacity is less than the initial buckling load capacity defined in Zone 1. The degradation of the buckling load capacity is caused by the Baushinger effect as well as the residual transverse displacement of the brace resulting from the plastic hinge rotations during the previous cycles. Baushinger effect degrades the initial elasticity modulus, E to a smaller value E_t with increasing number of cycles. Therefore, in the derivation of the analytical equations to simulate the axial force-deformation relationship within this zone, the effect of the residual transverse displacement at the end of Zone 5 and the Bauschinger effect in terms of a reduced modulus of elasticity (E_t , tangent modulus) must be included.

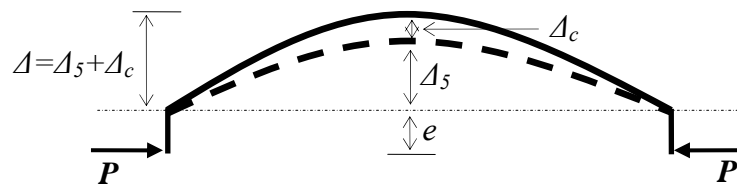


Fig. 4.26 Deformed brace shape in zone 6 due to bending effect

From Fig.4.26, the transverse displacement Δ is expressed as;

$$\Delta = \Delta_5 + \Delta_c \quad (4.68)$$

Where Δ_5 is the residual transverse displacement at the end of Zone 5 and Δ_c is the change in the transverse displacement of the brace due to the effect of reloading starting at the end of Zone 5. The change in the transverse displacement can be calculated using the unit dummy load method (Popov, 1999) as follows;

$$\Delta_c = 2 \int_0^{L/2} \frac{Mm}{E_t I} dx \quad (4.69)$$

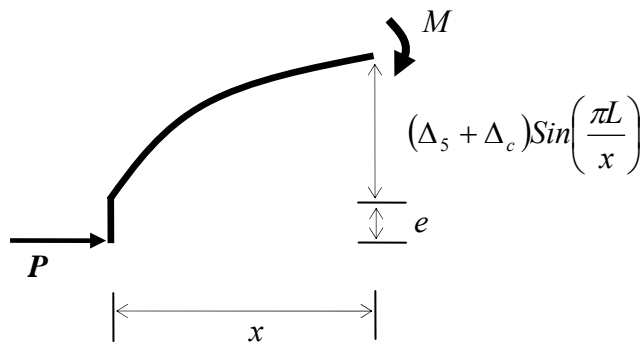


Fig. 4.27 Free body diagram for M

From Fig.4.27, the second order moment, M , is expressed as;

$$M = P \left[e + (\Delta_5 + \Delta_c) \sin\left(\frac{\pi L}{x}\right) \right] \quad (4.70)$$

From Fig. 4.20, the moment expression due to the unit dummy load is obtained as;

$$m = \frac{x}{2} \quad (4.71)$$

Now, substituting Eqns. (4.70) and (4.71) into Eqn.(4.69), Δ_c is obtained as follows;

$$\Delta_c = \frac{1.5e + \frac{8}{\pi^2} \Delta_5}{\frac{12E_t I}{PL^2} + 1} \quad (4.72)$$

Next, substituting the above equation into Eqn.(4.68), the transverse displacement, Δ , is calculated as;

$$\Delta = \Delta_5 + \frac{1.5e + \frac{8}{\pi^2} \Delta_5}{\frac{12E_t I}{PL^2} + 1} \quad (4.73)$$

Finally, substituting the above equation into Eqn.(4.14), the axial load-displacement relationship of the brace within Zone 6 is expressed as

$$\delta = \frac{PL}{AE} - L + \sqrt{L^2 - 4 \left(\Delta_5 + \frac{1.5e + \frac{8}{\pi^2} \Delta_5}{\frac{12E_t I}{PL^2} + 1} \right)^2} \quad (4.74)$$

4.2.7.1 Formulation of the Tangent Modulus

As observed from Fig.(2.3), the Bauschinger effect produces a degradation of the modulus of elasticity within the positive strain-negative stress and the negative strain-positive stress regions of the stress strain relationship of steel. It is also a known fact that the degradation in the elastic modulus is a function of the previous number of axial displacement cycles. Since, buckling load of a brace is a function of the tangent modulus of the material, smaller buckling loads are generally obtained at subsequent cycles of compression loading of the brace. This effect needs to be included in the analytical equations derived for Zone 6. This requires obtaining an expression for the elastic tangent modulus, E_t as a function of the number of cycles.

Accordingly, in this study, it is assumed that the degradation of the elastic modulus depends on the normalized cumulative plastic displacement of the brace as in the case of the growth effect. Using the experimental data of Black et al. (1980), the buckling load P_b at the subsequent cycles following the first cycle of the P - δ curves is obtained as a function of D_c . It is noteworthy that as explained earlier the reduction in the buckling capacity of a brace is a function of both the residual transverse displacement of the brace and the tangent modulus. Thus, the cycles that include the residual transverse displacement effect is excluded from the data used for obtaining the tangent modulus as a function of the normalized cumulative plastic displacement of the brace. To obtain a relationship between the tangent modulus E_t and cumulative displacement D_c the following steps are employed.

First, from the experimental P - δ hysteretic curves of the braces tested by Black et al. (1980), experimental buckling loads, P_b , at subsequent loading cycles following the first cycle are obtained. Then, these buckling loads are substituted in Eqn. (4.18) to calculate the transverse displacement at buckling. Following this, Eq. 4.15 is rearranged to obtain the tangent modulus of elasticity as a function of the, buckling load, the transverse displacement at buckling and the properties of the brace as follows;

$$E_t = -\frac{L^2 P_b \left(e + \frac{8}{\pi^2} \Delta_b \right)}{8I\Delta_b} \quad (4.75)$$

Next, the buckling load, P_b obtained from the experimental data of Black et al. (1980), the transverse displacement at buckling, Δ_b , the moment of inertia and length of the brace are substituted in Eqn.(4.75) to calculate the elastic tangent modulus, E_t for each load cycle of the axial force-displacement hysteresis of the brace. Next, the ratio, $F_B=E_t/E$ of the tangent modulus to the elastic modulus is calculated and plotted as a function of the normalized cumulative plastic displacement, D_c , for all the braces from the tests of Black et al. (1980) considered

in this study. The $F_B = E_t/E$ versus D_c plots for slenderness ratios of 40, 80, and 120 are shown in Figs. 4.29, 4.30 and 4.31.

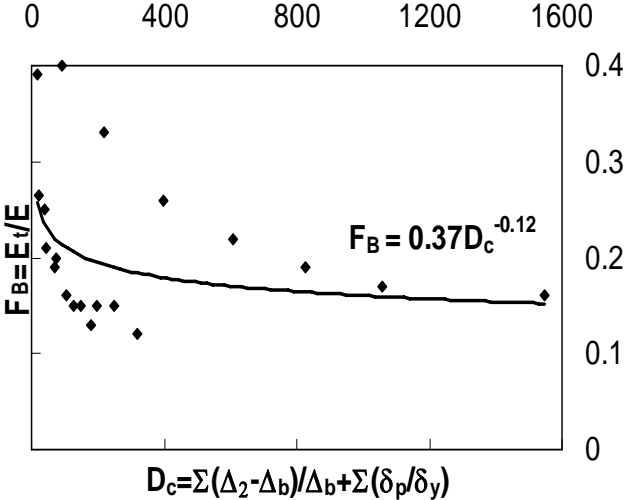


Fig. 4.28 Tangent elasticity versus cumulative displacement ($Kl/r = 40$)

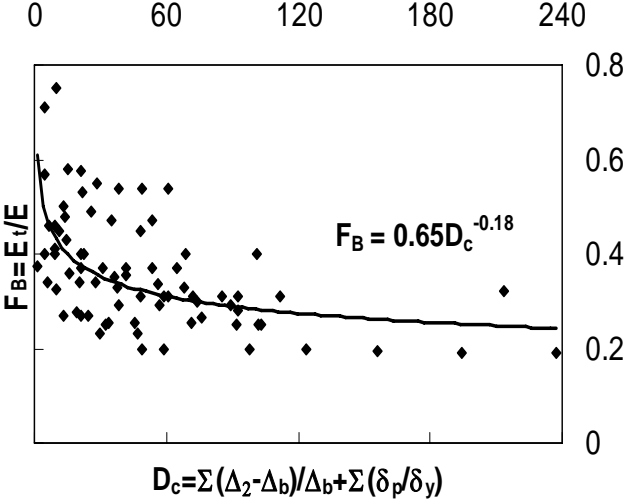


Fig. 4.29 Tangent elasticity versus cumulative displacement ($Kl/r = 80$)

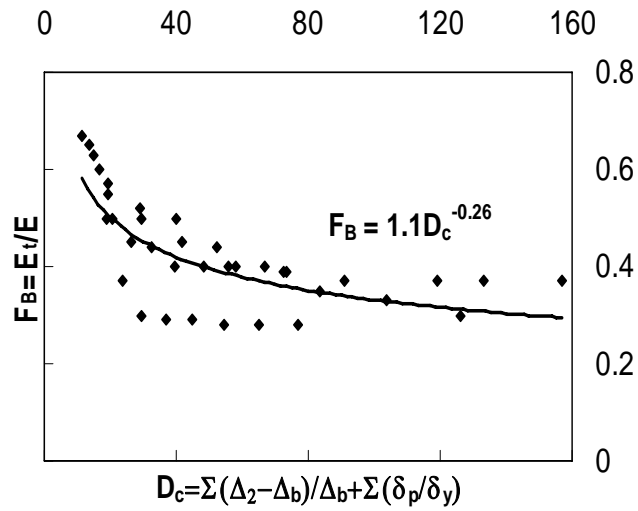


Fig. 4.30 Tangent elasticity versus cumulative displacement ($Kl/r = 120$)

A nonlinear logarithmic regression analysis procedure is employed to obtain a relationship between $F_B = E_t/E$ and D_c of the braces. The obtained relationships for three different slenderness ratios are presented below;

For slenderness ratio of 40;

$$F_B = 0.37D_c^{-0.12} \quad (4.76)$$

For slenderness ratio of 80;

$$F_B = 0.65D_c^{-0.18} \quad (4.77)$$

For slenderness ratio of 120;

$$F_B = 1.1D_c^{-0.26} \quad (4.78)$$

To obtain a universal relationship between F_B and the normalized cumulative plastic displacements of the brace that is applicable at any slenderness ratio different than 40, 80 and 120, an analytical relationship between F_B , D_c and KL/r must be formulated. For this purpose an adaptive polynomial curve fitting technique is used to obtain $F_B=E_t/E$ ratio as a function of the normalized cumulative plastic displacement and the slenderness ratio. Accordingly the $F_B=E_t/E$ ratio is assumed to have the following analytical form;

$$F_B = a + b\left(\frac{KL}{r}\right) + c\left(\frac{KL}{r}\right)^2 \quad (4.79)$$

From the above equation and Eqns. (4.76), (4.77) and (4.78), the $F_B=E_t/E$ ratio at $KL/r= 40, 80,$ and 120 are expressed as follows;

$$a + b(40) + c(40)^2 = 0.37(D_c)^{-0.12} \quad (4.80)$$

$$a + b(80) + c(80)^2 = 0.65(D_c)^{-0.18} \quad (4.81)$$

$$a + b(120) + c(120)^2 = 1.1(D_c)^{-0.26} \quad (4.82)$$

The above equations can be represented in matrix form as follows,

$$\begin{pmatrix} 1 & 40 & 1600 \\ 1 & 80 & 6400 \\ 1 & 120 & 14400 \end{pmatrix} \begin{pmatrix} a \\ b \\ c \end{pmatrix} = \begin{pmatrix} 0.37D_c^{-0.12} \\ 0.65D_c^{-0.18} \\ 1.1D_c^{-0.26} \end{pmatrix} \quad (4.83)$$

Using Gaussian- Elimination method (Burden and Faires, 2001), the coefficients, a , b and c of the polynomial Eqn. (4.26) are calculated as follows;

$$a = 3 \times 0.37 D_c^{-0.12} - 3 \times 0.65 D_c^{-0.18} + 1.1 \times D_c^{-0.26} \quad (4.84)$$

$$b = \frac{4 \times 0.65 D_c^{-0.18} - \frac{5}{2} \times 0.37 D_c^{-0.12} - \frac{3}{2} \times 1.1 D_c^{-0.26}}{40} \quad (4.85)$$

$$c = \frac{1.1 \times D_c^{-0.26} - 2 \times 0.65 D_c^{-0.18} + 0.37 \times D_c^{-0.12}}{3200} \quad (4.86)$$

Note that the coefficients a , b and c are functions of D_c . Thus, Eqn. (4.79) gives an exact match to Eqns. (4.76), (4.77) and (4.78) at slenderness ratios of 40, 80 and 120 respectively. Substituting Eqn. (4.79) into Eqn. (4.75) and solving for P_b , the analytical buckling load is obtained as follows;

$$P_b = - \frac{8 \Delta_b E \left(a + b \left(\frac{KL}{r} \right) + c \left(\frac{KL}{r} \right)^2 \right) I}{L^2 \left(e + \frac{8}{\pi^2} \Delta_b \right)} \quad (4.87)$$

The ratio of the experimental buckling load to the analytical buckling load calculated using the above equation is plotted as a function of the cycle number in Fig. 4.31 for various braces taken from the tests of Black et al. (1980). It is observed that most of the data has a small dispersion around 1.0. This indicates a reasonably good agreement between the analytical and experimental buckling load. This also validates the accuracy of the $F_B = E_t/E$ ratio formulated above. Furthermore, using Eqn.(4.79), the relationships between the $F_B = E_t/E$ ratio and the normalized cumulative plastic displacement D_c are presented in Fig. (4.32) for different slenderness ratios. From the figure, a larger reduction of the elastic tangent modulus is observed at smaller D_c and KL/r ratios and at larger D_c and KL/r ratios.

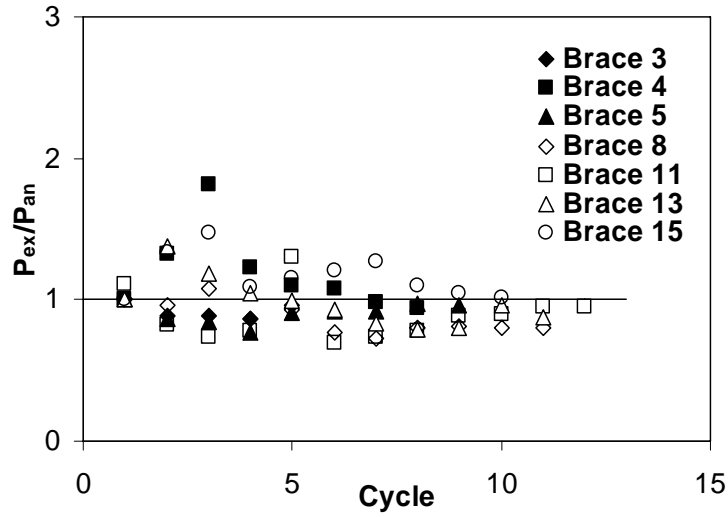


Fig. 4.31 Experimental and analytical buckling load ratios

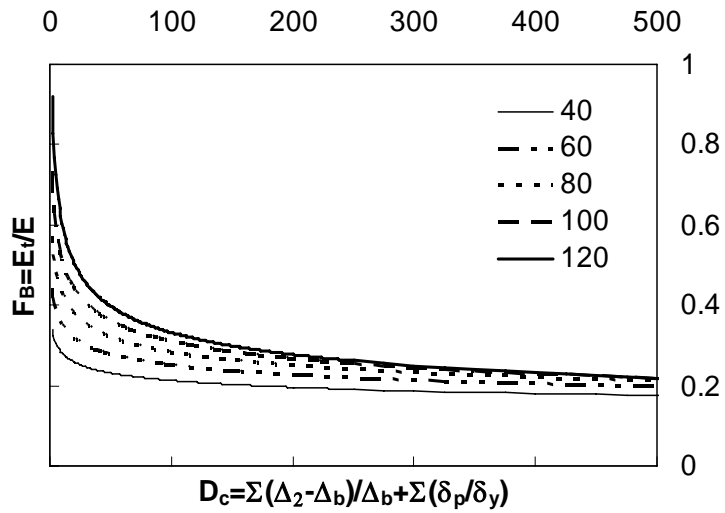


Fig. 4.32 E_t/E versus cumulative displacement

The analytical results obtained for Zones 1, 2, 3, 4, 5, and 6 are compared with the experimental results of Black et al. (1980) for brace 3 and brace 11 in Fig. (4.33) and Fig.(4.34) respectively. Both axial force-axial displacement and axial force-

transverse displacement relationships are compared. Although for Zones 1 and 2 the analytical and experimental results for the first loading cycles are compared, for the subsequent zones (3, 4, 5, 6) the analytical and experimental results are compared for loading cycles 3 and 8 of Brace 3 and 11 respectively. A fairly good agreement is found between the experimental and analytical results. It is also observed that the degradation of the buckling capacity is simulated quite well by the developed analytical hysteretic model.

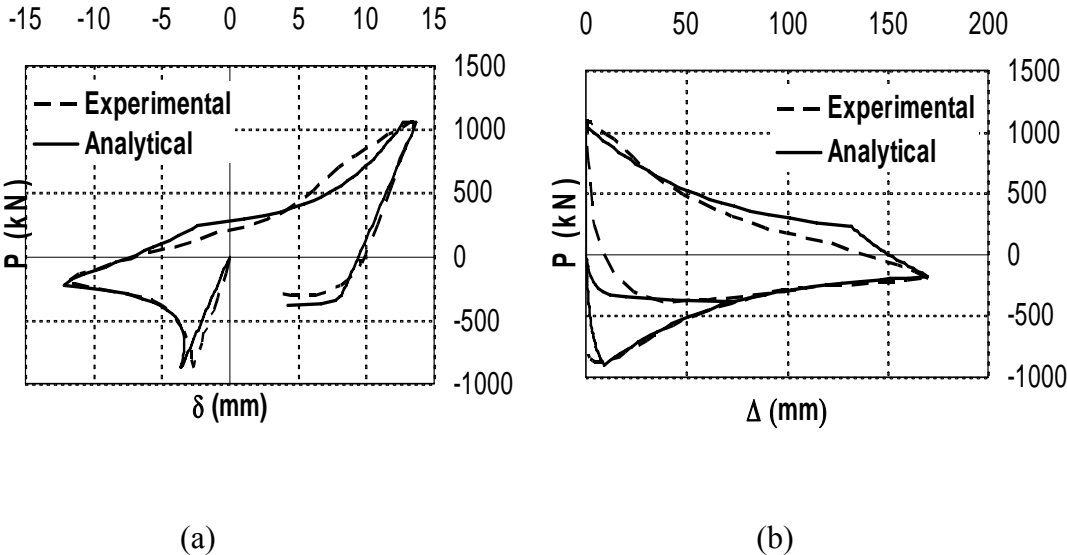


Fig. 4.33 Comparison of experimental and analytical results for Brace 3, Zones 1, 2, 3, 4, 5, and 6; (a) axial force versus axial displacement, (b) axial force versus transverse displacement

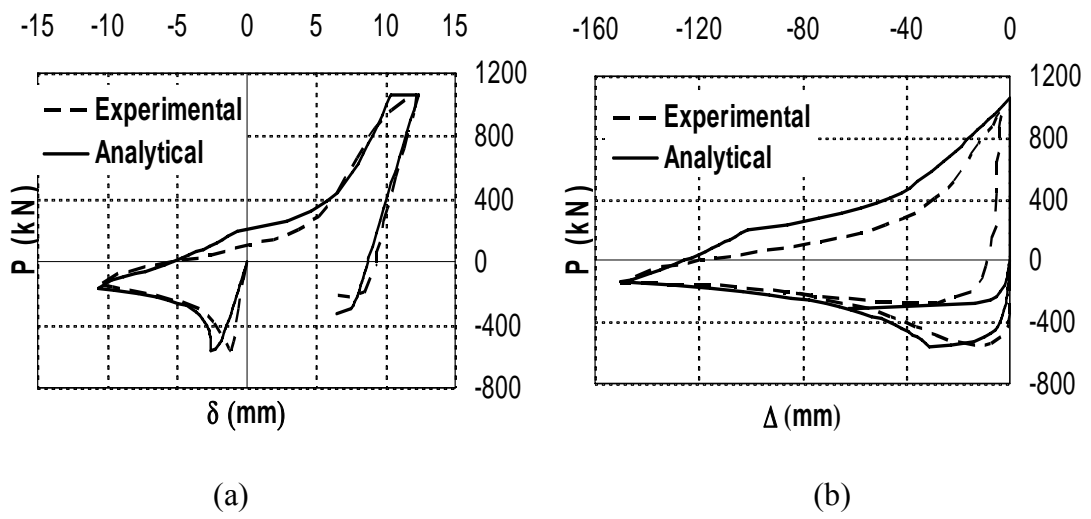


Fig. 4.34 Comparison of experimental and analytical results for Brace 11, Zones 1, 2, 3, 4, 5, and 6; (a) axial force versus axial displacement, (b) axial force versus transverse displacement

CHAPTER 5

COMPARISON OF ANALYTICAL AND EXPERIMENTAL RESULTS

In this chapter, the developed analytical hysteretic model is verified using the experimental cyclic axial force – axial deformation and axial force – transverse deformation relationships of the braces tested by Black et al. (1980). Furthermore, in order to observe its capabilities compared to other existing models, the analytical model developed in this study is compared with the refined physical theory models of Ikeda and Mahin (1984) and Jin and El-Tawil (2003) as well as with the phenomenological model of Ikeda et al. (1984).

5.1 Selection of the Braces for Verification Purposes

Eleven braces were selected from the specimens used by Black et al. (1980) to verify the developed analytical model. Since the effective slenderness ratio has been shown to be one of the most important parameters affecting the hysteretic behavior of braces, the eleven braces were selected to have three different slenderness ratios of 40, 80 and 120. Included within the eleven selected braces were six different cross-sectional shapes: W, T, pipe, box, double channel, and double angle. A common slenderness ratio of 80 was used for specimens with different section types to allow for a direct comparison of the results due to the variation in the section type of the brace. On the basis of its common use in steel braced frame construction, the W section was chosen as a basic shape for the comparison of the analytical results

with the experimental ones. Therefore, six out of the eleven specimens are chosen to have W sections. Three of the W sections were W 6×20's with a commonly used slenderness ratio of $KL/r = 80$. Three additional W sections with the following sizes and slenderness ratios were selected; (i) W 8×20, $KL/r=120$, (ii) W6×15.5, $KL/r=40$ and (iii) W6×25, $KL/r=40$. The other brace sections were; (i) Double-channel, 2C 8×11.5, $KL/r=120$, (ii) Double-angle 2L 6×3 ½ ×3/8, $KL/r = 80$, (iii) T, WT 8×22.5, $KL/r=80$, (iv) Pipe, 4×0.237, $KL/r=80$ and (v) Box, TS 4×0.5, $KL/r=80$.

5.2 Experimental Displacement Histories Applied on the Braces

All the test specimens were subjected to quasi-statically applied cycles of reversed axial displacements. These cycles generally resulted in compressive loads causing inelastic buckling followed by tensile loads sufficient to cause yielding in the brace. Since loading cycles were continued until the axial strength of the specimen was exhausted, some braces experienced more cycles than others. Load histories of the eleven braces used in this study for verification purposes are presented in Fig. 5.1

5.3 Comparison of Analytical and Experimental Results

5.3.1 Comparison of Hysteresis Loops

In this section the analytical axial force-axial displacement and axial force-transverse displacement hysteresis of the eleven braces are compared with their experimental counterparts. The results are presented in Figs. 5.2 – 5.12.

Fig. 5.2 displays the analytical and experimental hysteresis loops of Brace 1. As mentioned earlier, this brace is made of a W 8×20 section and has a slenderness ratio of 120. As observed from the plots of Fig. 5.2, the analytical hysteresis loops closely match their experimental counterparts. Fig 5.3 displays the analytical and

experimental hysteresis loops of a similar brace with a section size of W 6x25 but with a slenderness ratio of 40 (Brace 2). As observed from the plots of Fig. 5.3, the hysteretic behavior of this brace is not simulated as well as the one with a slenderness ratio of 120. Especially the analytical growth effect does not closely match the experimental one for this particular brace. This is mainly due to the dominance of the local buckling effect in braces with a low slenderness ratio, which is not considered in the proposed analytical model,

Fig. 5.4 displays the analytical and experimental hysteresis loops of Brace 3. As mentioned earlier, this brace is made of a W 6x20 section and has a slenderness ratio of 80. Compared to other braces, the hysteresis loops of this brace are quite legible. As observed from the plots of Fig. 5.4, the analytical hysteresis loops almost perfectly match their experimental counterparts.

Fig. 5.5 displays the analytical and experimental hysteresis loops of Brace 4. Similar to Brace 3, this brace is also made of a W 6x20 section and has a slenderness ratio of 80. However, this brace experiences two distinct tensile plastic deformations following the end of Zone 4 at cycles 4 and 5. As observed from the plots of Fig. 5.5, the analytical hysteresis loops match their experimental counterparts quite well.

Fig. 5.6 displays the analytical and experimental hysteresis loops of Brace 5 which is also made of a W 6x20 section and has a slenderness ratio of 80. However, in the case of this brace, the first displacement cycle is applied in tension causing axial yielding of the specimen. Due to Bauschinger effect, the buckling load in the first compression cycle following this tensile loading cycle is smaller than those of Braces 3 and 4 which are identical to this brace (W 6x20 and $KL/r=80$) as observed from the experimental results shown in Fig. 5.6. Comparison of the analytical hysteresis loops with the experimental ones reveals that the reduction in the buckling load capacity due to the initial tensile loading cycle (Bauschinger effect) as well as other parts of the hysteresis loops are analytically simulated reasonably well.

Fig. 5.7 displays the analytical and experimental hysteresis loops of Brace 7. This brace is made of a W 6×15.5 section and has a slenderness ratio of 40. In this brace, the first displacement cycle is also applied in tension causing axial yielding of the specimen. Comparison of the analytical hysteresis loops with the experimental ones reveals that the buckling load capacity in the first compressive displacement cycle is computed reasonably well. Furthermore, the experimental hysteresis loops are analytically simulated better than that of Brace 2 which also has a slenderness ratio of 40. This is mainly results from the reduced buckling capacity of Brace 7 due to the initial tensile loading cycle causing Baushinger effect to kick in. This phenomenon reduced the magnitude of the compression loads in the subsequent cycles and hence alleviated the effect of local buckling within the brace.

Fig. 5.8 displays the analytical and experimental hysteresis loops of Brace 8. This brace is made of a double L6×3-1/2× 3/8 built-up section and has a slenderness ratio of 80. Fig 5.9 displays the analytical and experimental hysteresis loops of Brace 11. This brace is made of a double C 8×11.5 built-up section and has a slenderness ratio of 120. As observed from the plots of Figs. 5.8 and 5.9, the analytical model proposed in this study simulates the cyclic inelastic behavior of the two built-up braces very well.

Fig. 5.10 displays the analytical and experimental hysteresis loops of Brace 13. This brace is made of a T8×22.5 section and has a slenderness ratio of 80. In this brace, although most of the tensile displacement cycles at the end of Zone 4 reach the yield point in tension, a few of these tensile cycles (cycles 9, 11, 13 and 14) stopped before tensile axial yielding of the brace takes place. This results in a residual transverse displacement (residual kink) within the brace upon the removal of the load (i.e at $P=0$ at the end of Zone 5). This residual kink further reduces the buckling capacity of the brace in the subsequent cycle as observed from the experimental hysteresis loops presented in Fig. 5.10. The analytical plots presented in the figure reveals that the proposed analytical model is capable of successfully simulating the reduction of the buckling load capacity of the brace due to the effect of the residual kink.

Figs. 5.11 and 5.12 display the analytical and experimental hysteresis loops of Brace 15 and 18. Both braces are made of tubular sections. Brace 15 is made of a pipe section O4×0.257 and has a slenderness ratio of 80. Brace 18 is made of a square box section TS4×0.5 and has a slenderness ratio of 80 as well. As observed from the plots of Figs. 5.11 and 5.12, the analytical model proposed in this study simulates the cyclic inelastic behavior of the two tubular braces reasonably well.

5.3.2 Comparison of the Hysteresis Envelopes

Because of an infinite variety of cyclic patterns that may be applied to a brace, it is convenient to make use of envelopes for a family of hysteresis loops obtained at the end of the applied displacement history for comparison purposes. This makes a one-to-one comparison of the analytical and experimental cyclic behavior of the 11 braces on the same graph possible. Comparison of the experimental and analytical envelopes are presented Figs. 5.13-5.23. As observed from the figures a reasonably good agreement is found between the analytical and experimental hysteresis envelopes. Only a slight discrepancy is observed between the hysteresis envelopes within the envelope of Zone 3 and envelope merging the ends of Zone 4.

5.4 Comparison of the Proposed Analytical Model with the Available Models

In this section, the analytical model developed in this study is compared with the refined physical theory models of Ikeda and Mahin (1984) (Figs. 5.24-5.27) and Jin and El-Tawil (2003) (Fig. 5.28) as well as with the phenomenological model of Ikeda et al. (1984) (Fig. 5.29-36). As observed from the figures, in most cases, the proposed analytical model simulates the inelastic cyclic axial force-deformation behavior of braces better than those of the existing analytical models considered in this study.

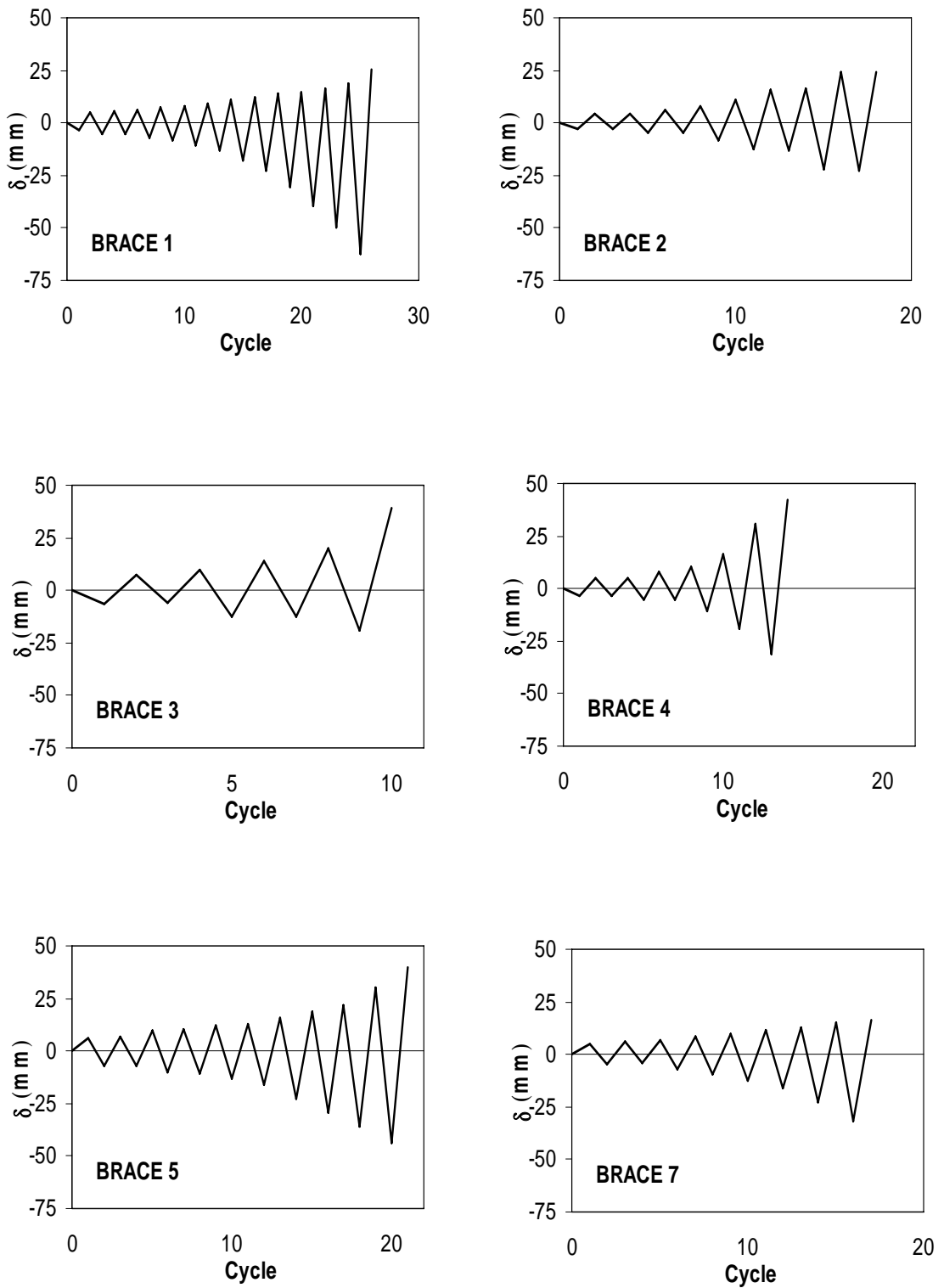


Fig. 5.1 Displacement Histories

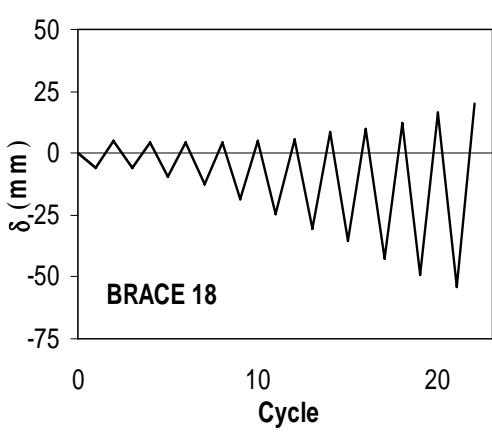
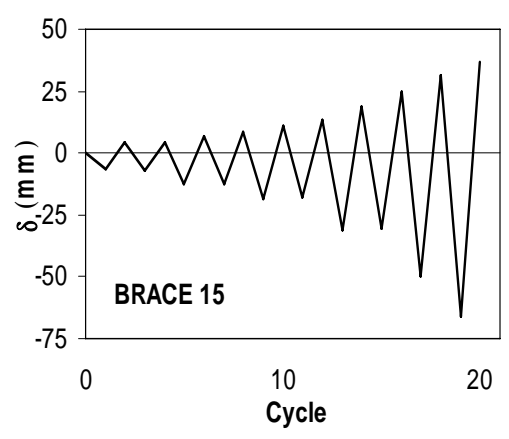
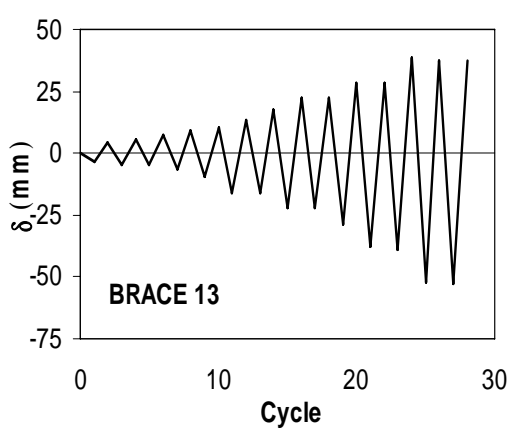
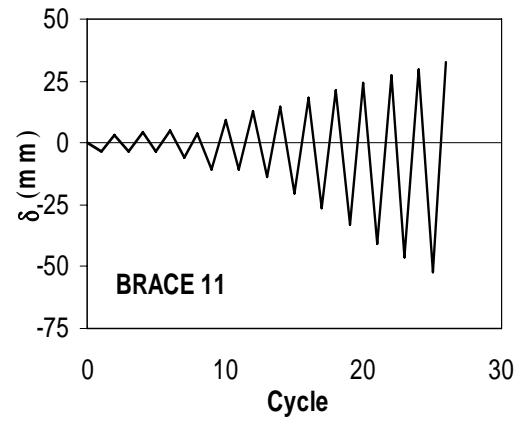
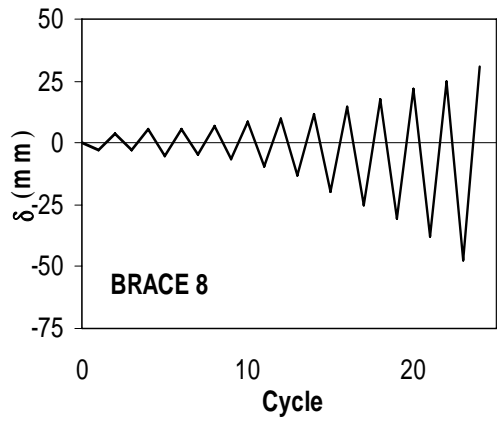
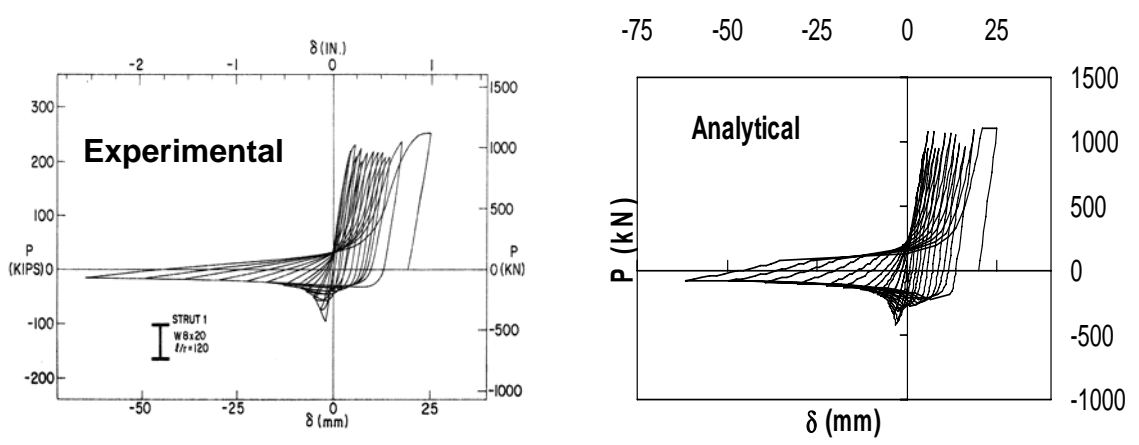
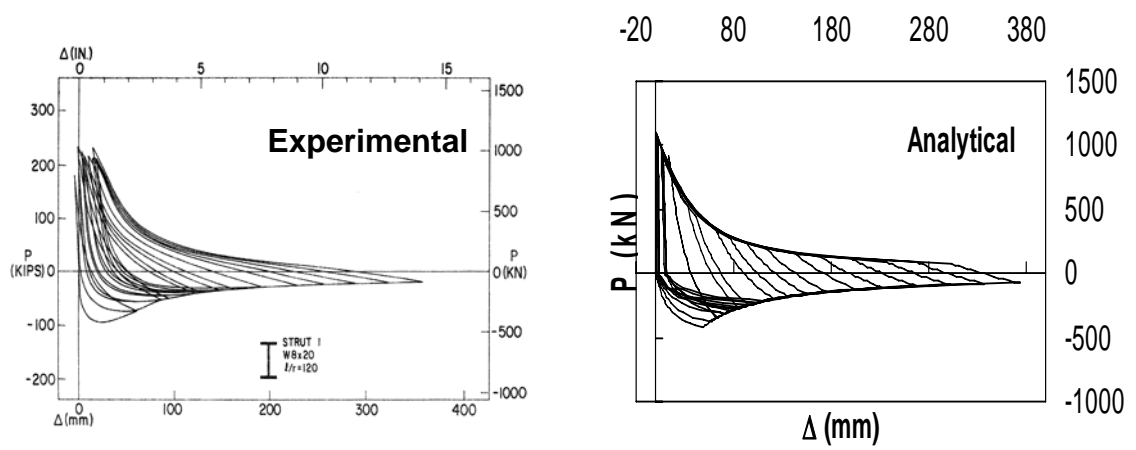


Fig. 5.1 (continued) Displacement Histories

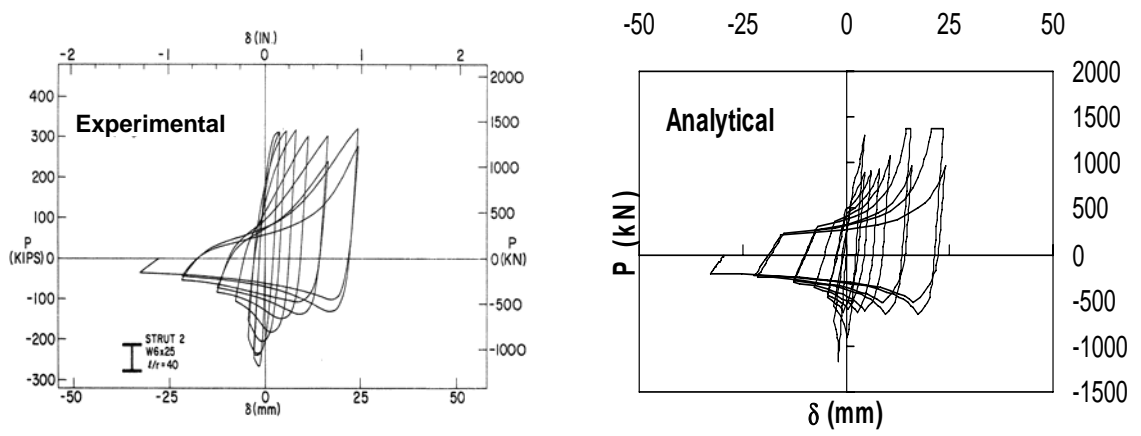


(a)

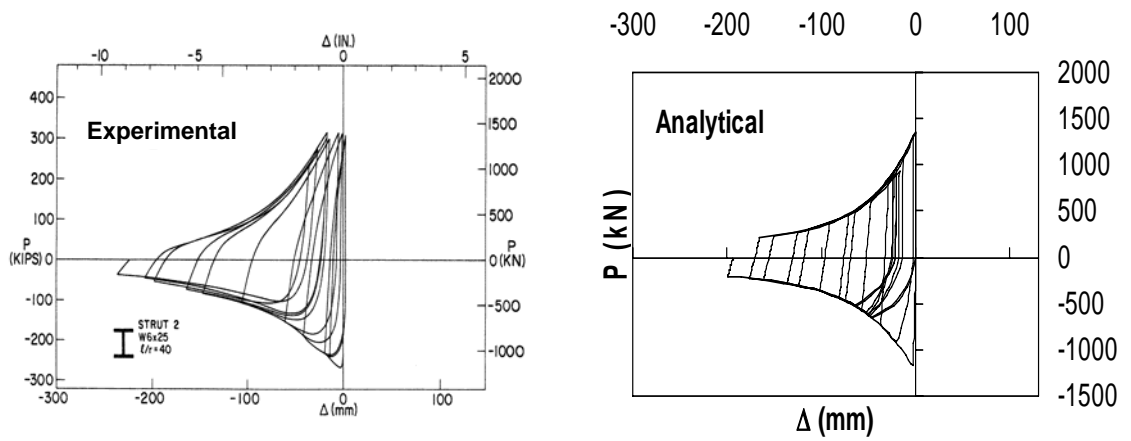


(b)

Fig. 5.2 Comparison of Analytical and Experimental Curves for Brace 1 (a) Axial Force-Axial Displacement (b) Axial Force- Transverse Displacement

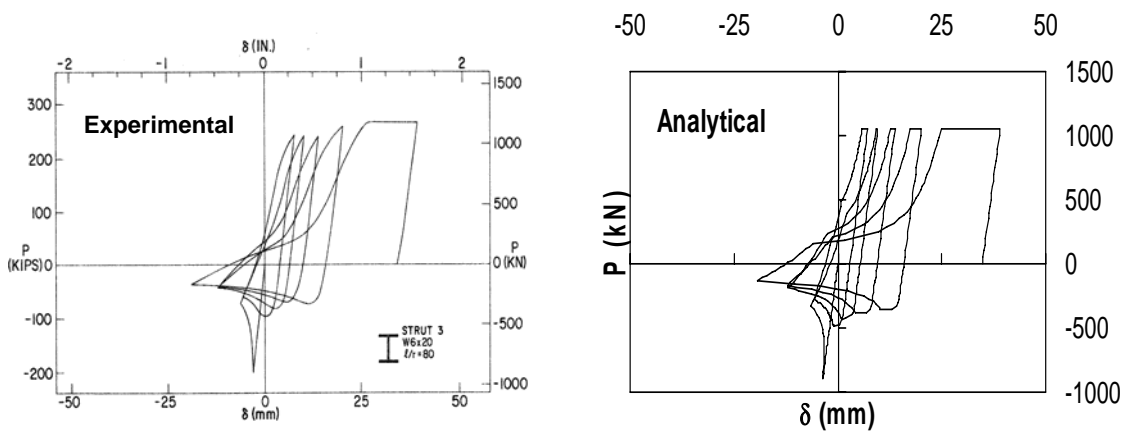


(a)

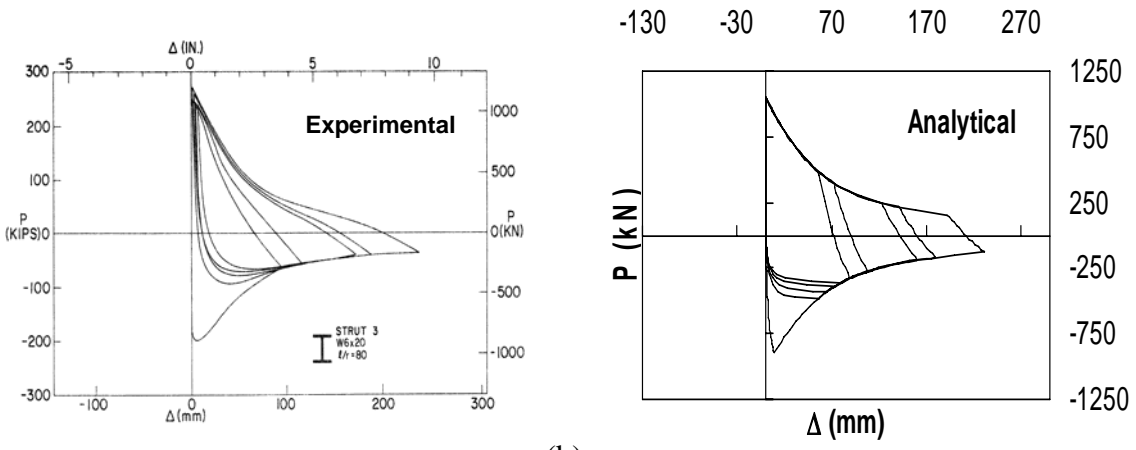


(b)

Fig. 5.3 Comparison of Analytical and Experimental Curves for Brace 2 (a) Axial Force-Axial Displacement (b) Axial Force- Transverse Displacement

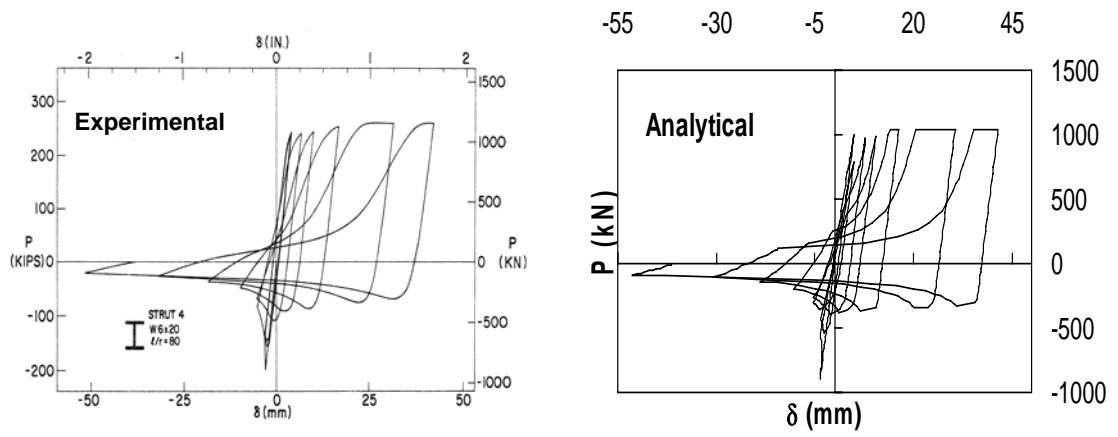


(a)

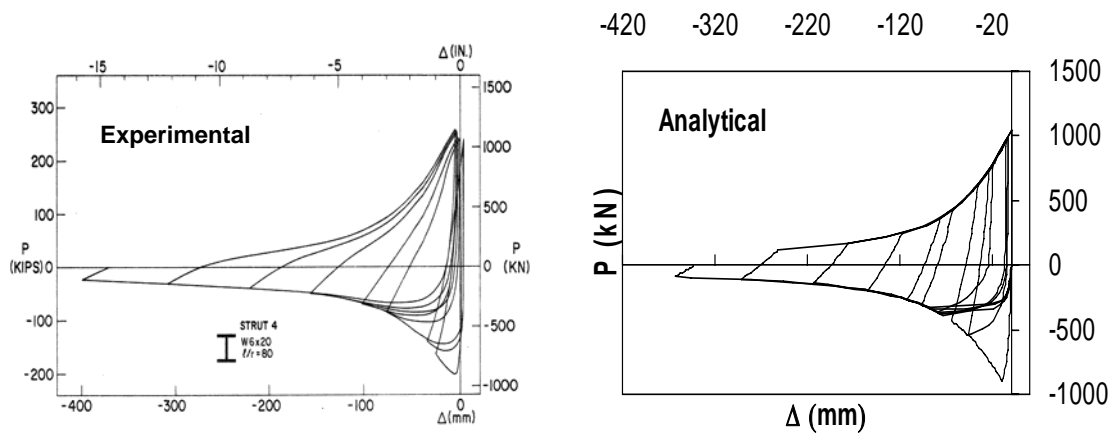


(b)

Fig. 5.4 Comparison of Analytical and Experimental Curves for Brace 3 (a) Axial Force-Axial Displacement (b) Axial Force- Transverse Displacement

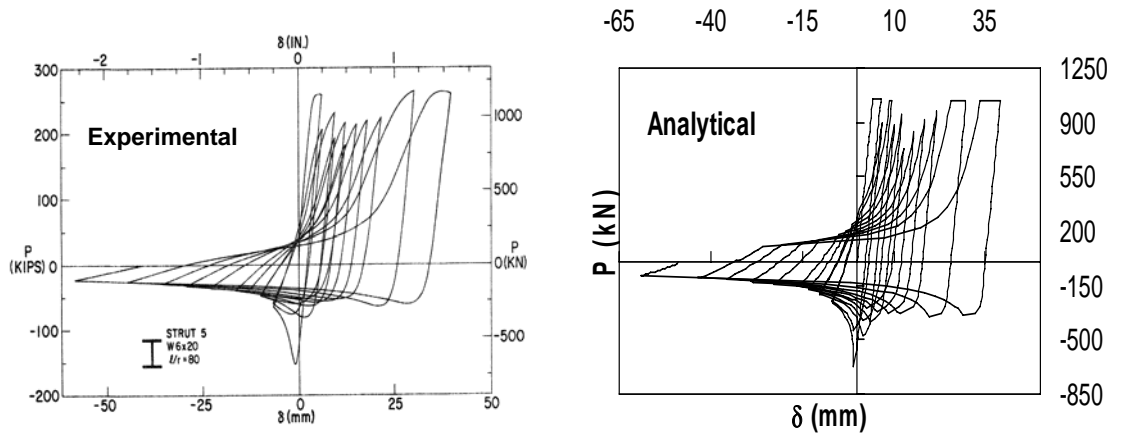


(a)

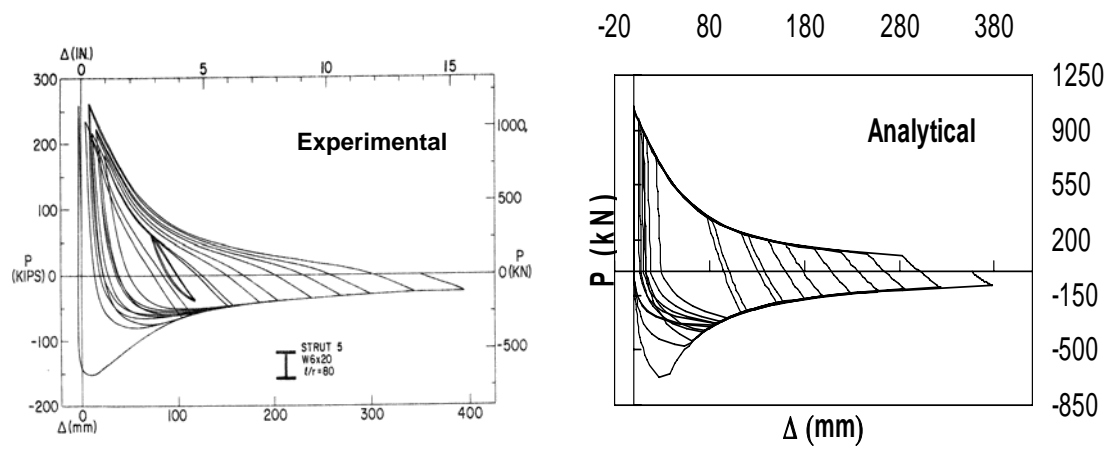


(b)

Fig. 5.5 Comparison of Analytical and Experimental Curves for Brace 4 (a) Axial Force-Axial Displacement (b) Axial Force- Transverse Displacement

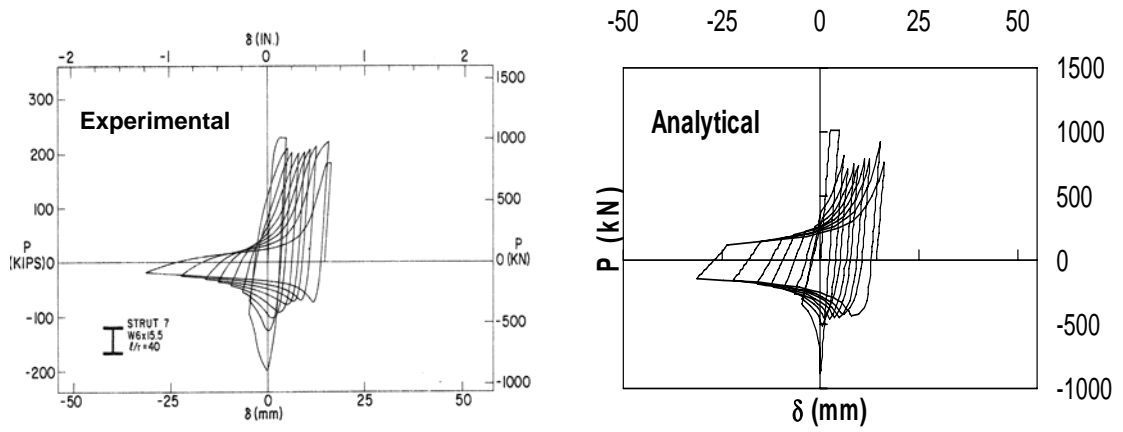


(a)

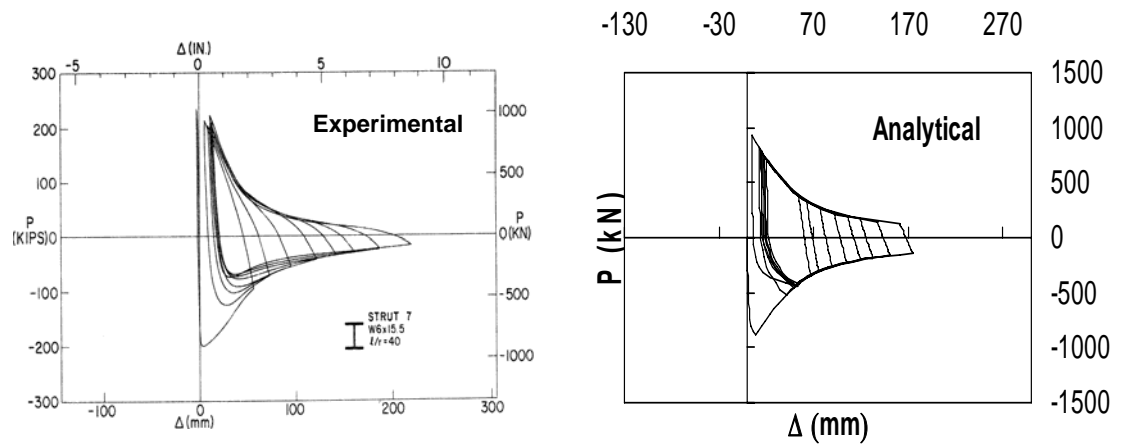


(b)

Fig. 5.6 Comparison of Analytical and Experimental Curves for Brace 5 (a) Axial Force-Axial Displacement (b) Axial Force- Transverse Displacement

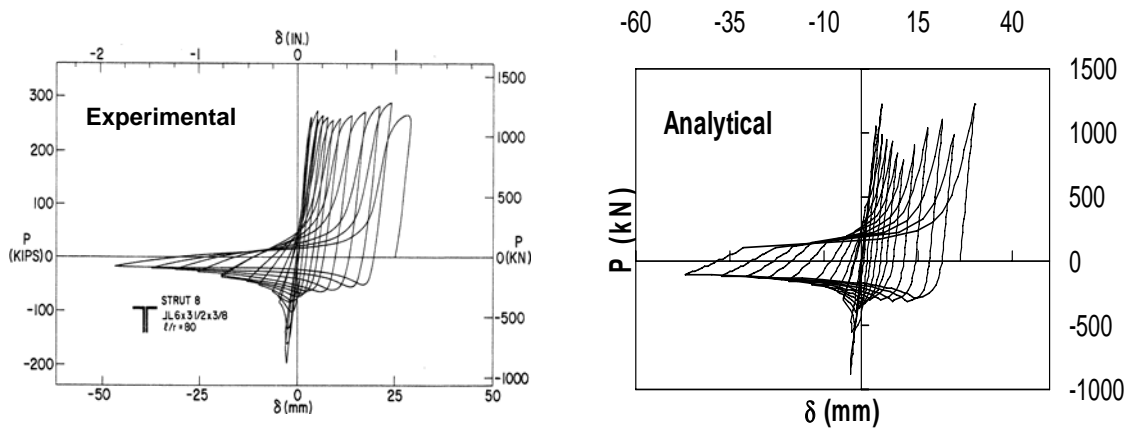


(a)

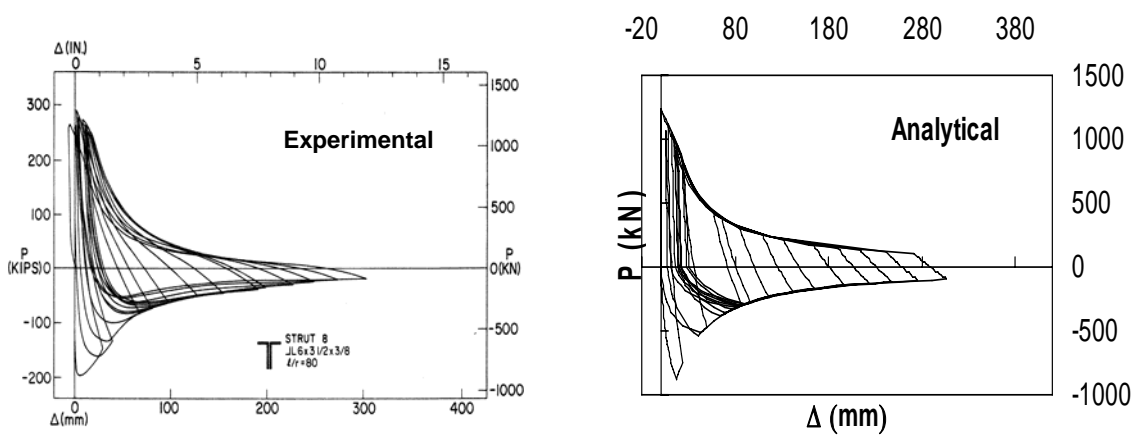


(b)

Fig. 5.7 Comparison of Analytical and Experimental Curves for Brace 7 (a) Axial Force-Axial Displacement (b) Axial Force- Transverse Displacement

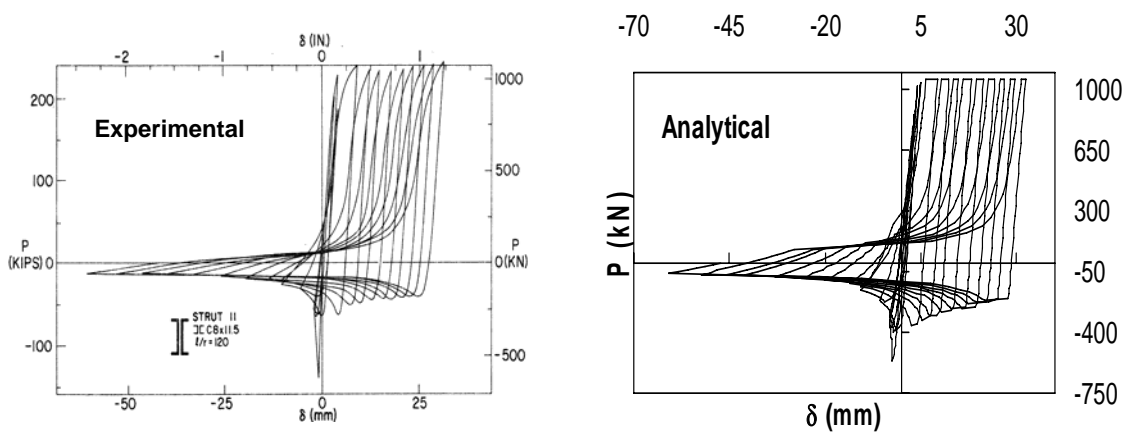


(a)

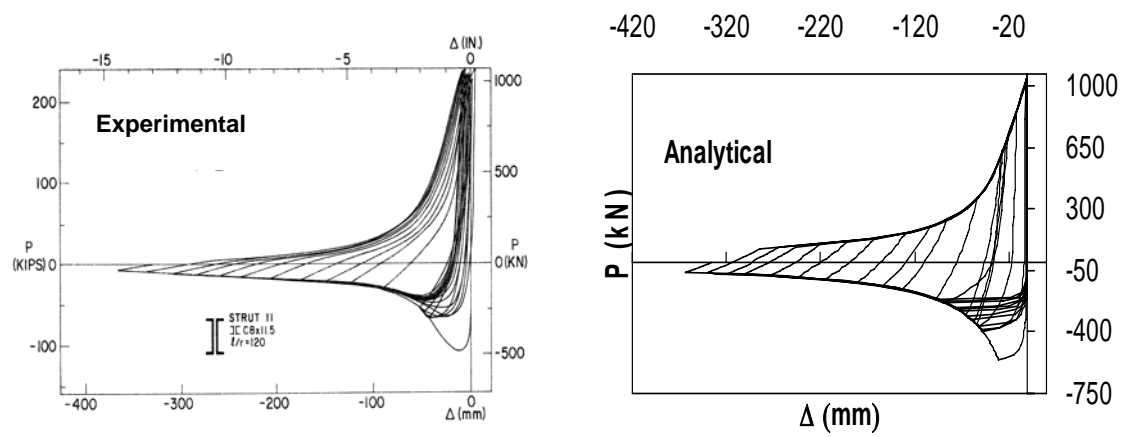


(b)

Fig. 5.8 Comparison of Analytical and Experimental Curves for Brace 8 (a) Axial Force-Axial Displacement (b) Axial Force- Transverse Displacement

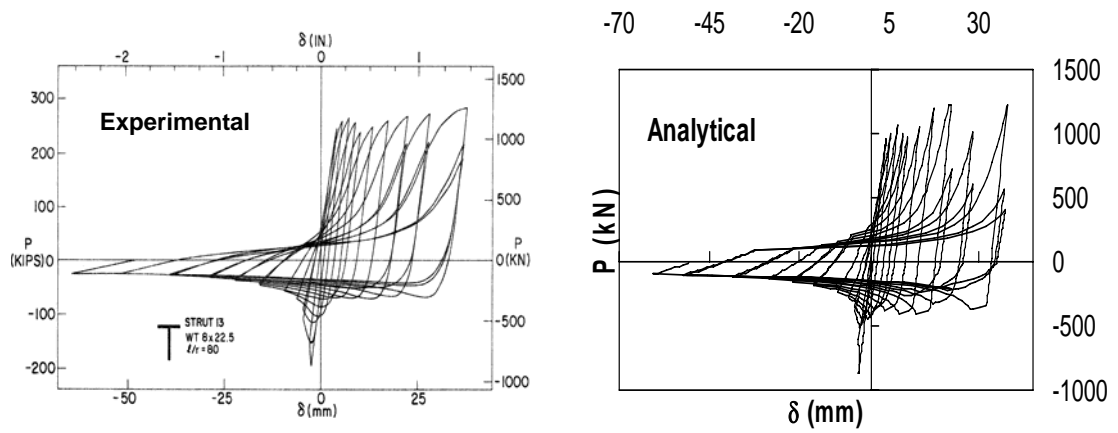


(a)

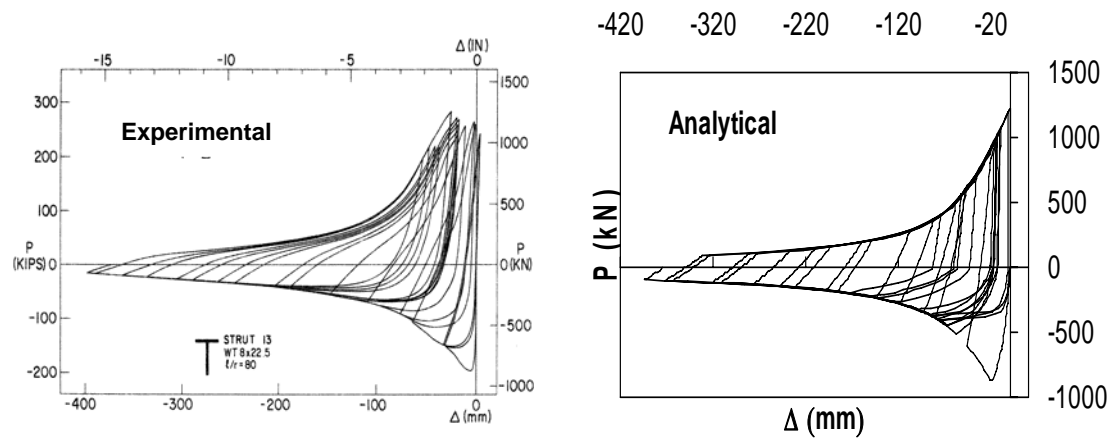


(b)

Fig. 5.9 Comparison of Analytical and Experimental Curves for Brace 11 (a) Axial Force-Axial Displacement (b) Axial Force- Transverse Displacement

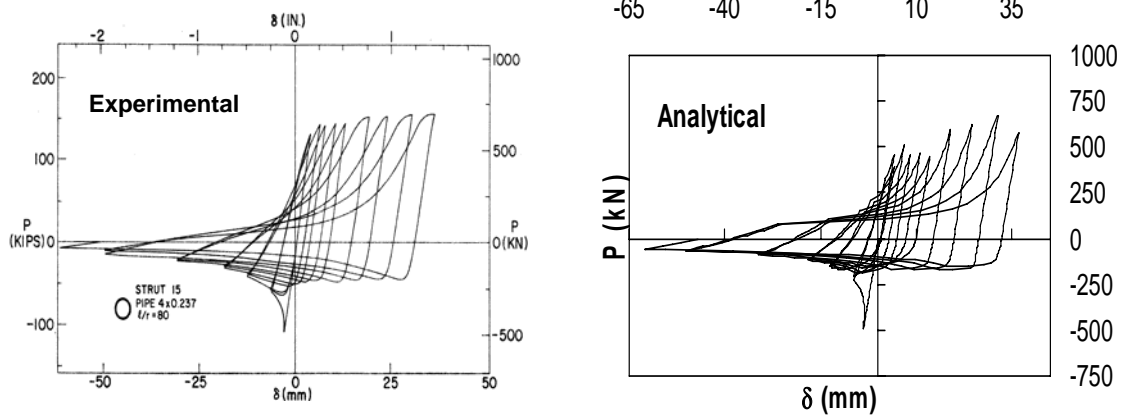


(a)

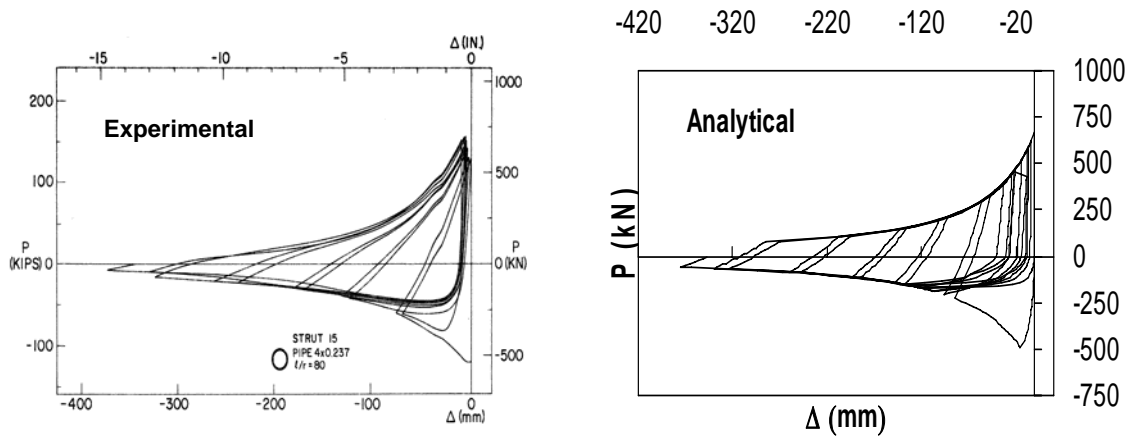


(b)

Fig. 5.10 Comparison of Analytical and Experimental Curves for Brace 13 (a) Axial Force-Axial Displacement (b) Axial Force- Transverse Displacement

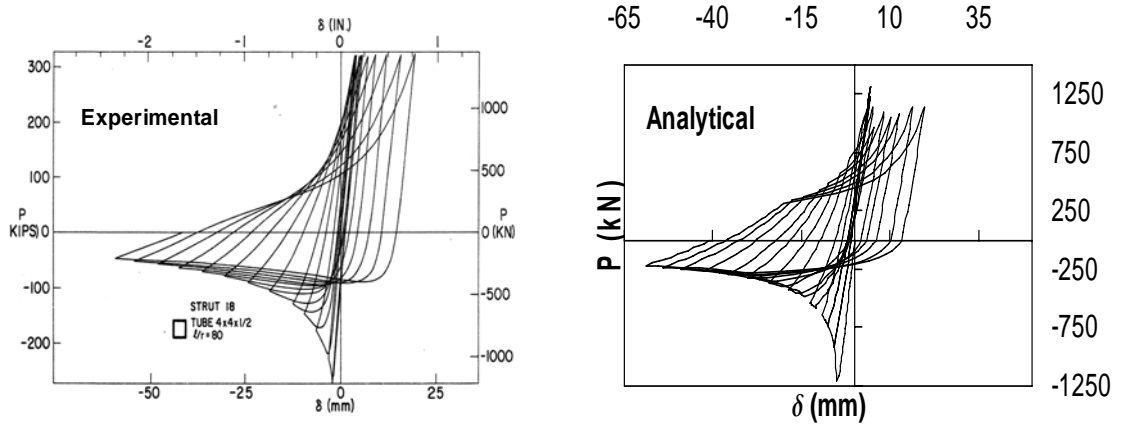


(a)

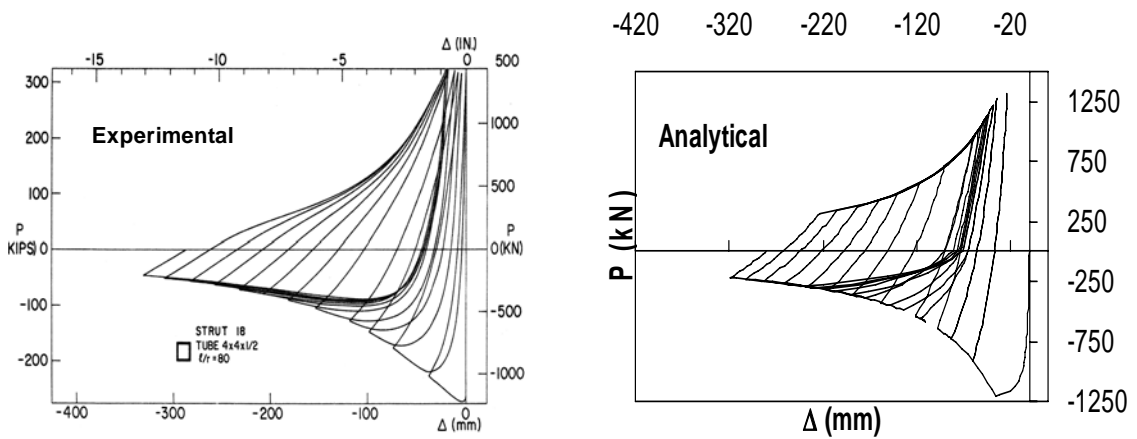


(b)

Fig. 5.11 Comparison of Analytical and Experimental Curves for Brace 15 (a) Axial Force-Axial Displacement (b) Axial Force- Transverse Displacement



(a)



(b)

Fig. 5.12 Comparison of Analytical and Experimental Curves for Brace 18 (a) Axial Force-Axial Displacement (b) Axial Force- Transverse Displacement

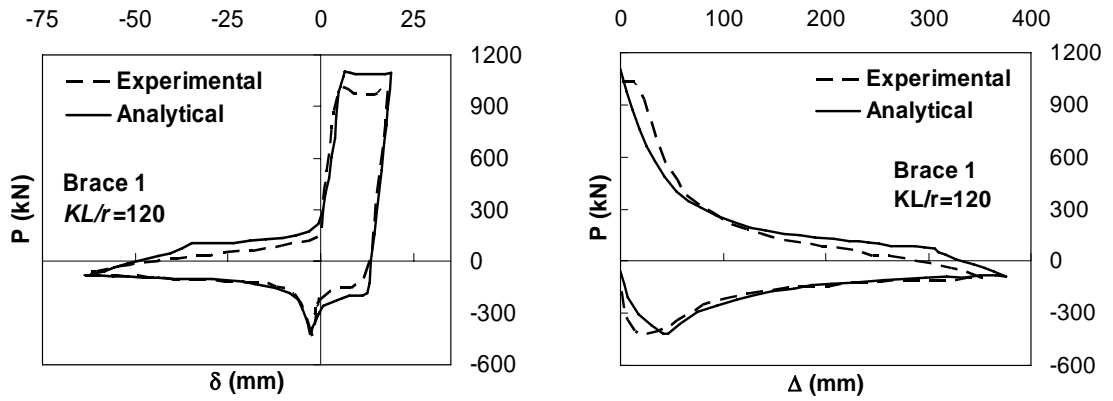


Fig. 5.13 Comparison of experimental and analytical P - δ and P - Δ envelopes for Brace 1

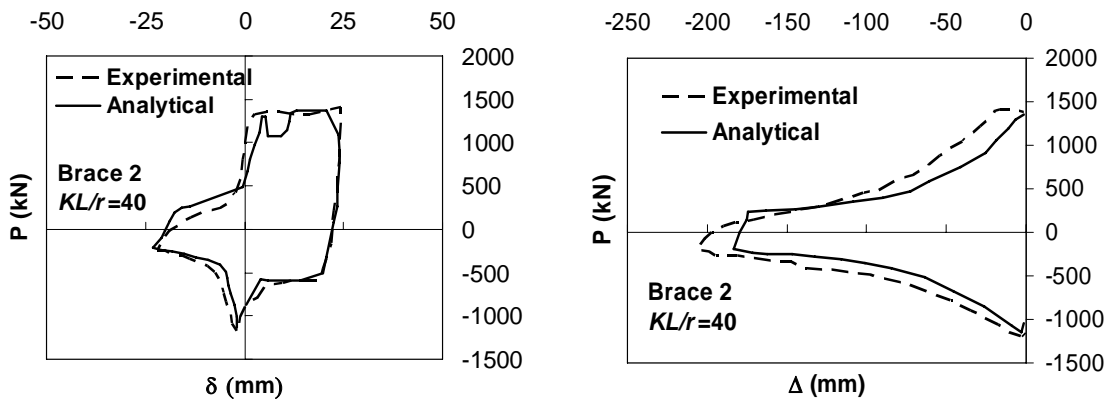


Fig. 5.14 Comparison of experimental and analytical P - δ and P - Δ envelopes for Brace 2

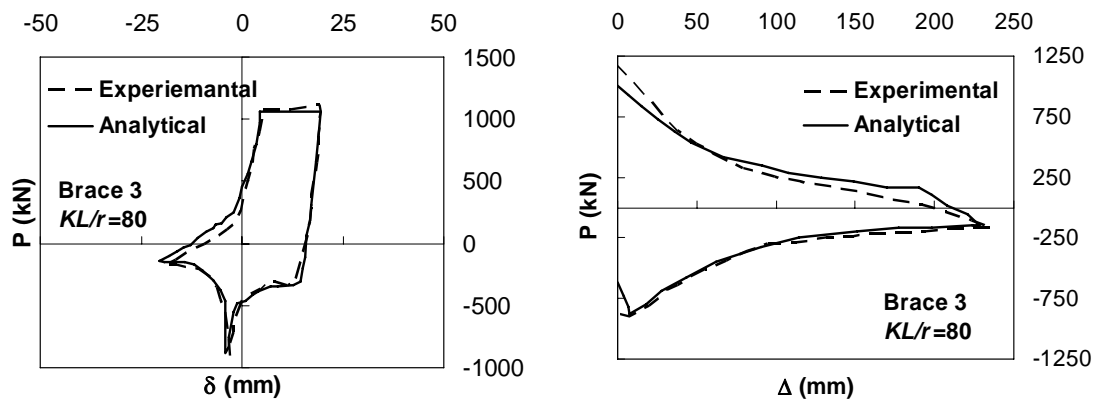


Fig. 5.15 Comparison of experimental and analytical $P-\delta$ and $P-\Delta$ envelopes for Brace 3

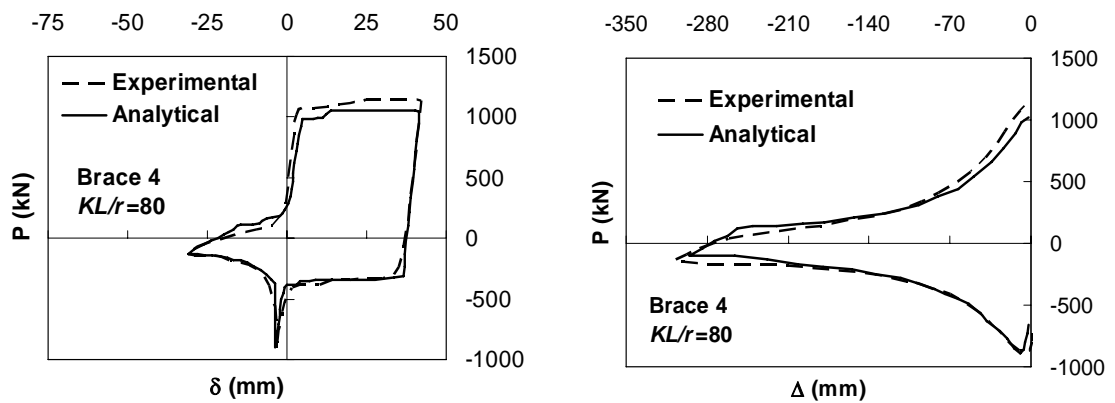


Fig. 5.16 Comparison of experimental and analytical $P-\delta$ and $P-\Delta$ envelopes for Brace 4

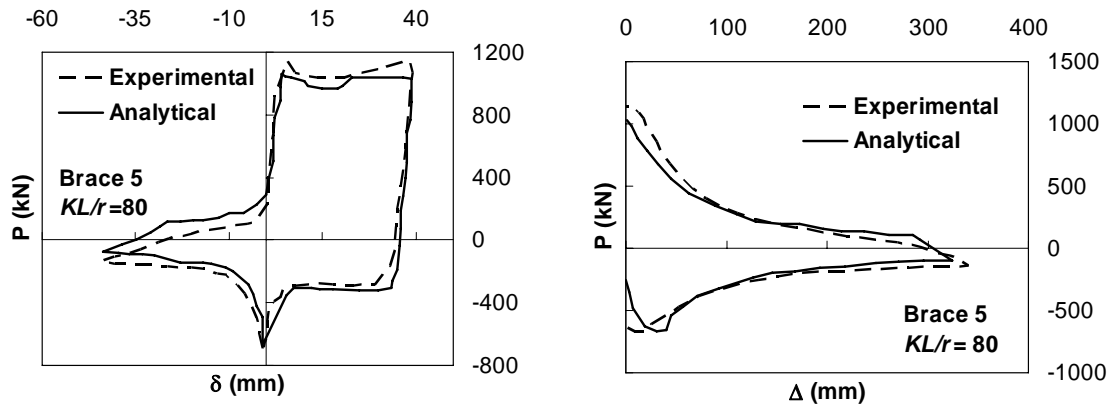


Fig. 5.17 Comparison of experimental and analytical $P-\delta$ and $P-\Delta$ envelopes for Brace 5

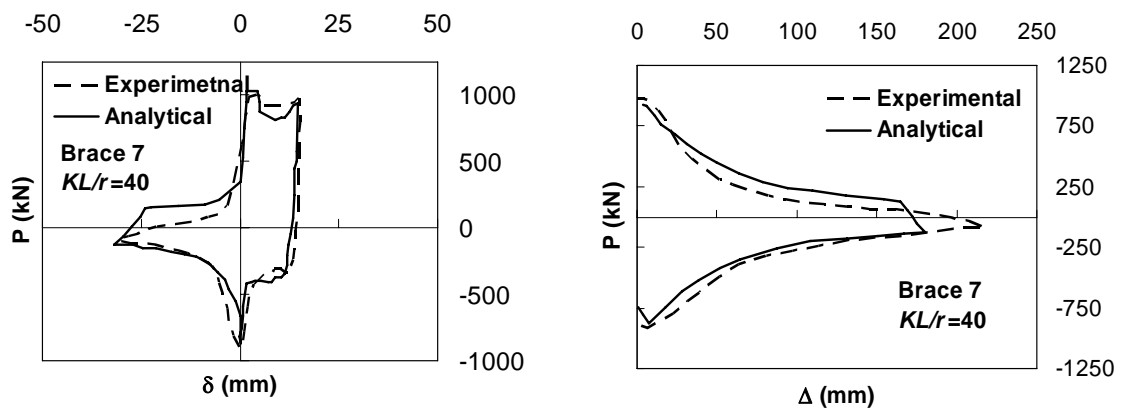


Fig. 5.18 Comparison of experimental and analytical $P-\delta$ and $P-\Delta$ envelopes for Brace 7

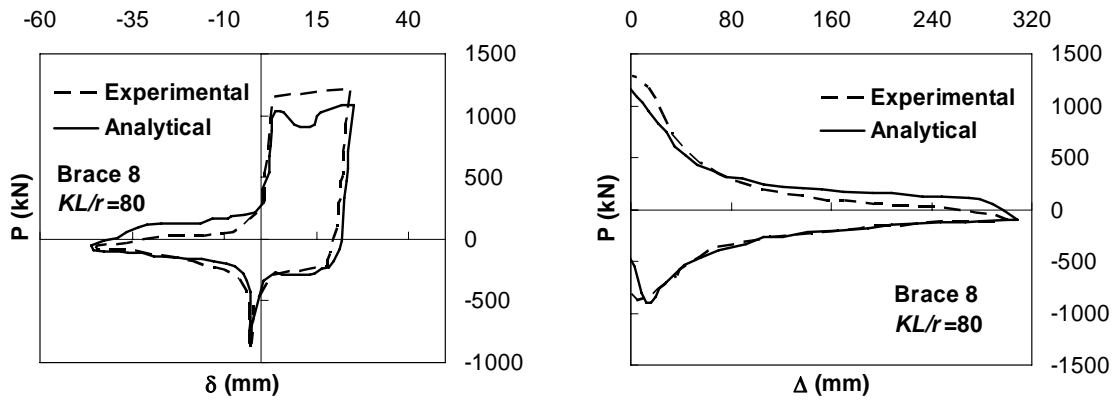


Fig. 5.19 Comparison of experimental and analytical P - δ and P - Δ envelopes for Brace 8

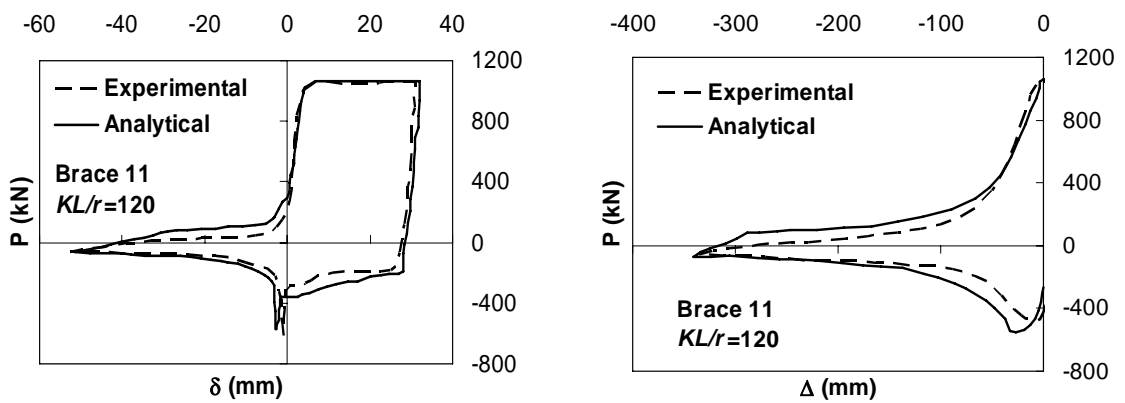


Fig. 5.20 Comparison of experimental and analytical P - δ and P - Δ envelopes for Brace 11

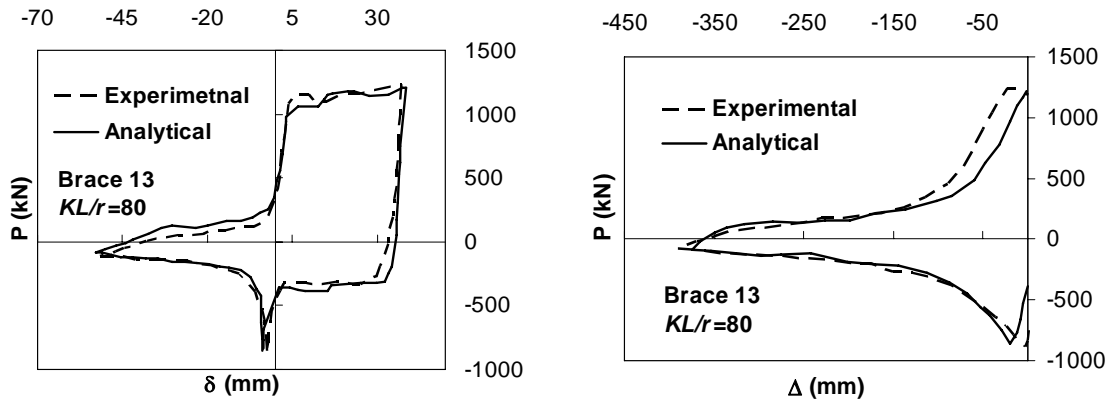


Fig. 5.21 Comparison of experimental and analytical P - δ and P - Δ envelopes for Brace 13

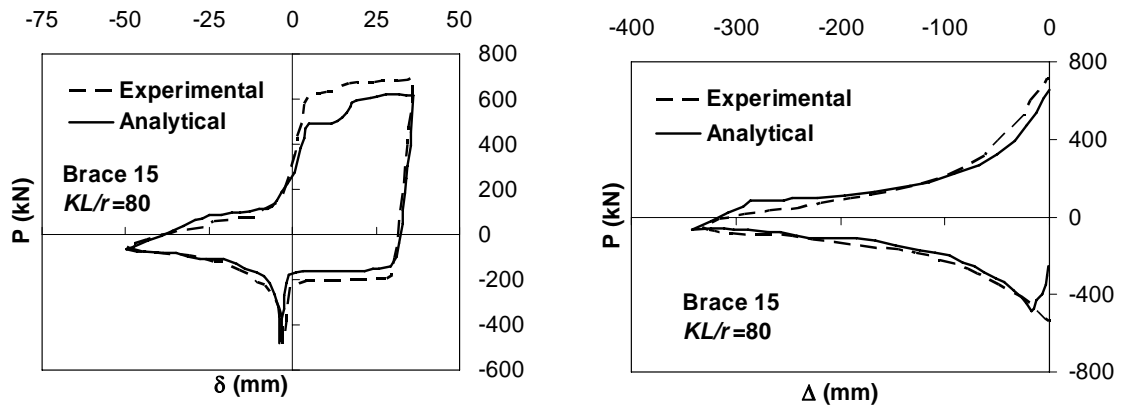


Fig. 5.22 Comparison of experimental and analytical P - δ and P - Δ envelopes for Brace 15

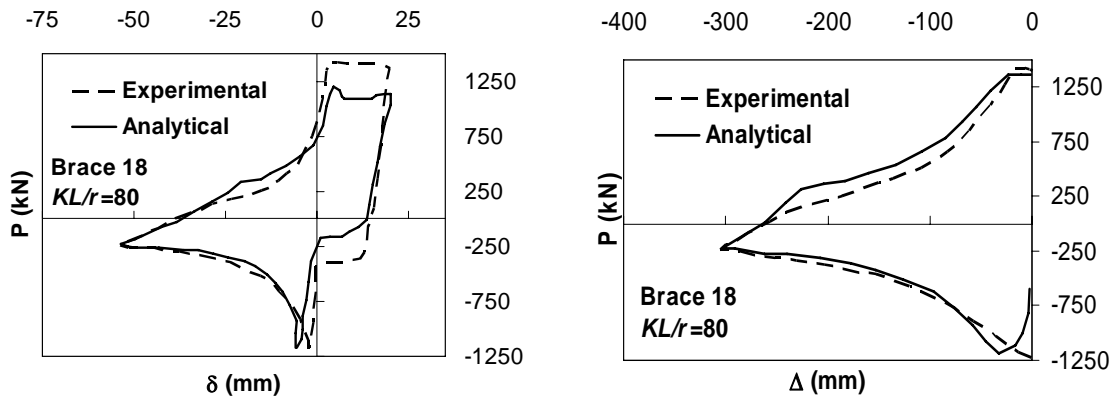


Fig. 5.23 Comparison of experimental and analytical P - δ and P - Δ envelopes for Brace 18

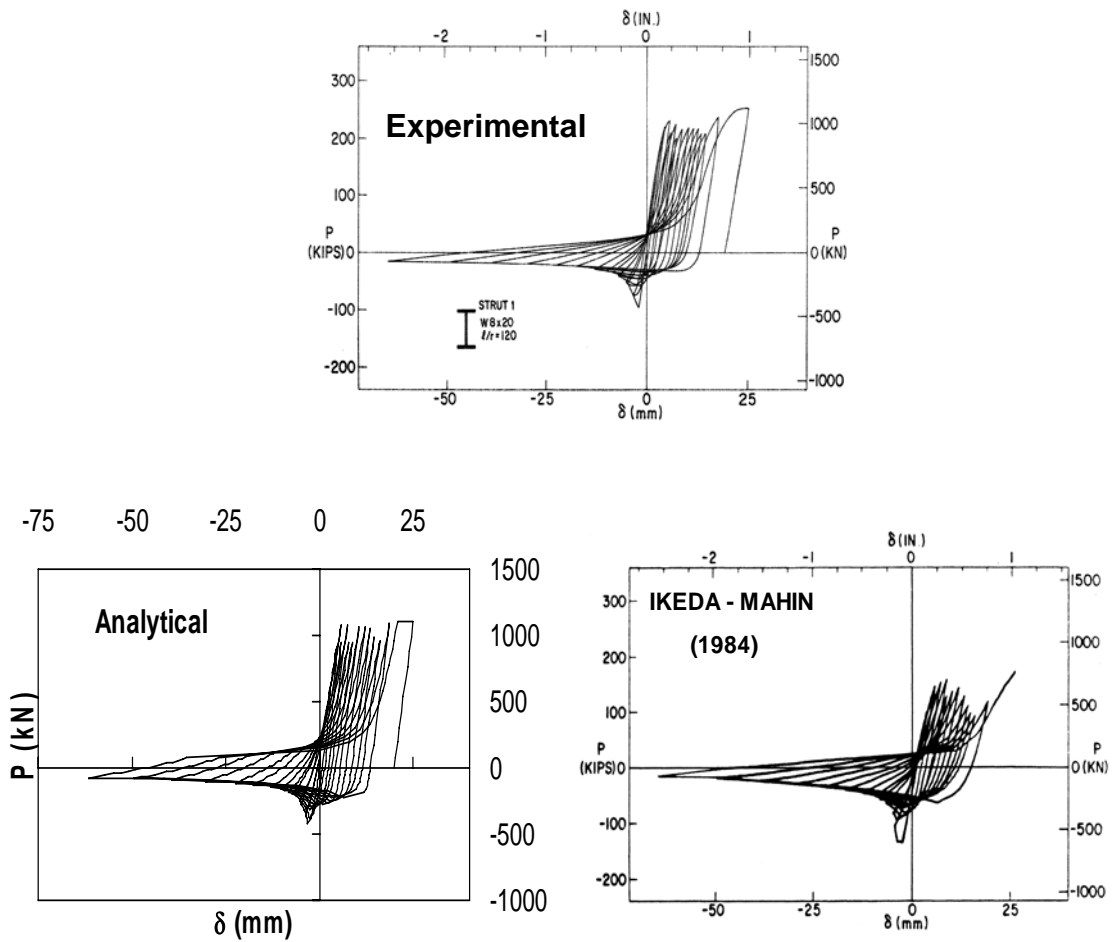


Fig. 5.24 Comparison of the proposed analytical model with the refined physical theory model of Ikeda and Mahin (1984) and the test results of Black et al. (1980) for Brace 1

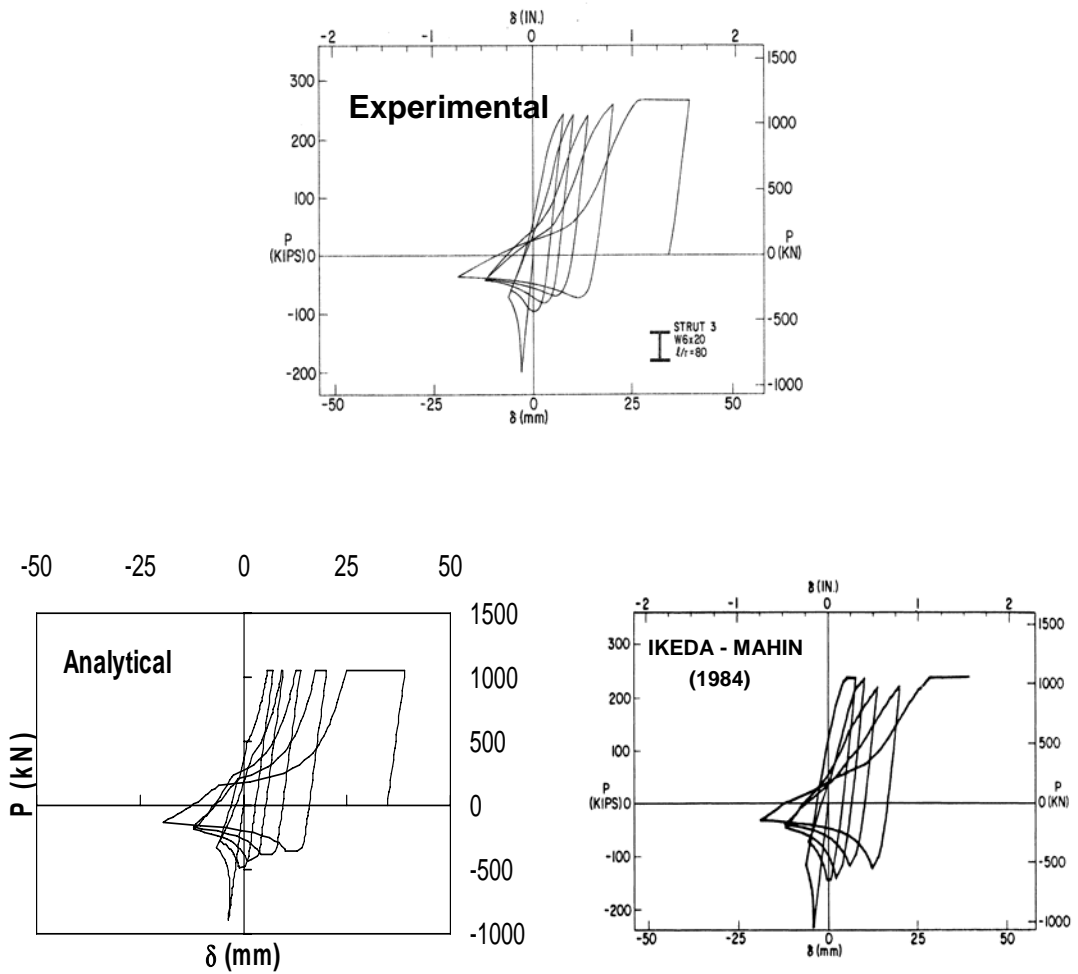


Fig. 5.25 Comparison of the proposed analytical model with the refined physical theory model of Ikeda and Mahin (1984) and the test results of Black et al. (1980) for Brace 3.

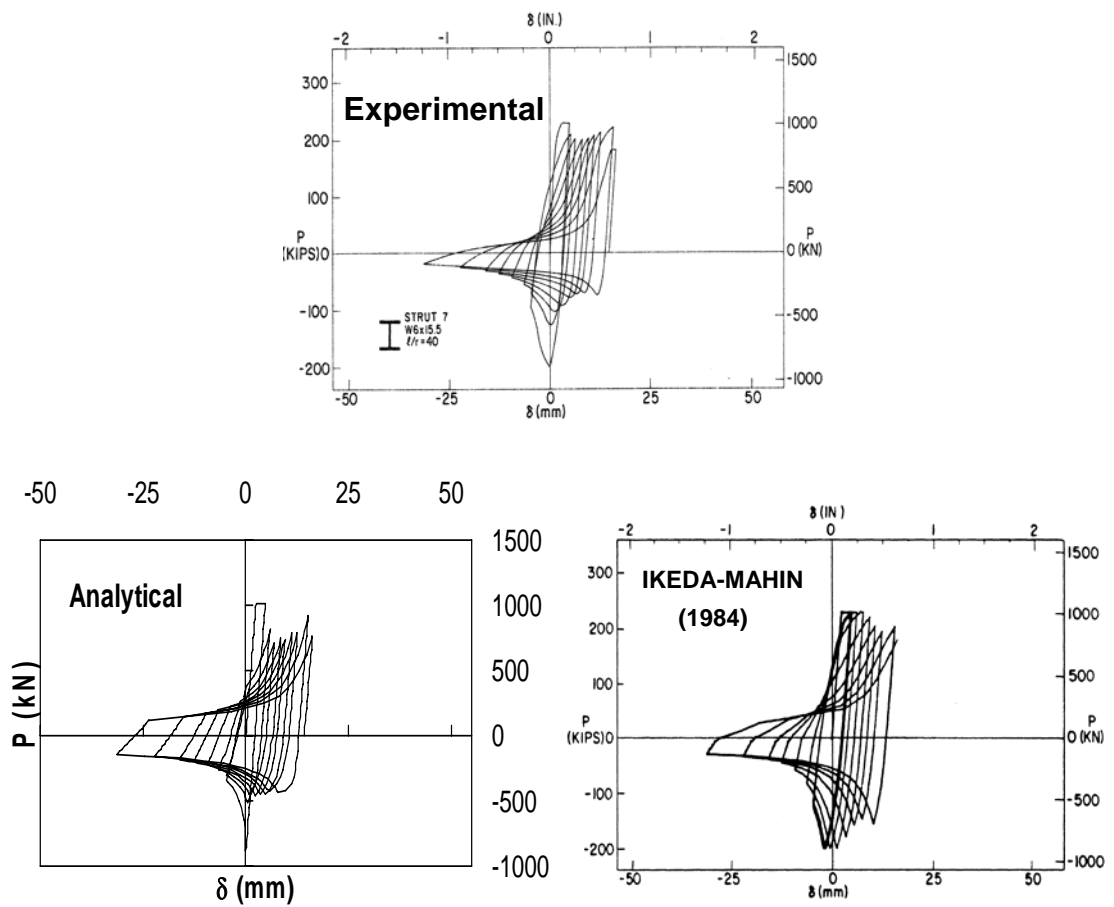


Fig. 5. 26 Comparison of the proposed analytical model with the refined physical theory model of Ikeda and Mahin (1984) and the test results of Black et al. (1980) for Brace 7

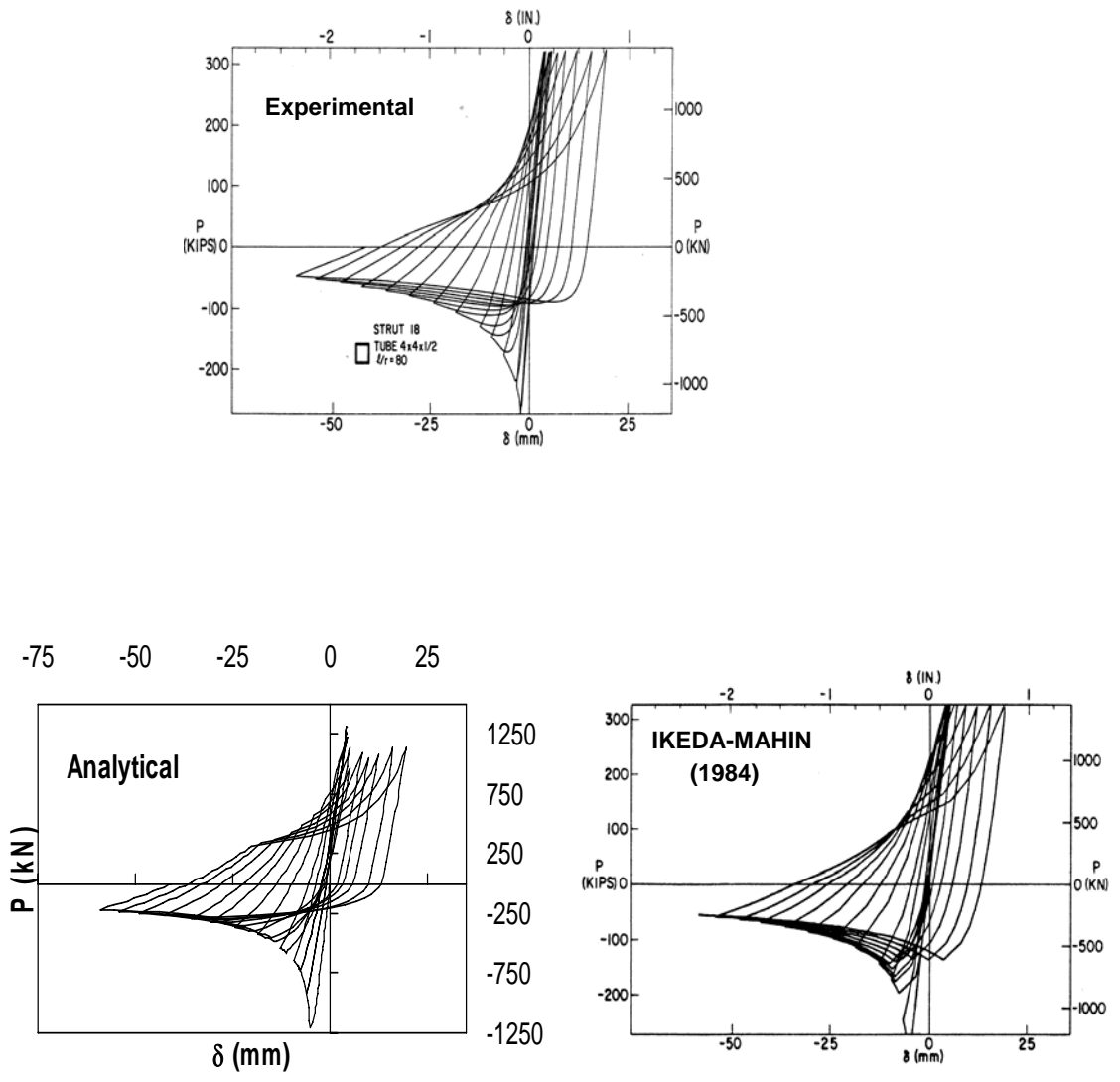


Fig. 5.27 Comparison of the proposed analytical model with the refined physical theory model of Ikeda and Mahin (1984) and the test results of Black et al. (1980) for Brace 18

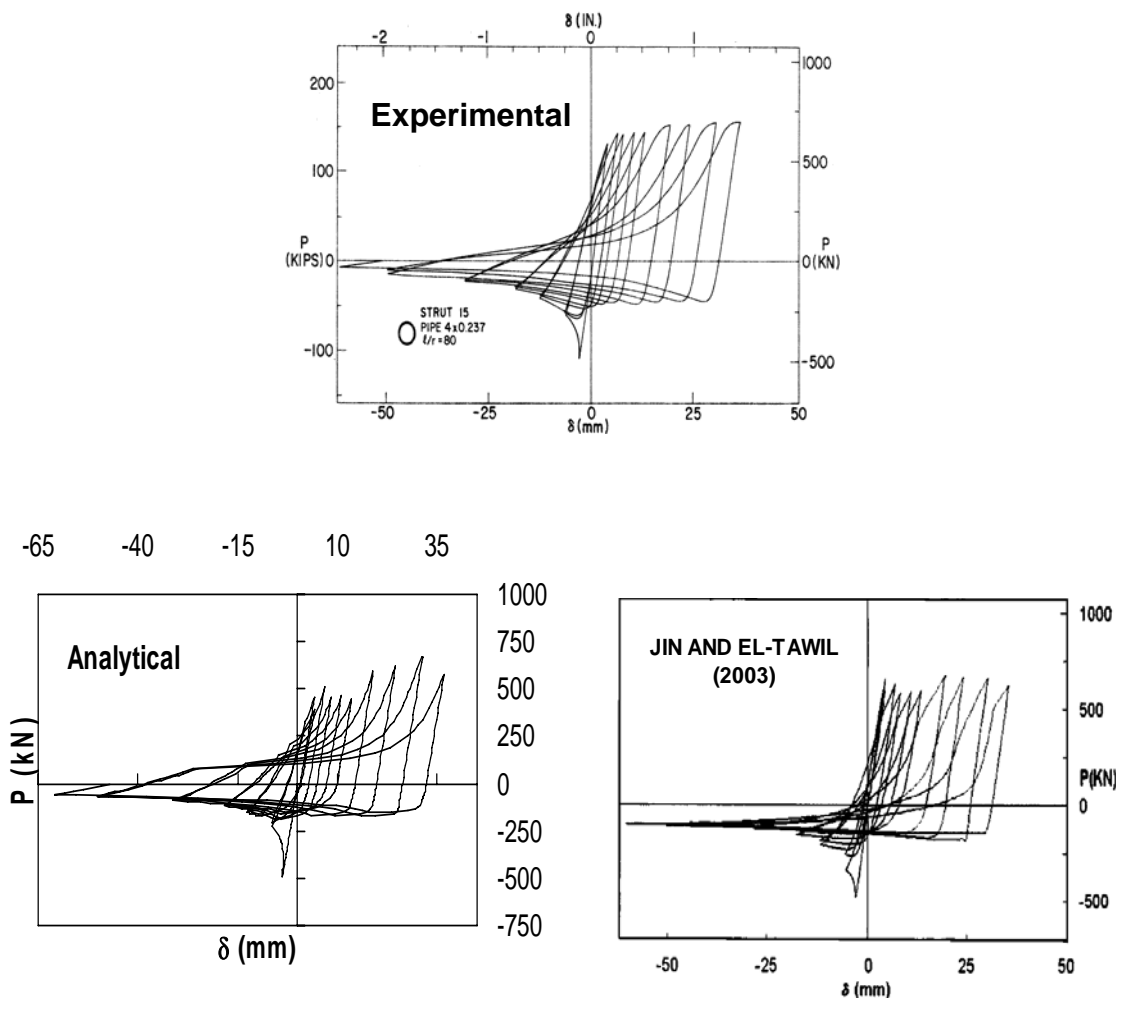


Fig. 5.28 Comparison of the proposed analytical model with model of Jin and El-Tawil (2003) and the test results of Black et al. (1980) for Brace 15

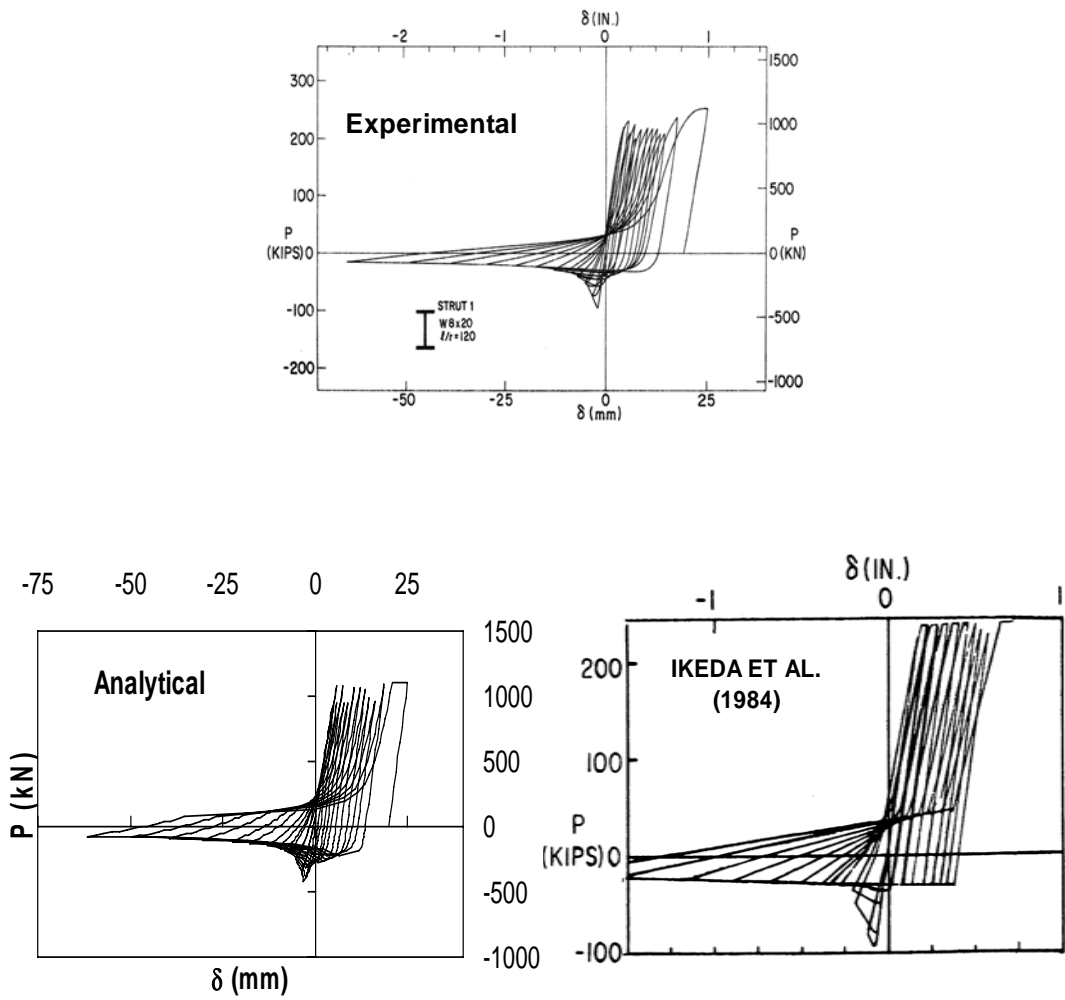


Fig. 5.29 Comparison of the proposed analytical model with the phenomenological model of Ikeda et al. (1984) and the test results of Black et al. (1980) for Brace 1

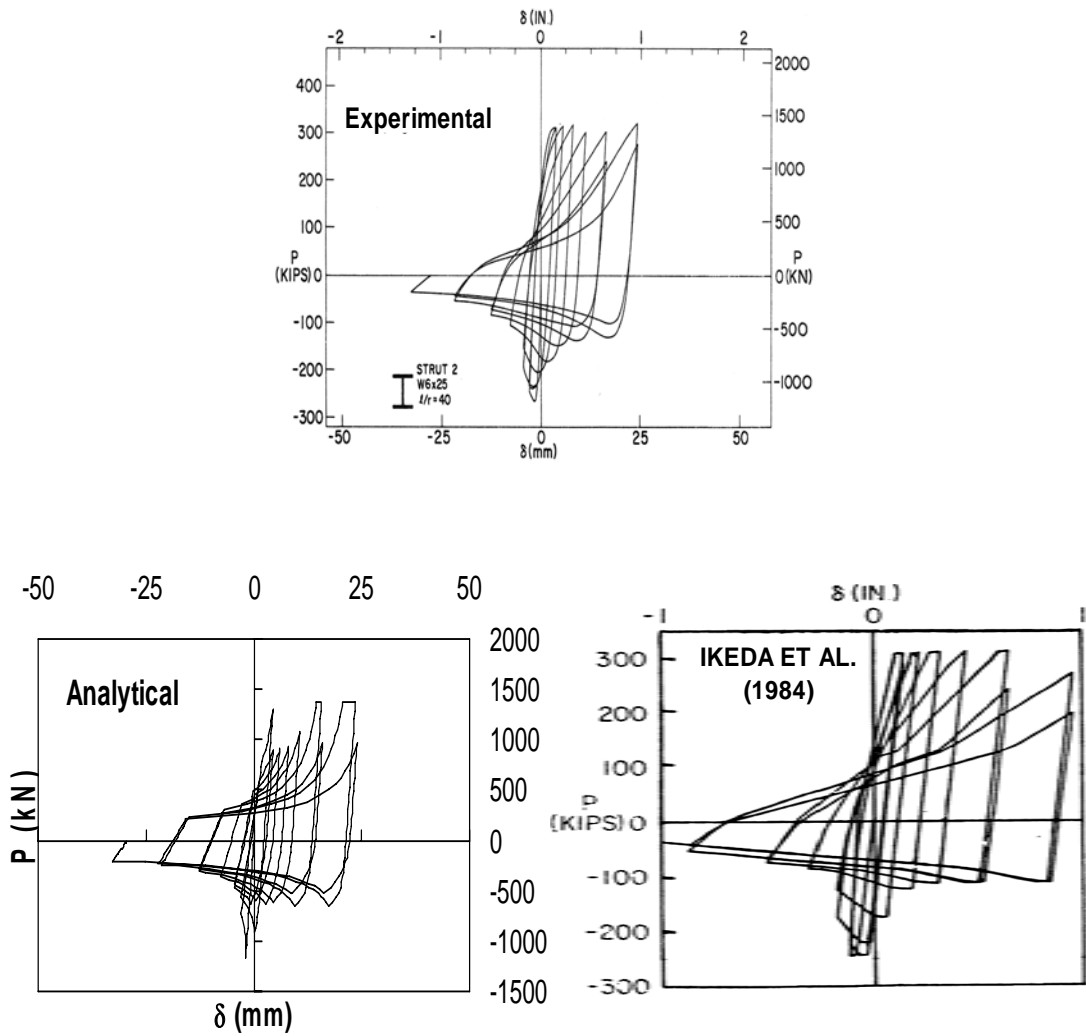


Fig. 5.30 Comparison of the proposed analytical model with the phenomenological model of Ikeda et al. (1984) and the test results of Black et al. (1980) for Brace 2

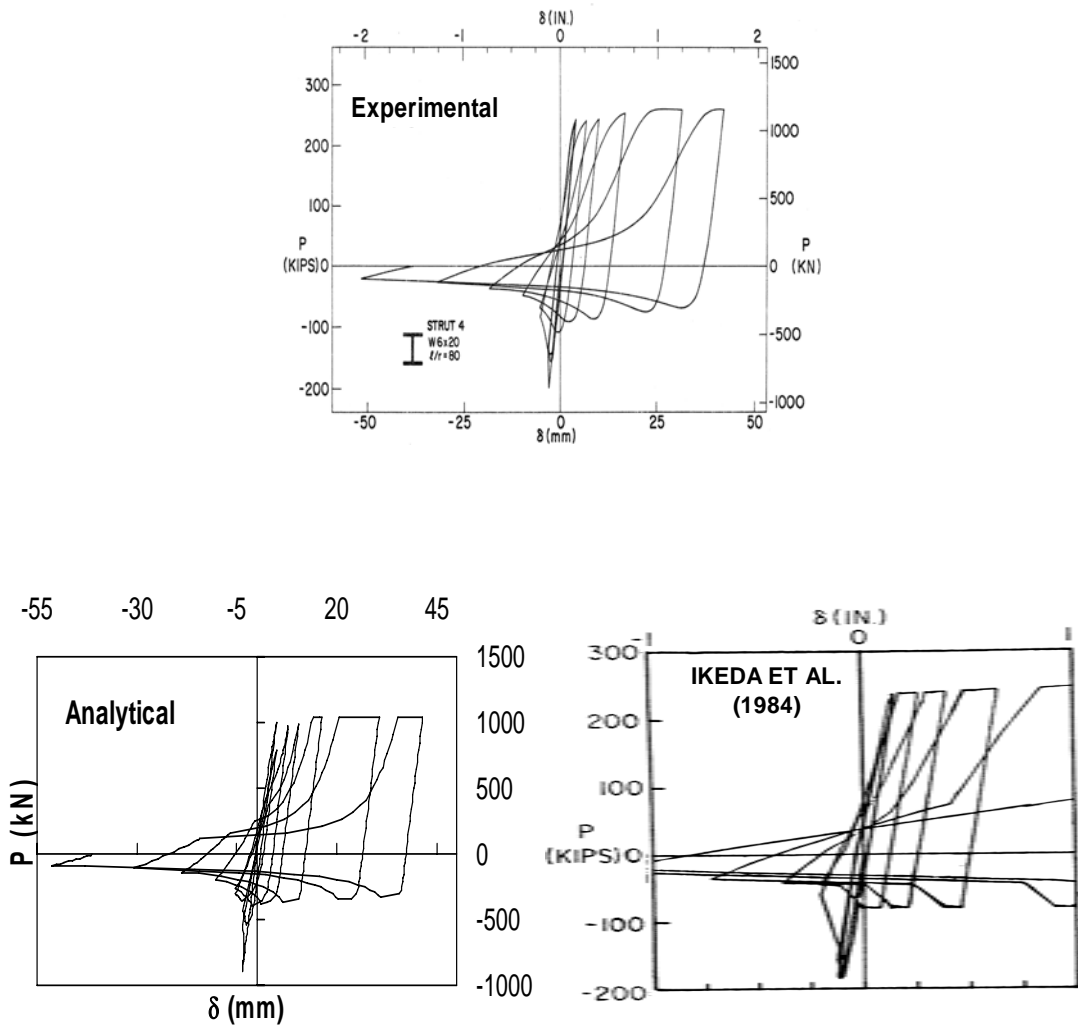


Fig. 5.31 Comparison of the proposed analytical model with the phenomenological model of Ikeda et al. (1984) and the test results of Black et al. (1980) for Brace 4

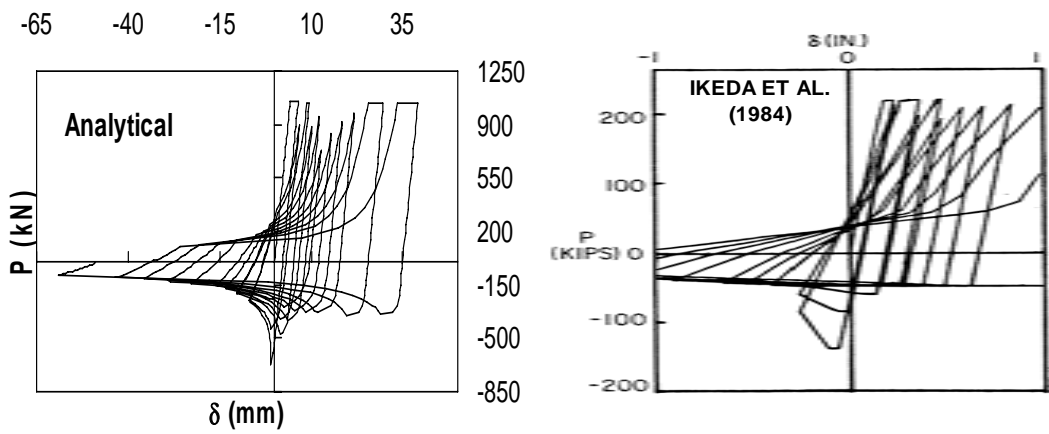
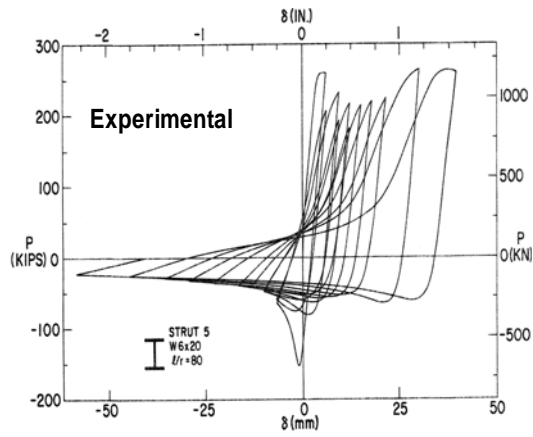


Fig. 5.32 Comparison of the proposed analytical model with the phenomenological model of Ikeda et al. (1984) and the test results of Black et al. (1980) for Brace 5

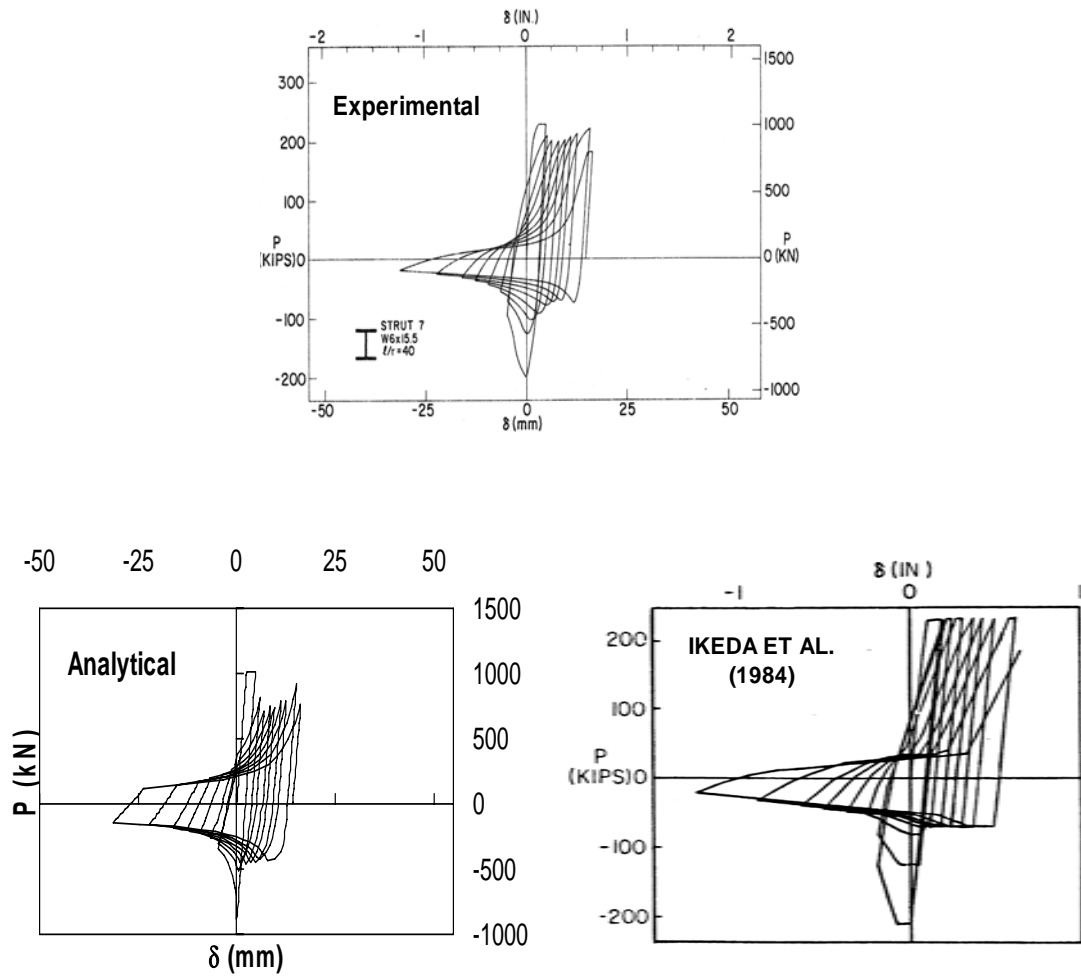


Fig. 5.33 Comparison of the proposed analytical model with the phenomenological model of Ikeda et al. (1984) and the test results of Black et al. (1980) for Brace 7

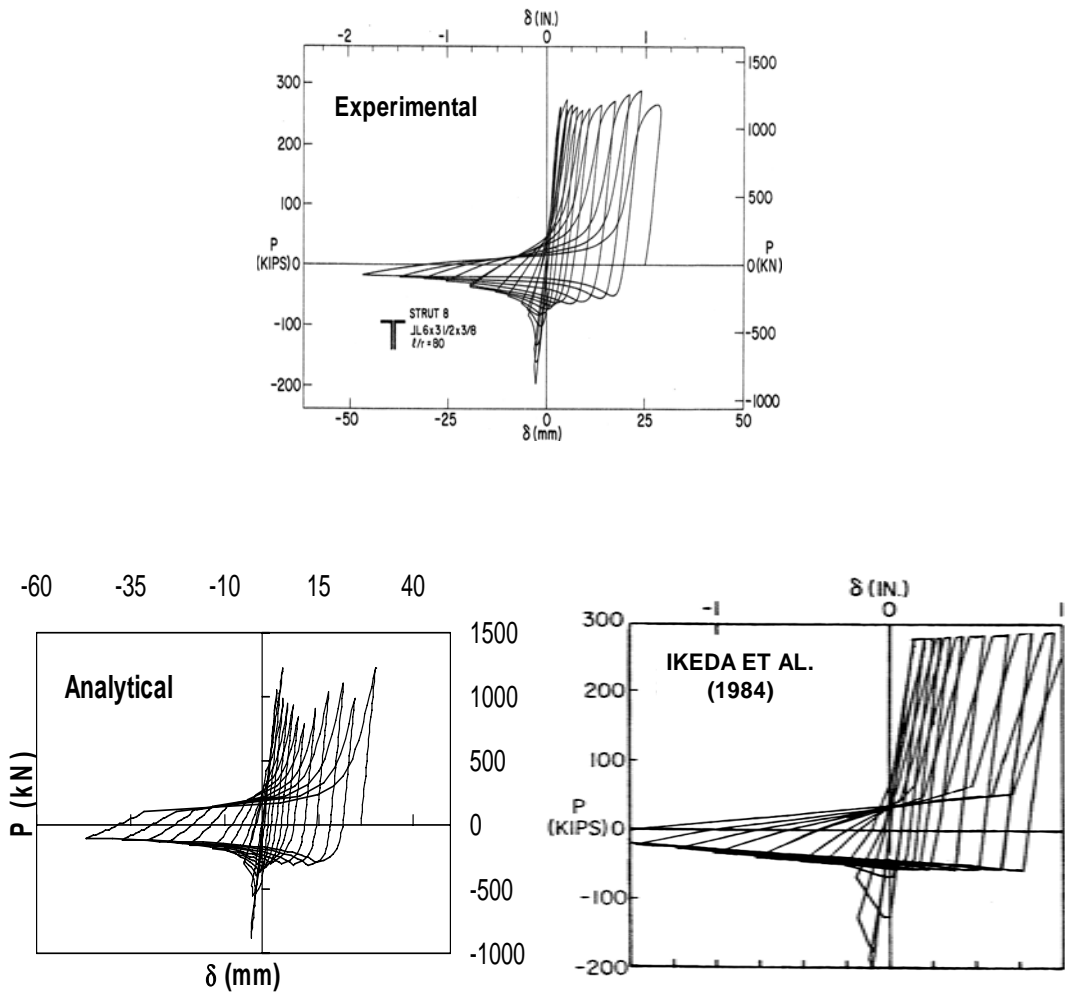


Fig. 5.34 Comparison of the proposed analytical model with the phenomenological model of Ikeda et al. (1984) and the test results of Black et al. (1980) for Brace 8

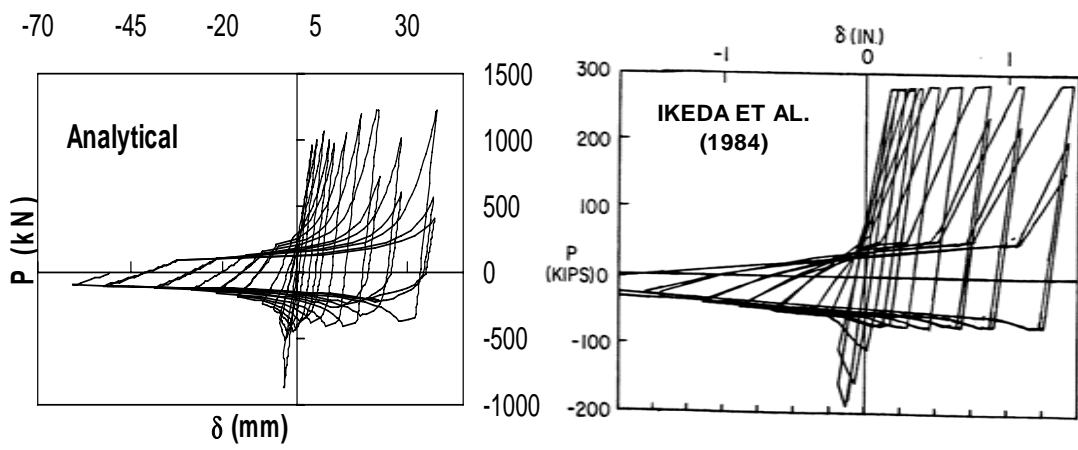
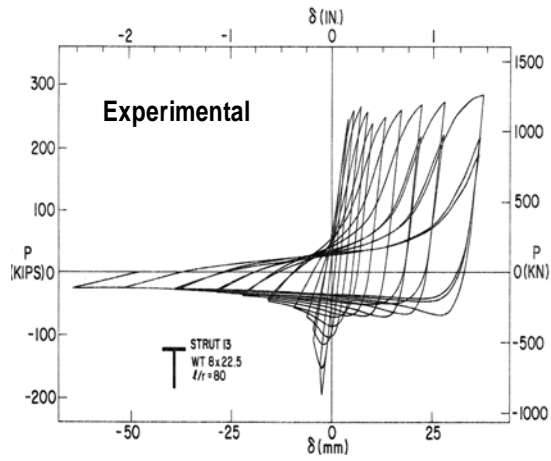


Fig. 5.35 Comparison of the proposed analytical model with the phenomenological model of Ikeda et al. (1984) and the test results of Black et al. (1980) for Brace 13

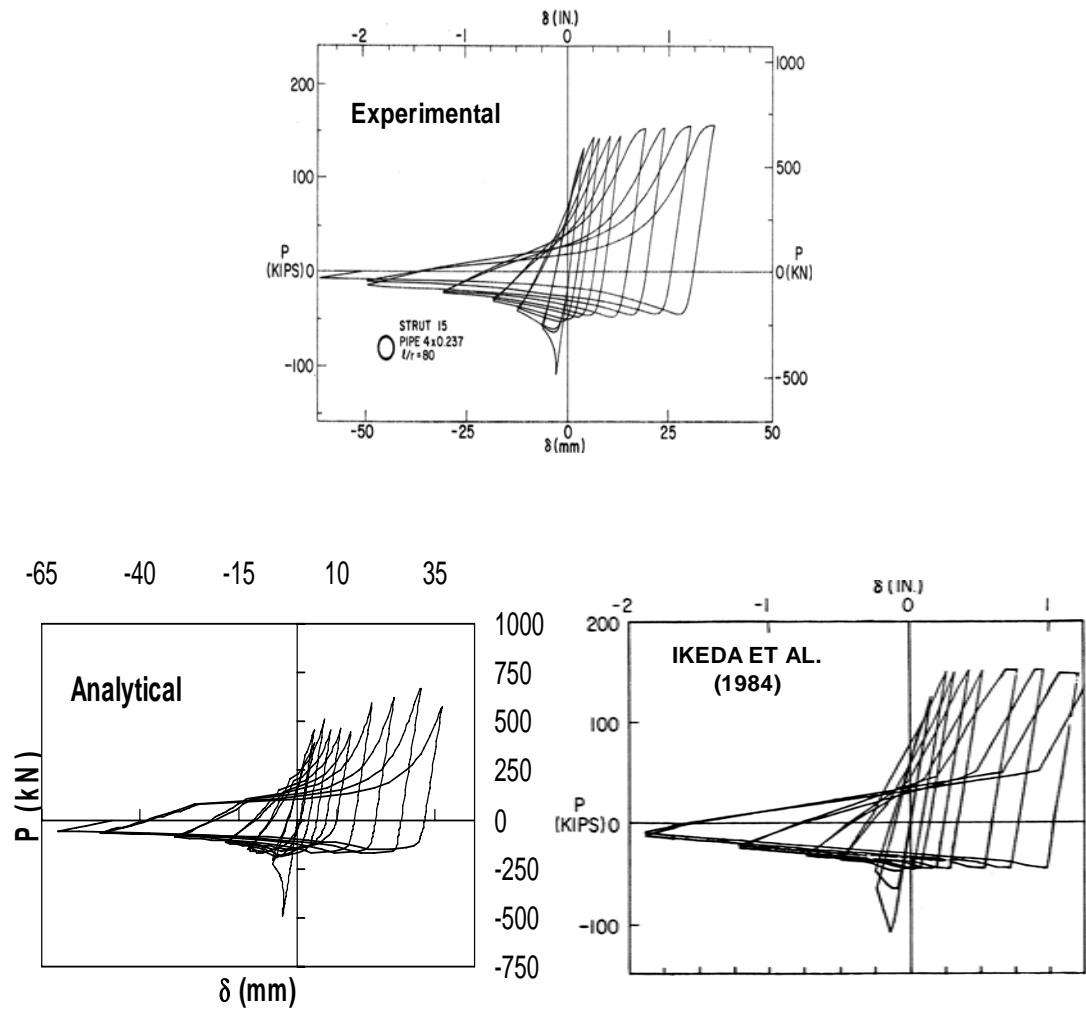


Fig. 5.36 Comparison of the proposed analytical model with the phenomenological model of Ikeda et al. (1984) and the test results of Black et al. (1980) for Brace 15

CHAPTER 6

CONCLUSION

This study presents a simple, yet an efficient and a universally applicable physical theory model that can be used to simulate the complex cyclic inelastic behavior of steel braces. Although, several analytical models have been developed for simulating the cyclic inelastic behavior of steel braces, most of these analytical models are either developed for a specific brace type or fail to account for certain inelastic behavioral characteristics such as degradation of the compressive load capacity, progressive lengthening of the brace called brace growth as well as the axial force - transverse displacement relationship of the brace. Moreover, some of the better analytical models are very difficult to use in practice as they involve numerous implicit parameters that require extra computations to define the cyclic inelastic behavior of a particular brace.

The developed model incorporates simplified theoretical formulations of the inelastic behavior of steel braces. In the analytical model, some semi-empirical techniques were used to account for the partial plastification (brace growth) and degradation of buckling capacity due to Baushinger effect. The analytical model developed in this study is verified by comparing the analytically obtained hysteresis loops with their experimental counterparts. Furthermore, in order to observe its capabilities compared to other existing models, the analytical model developed in this study is compared with the refined physical theory models of Ikeda and Mahin (1984) and Jin and El-Tawil (2003) as well as with the phenomenological model of Ikeda et al. (1984). Followings are the conclusions derived from this study;

- Based on the form of the analytical equations derived in this study to simulate the cyclic inelastic behavior of steel braces, it may be concluded that the developed analytical model is computationally more efficient than many existing models available in the literature. Furthermore, the developed analytical model is easier to use in practice than many existing models available in the literature since the input parameters of the model are based only on the geometric and material properties of the brace.
- The developed analytical model successfully accounts for brace growth and degradation of buckling capacity due to Bauschinger effect and residual kink present within the brace. Furthermore, different than the existing analytical models, the semi-empirical analytical equations developed to simulate the growth and Bauschinger effects in the proposed model are universally applicable to steel braces with various section types and slenderness ratios. This is achieved by correlating the experimental results to the geometric and structural properties of the brace using dimensional analysis techniques.
- The developed analytical model also accounts for the reduction in buckling capacity following an initial tensile yielding of the brace in relation to Bauschinger effect.
- The analytically obtained axial force – axial displacement as well as axial force – transverse displacement hysteresis loops compare reasonably well with the experimental ones.
- Comparing the results obtained from the analytical model developed in this study with the results obtained from the refined physical theory models of Ikeda and Mahin (1984) and Jin and El-Tawil (2003) as well as with the phenomenological model of Ikeda et al. (1984), it is observed that, in most cases, the proposed analytical model simulates the inelastic cyclic axial force-deformation behavior of braces better than those of the existing analytical models considered in this study.

REFERENCES

Black, R.G., Wenger, W.A.B. and Popov, E.P., (1980) "Inelastic Buckling of Steel Strut under Cyclic Load Reversals," Report No. UCB/EERC-80/40, Earthquake Engineering Research Center, University of California, Berkeley, CA.

Bruneau, M., Uang, C.M., Whittaker, A. (1998). Ductile design of steel structures. McGraw Hill, New York, NY.

Burden, L.R and Faires, L.D (2001), Numerical Analysis, Thomas Learning, USA

Dicleli, M., Mehta, A., (2007) "Simulation of Inelastic Cyclic Buckling Behavior of Steel Box Sections", Computers and Structures, Elsevier Science, Vol. 85 No. 7-8, pp. 446-457.

Fujimoto, M., Aoyagi, T., Ukai., Wada, A. and Saito, K., (1972) "Structural Characteristic of Eccentric K-Braced Frames," Transactions AIJ, No. 195

Fujiwara, T., (1979) "Earthquake Response of Framed Structures Having Aseismic Elements Part 1," Trans. of AIJ, 101-108, No. 285.

Fujiwara, T., (1980) "Seismic Behavior of Inelastic Member of Braced Frame Structure," Proc. of 7th World Conference on Earthquake Engineering.

Goel, S.C. and Hanson, C.R. (1974) "Seismic Behavior of Multistory Braced Steel Frames," ASCE, Journal of Structural Division, Vol. 100

Gugerli, H. and Goel, S.C., (1982) "Inelastic Cyclic Behavior of Steel Bracing Members," Report No. UMEE 82R1, Department of Civil Engineering, The University of Michigan, Ann Arbor, Michigan.

Higginbotham, A.B., (1973) "The Inelastic Cyclic Behavior of Axially-Loaded Steel Members," Dissertation, University of Michigan, Ann Arbor.

Ikeda, K., and Mahin, S.A (1984) "A Refined Physical Theory model for Predicting the Seismic Behavior of Braced Steel Frames" Report No. UCB/EERC-84/12, Earthquake Engineering Research Center, University of California, Berkeley, CA.

Ikeda, K., Mahin, S.A, and Dermitzakis S.N, (1984) "Phenomenological Modeling of steel Braces Under Cyclic Loading," Report No. UCB/EERC-84/09, Earthquake Engineering Research Center, University of California, Berkeley, CA.

Jain, A.K.,Goel, S.C., and Hanson, R.D., (1978) "Hysteretic Behavior of bracing Members and Seismic Response of Braced Frames with Different Proportions," University of Michigan Research Report UMEE 78R6, Ann Arbor

Jin,J., El-Tawil,S., (2003) "Inelastic Cyclic Model for Steel Braces," Journal of Engineering Mechanics, Vol. 129, No. 5.

Marshal, P.W, (1974) "Post-yiels Capacity of Tubuler Members," Presentation of the Column Research Council, Houston.

Nilforoushan, R., (1973) "Seismic Behavior of Multi-Story K-braced Frame Structures," University of Michigan Research Report UMEE 73R9, Ann Arbor, November.

Nonaka, T., (1973) "An Elastic-Plastic Analysis of a bar under Repeated Axial Loading," Int.J.Solids. Structures 9, 560-580 (Erratum in No.10, p.569).

Nonaka, T., (1977) "Approximation of Yield Condition for the Hysteretic Behavior of a Bar Repeated Axial Loading," Int. J. Solids Structures, Vol. B, 637-643.

Popov, E.P, (1999) "Introduction to Mechanics of Solids," New Jersey; Prentice-Hall

Popov, E.P, Black, R.G, (1981) "Steel Strut Under Severe Cyclic Loadings", ASCE, Journal of Structural Division, Vol.107

Remennikov,A.M, Walpole,W.R., (1997) "Analytical Prediction of Seismic Behavior for concentrically-Braced steel Systems," Earthquake Engineering and Structural Dynamics", Vol. 26 ,859-874.

Roeder,c.W., and Popov,E.P., (1977) "Inelastic Behavior of Eccentricallt Braced Frames Under Cyclic Loading," Report No. UCB/EERC-77/18, Earthquake Engineering Research Center, University of California, Berkeley, CA..

Singh,P., (1977) "Seismic Behavior of Braces and Braced Steel Frames," Dissetation, University of Michigan, Ann Arbor.

Sherman ,D.R., and Erzurumlu,H., (1976) "Ultimate Capacity of Tubular Beam-Columns," presented at the ASCE National Structural Engineering conference.

Soroushian,P., Alawa., M.S. (1990) "Hysteretic Modeling of Steel Struts:Refined Physical Theory Approach," Journal of Structural Engineering, Vol.111, No. 11.

Zayas,A.Z., Shing, P.B., Mahin, S.A and Popov,E.P., (1981) "Inelastic Structural Modelling of Braced Offshore Platforms for Seismic Loading," Report No. UCB/EERC-81/04, Earthquake Engineering Research Center, University of California, Berkeley, CA..

Wakabayashi, M., M., Shibata, M. and Masuda, H., (1971) "An Elastic-Plastic Analysis of a Brace Subjected to End Displacement," Annuals, Disaster Prevention Research Institute, Kyoto University, No.18b, 143-154

APPENDICES

DATA USED FOR THE GENERATION OF GROWTH FACTOR AND MODULUS ELASTICITY EQUATIONS

This appendix presents data used to calculate growth factor and modulus of elasticity equations for braces. The data is listed in Table. A1-A11

Table A1. Data for growth factor and degraded modulus of elasticity calculations for Brace 1

$\Delta_2-\Delta_b$	δ	δ_e	$n.\delta_e$	$\delta_i-\delta_{i-1}$	$n.(\delta_i-\delta_{i-1})$	$n(\Delta_2-\Delta_b)$	δ_p/δ_y	P_4	P_2	P_4-P_2	E_i/E	D_c
39.0	5.8	3.6	1.6	2.2	0.6	13.4		1375.0	-849.0	2224.0	0.4	19.5
59.0	8.1	3.4	2.4	2.3	0.8	20.3		1375.0	-670.0	2045.0	0.3	39.8
104.0	11.4	3.0	3.9	3.3	1.4	35.9		1340.0	-462.0	1802.0	0.2	75.7
144.0	16.6	2.8	6.0	5.2	2.1	49.7		1340.0	-358.0	1698.0	0.2	125.3
161.0	16.6	2.2	7.4	0.0	1.5	55.5		1050.0	-311.0	1361.0	0.1	180.8
195.0	24.4	2.6	9.3	7.8	1.9	67.2		1375.0	-226.0	1601.0		248.1
205.0	24.4	2.3	10.7	0.0	1.4	70.7		1210.0	-188.0	1398.0	0.1	318.7

Table A2. Data for growth factor and degraded modulus of elasticity calculations for Brace 2

$\Delta_2-\Delta_b$	δ	δ_e	$n.\delta_e$	$\delta_i-\delta_{i-1}$	$n.(\delta_i-\delta_{i-1})$	$n(\Delta_2-\Delta_b)$	δ_p/δ_y	P_4	P_2	P_4-P_2	E_i/E	D_c
53.7	5.3	3.4	1.6	1.9	0.6	16.3	0.9	927.0	-420.0	1347.0	0.3	21.4
69.7	6.3	3.0	2.1	1.1	0.5	21.1		898.0	-313.0	1211.0	0.2	42.5
91.7	8.2	2.8	2.9	1.9	0.8	27.8		890.0	-248.0	1138.0	0.2	70.3
117.7	9.7	2.7	3.6	1.5	0.7	35.7		897.0	-190.0	1087.0	0.2	106.0
138.7	11.2	2.7	4.1	1.5	0.6	42.0		925.0	-161.0	1086.0	0.2	148.0
155.7	12.7	2.7	4.7	1.5	0.6	47.2		946.0	-138.0	1084.0	0.2	195.2
182.7	15.8	2.7	5.8	3.1	1.1	55.4		981.0	-108.0	1089.0	0.2	250.5

Table A3. Data for growth factor and degraded modulus of elasticity calculations for Brace 3

$\Delta_2-\Delta_b$	δ	δ_e	$n.\delta_e$	$\delta_i-\delta_{i-1}$	$n.(\delta_i-\delta_{i-1})$	$n(\Delta_2-\Delta_b)$	δ_p/δ_y	P_4	P_2	P_4-P_2	E_t/E	D_c
85.7	7.1	5.5	1.3	1.6	0.3	9.2		1050.0	-310.0	1360.0	0.4	9.2
106.7	9.6	5.3	1.8	2.5	0.5	11.5		1050.0	-270.0	1320.0	0.3	20.7
161.7	13.4	5.0	2.7	3.8	0.9	17.4		1050.0	-193.0	1243.0	0.3	38.1
175.7	17.2	5.0	3.4	3.8	0.8	18.9		1050.0	-193.0	1243.0	0.3	57.0

Table A4. Data for growth factor and degraded modulus of elasticity calculations for Brace 4

$\Delta_2-\Delta_b$	δ	δ_e	$n.\delta_e$	$\delta_i-\delta_{i-1}$	$n.(\delta_i-\delta_{i-1})$	$n(\Delta_2-\Delta_b)$	δ_p/δ_y	P_4	P_2	P_4-P_2	E_t/E	D_c
67.43	6.4	5.82814	1.098121	0.57186	0.098121	7.045977		1050	-389	1439	0.45	11.4
93.43	9.4	5.556781	1.691627	3	0.593506	9.7628		1050	-322	1372	0.37	21.16
147.43	14	5.196319	2.694215	4.6	1.002588	15.40543		1050	-233	1283	0.35	36.2
212.43	21	5.018113	4.18484	7	1.490625	22.19749	0.705	1050	-189	1239	0.31	59.1
298.43	36	4.977612	7.232384	15	3.047544	31.18391	2.59	1050	-179	1229	0.28	92.87

Table A5. Data for growth factor and degraded modulus of elasticity calculations for Brace 5

$\Delta_2-\Delta_b$	δ	δ_e	$n.\delta_e$	$\delta_i-\delta_{i-1}$	$n.(\delta_i-\delta_{i-1})$	$n(\Delta_2-\Delta_b)$	δ_p/δ_v	P_4	P_2	P_4-P_2	E_v/E	D_c
135.79	12	4.787256	2.506655	7.212744	1.506655	6.718951		947	-235	1182		21.88
181.79	14.9	4.59285	3.244173	2.9	0.737518	8.995052		935	-199	1134		38.9
215.79	17.7	4.641451	3.813462	2.8	0.569289	10.67739		965	-181	1146		49.5
246.79	21.3	4.637401	4.59309	3.6	0.779627	12.21128		982	-163	1145		61.75
276.79	25.5	4.856108	5.251119	4.2	0.658029	13.6957	0.564356	1050	-149	1199	0.265	76
322.79	32	4.783206	6.690074	6.5	1.438955	15.9718		1050	-131	1181	0.25	92

Table A6. Data for growth factor and degraded modulus of elasticity calculations for Brace 7

$\Delta_2-\Delta_b$	δ	δ_e	$n.\delta_e$	$\delta_i-\delta_{i-1}$	$n.(\delta_i-\delta_{i-1})$	$n(\Delta_2-\Delta_b)$	δ_p/δ_v	P_4	P_2	P_4-P_2	E_v/E	D_c
50.87	5.3	5.116511	1.035862	0.183489	0.035862	2.969644		1220	-371	1591	0.71	4.93
79.87	6.7	4.727386	1.417274	1.4	0.381412	4.66258		1177	-293	1470	0.5	13.32
110.87	7.9	4.489409	1.759697	1.2	0.342423	6.472271		1163	-233	1396		19.8
135.87	9.2	4.363989	2.108163	1.3	0.348466	7.931699		1149	-208	1357	0.34	27.72
172.87	11.1	4.280375	2.593231	1.9	0.485068	10.09165		1156	-175	1331	0.33	37.72
180.87	14	4.302886	3.25363	2.9	0.660399	10.55867		1177	-161	1338	0.31	48.3
209.87	17.5	4.33183	4.039863	3.5	0.786234	12.25161		1206	-141	1347	0.31	60.53
230.87	20.3	4.338261	4.679294	2.8	0.63943	13.47752		1236	-113	1349	0.3	74
254.87	22.3	4.302886	5.182568	2	0.503274	14.87858	0.502755	1236	-102	1338	0.29	89.4

Table A7. Data for growth factor and degraded modulus of elasticity calculations for Brace 8

$\Delta_2-\Delta_b$	δ	δ_e	$n.\delta_e$	$\delta_i-\delta_{i-1}$	$n.(\delta_i-\delta_{i-1})$	$n(\Delta_2-\Delta_b)$	δ_p/δ_y	P_4	P_2	P_4-P_2	E_t/E	D_c
52.3	4.7	3.934626	1.194523	0.765374	0.194523	2.796791		935	-391	1326	0.57	4.63
86.3	6.4	3.42722	1.867403	1.7	0.67288	4.614973		870	-285	1155	0.46	9.24
100.3	9.1	3.548879	2.56419	2.7	0.696787	5.363636		943	-253	1196	0.43	14.6
145.3	12.5	3.418318	3.656769	3.4	1.092579	7.770053		957	-195	1152	0.4	22.37
193.3	17.2	3.566682	4.822409	4.7	1.165639	10.3369		1050	-152	1202	0.37	41.5
231.3	21.4	3.596355	5.950469	4.2	1.12806	12.36898		1090	-122	1212	0.37	53.87
272.3	25	3.617126	6.911564	3.6	0.961095	14.5615		1100	-119	1219	0.33	68.42
309.3	28.6	3.640864	7.855277	3.6	0.943713	16.54011		1122	-105	1227	0.31	84.96
342.3	33.2	3.715047	8.936631	4.6	1.081353	18.30481		1151	-101	1252	0.25	103.27

Table A8. Data for growth factor and degraded modulus of elasticity calculations for Brace 11

$\Delta_2-\Delta_b$	δ	δ_e	$n.\delta_e$	$\delta_i-\delta_{i-1}$	$n.(\delta_i-\delta_{i-1})$	$n(\Delta_2-\Delta_b)$	δ_p/δ_y	P_4	P_2	P_4-P_2	E_t/E	D_c
55.5	7.2	5.868116	1.22697	1.331884	0.22697	2.846154		1171	-411	1582	0.46	6.3
89.5	8.9	5.37107	1.657026	1.7	0.430056	4.589744		1135	-313	1448	0.41	9.15
127.5	10	4.859186	2.057958	1.1	0.400932	6.538462		1057	-253	1310	0.36	15.7
169.5	13.3	4.851767	2.741269	3.3	0.683311	8.692308		1107	-201	1308	0.27	24.4
185.5	17.3	4.948209	3.496214	4	0.754945	9.512821		1150	-184	1334	0.255	33.9
225.5	22.4	5.00014	4.479875	5.1	0.983661	11.5641		1193	-155	1348	0.255	45.45
268.5	28	4.989012	5.612334	5.6	1.132459	13.76923		1210	-135	1345	0.255	71.4
316.5	35	4.99643	7.005001	7	1.392667	16.23077		1238	-109	1347	0.25	102

Table A9. Data for growth factor and degraded modulus of elasticity calculations for Brace 13

$\Delta_2-\Delta_b$	δ	δ_e	$n.\delta_e$	$\delta_i-\delta_{i-1}$	$n.(\delta_i-\delta_{i-1})$	$n(\Delta_2-\Delta_b)$	δ_p/δ_y	P_4	P_2	P_4-P_2	E_v/E	D_c
115.97	7.2	6.478603	1.111351	0.721397	0.111351	8.265859		667	-194	861	0.49	25.47
124.97	11.6	6.328113	1.83309	4.4	0.721739	8.907341	0.398498	667	-174	841	0.47	34.8
177.97	16.2	6.124951	2.644919	4.6	0.811829	12.68496	0.637597	667	-147	814	0.45	48.11
250.97	23	5.869118	3.918817	6.8	1.273898	17.8881		667	-113	780	0.37	64.8

Table A10. Data for growth factor and degraded modulus of elasticity calculations for Brace 15

$\Delta_2-\Delta_b$	δ	δ_e	$n.\delta_e$	$\delta_i-\delta_{i-1}$	$n.(\delta_i-\delta_{i-1})$	$n(\Delta_2-\Delta_b)$	δ_p/δ_y	P_4	P_2	P_4-P_2	E_v/E	D_c
105.4	6.6	6.282966	1.050459	0.317034	0.050459	6.75641		642	-193	835	0.48	13.98
114.4	8.1	6.147525	1.2892	1.5	0.238741	7.333333		642	-175	817	0.4	21.32
152.4	10.7	5.951887	1.703017	2.6	0.413817	9.769231		642	-149	791	0.37	31.1
164.4	13.24	5.869118	2.107285	2.54	0.404268	10.53846		642	-138	780	0.355	41.624
222.4	17.8	5.83902	2.833057	4.56	0.725772	14.25641	0.358648	667	-109	776	0.335	56.238
245.4	23	5.763775	3.660692	5.2	0.827635	15.73077	0.239099	667	-99	766	0.31	72.2
305.4	27.9	5.568137	4.440578	4.9	0.779886	19.57692	0.537972	667	-73	740	0.31	92.32
310.4	33.4	5.3725	5.315961	5.5	0.875383	19.89744		667	-47	714	0.31	112

Table A11. Data for growth factor and degraded modulus of elasticity calculations for Brace 18

$\Delta_2-\Delta_b$	δ	δ_e	$n.\delta_e$	$\delta_i-\delta_{i-1}$	$n.(\delta_i-\delta_{i-1})$	$n(\Delta_2-\Delta_b)$	δ_p/δ_y	P_4	P_2	P_4-P_2	E_i/E	D_c
11.2	4.7	3.853567	1.219649	0.846433	0.219649	1.435897		485	-319	804	0.375	1.44
61.2	6.6	3.412611	1.934003	1.9	0.714354	7.846154		485	-227	712	0.325	10.16
72.2	7.6	3.326338	2.284795	1	0.350792	9.25641		485	-209	694	0.275	19.41
103.2	9.2	3.182548	2.890766	1.6	0.605971	13.23077		485	-179	664	0.25	32.64
113.2	11	3.134618	3.5092	1.8	0.618434	14.51282		485	-169	654	0.23	47.15
184.2	16.5	2.986035	5.525722	5.5	2.016522	23.61538		500	-123	623	0.2	97.8
199.2	20.2	3.043551	6.636984	3.7	1.111262	25.53846		519	-116	635	0.2	123.4
253.2	25	2.971656	8.412817	4.8	1.775833	32.46154		519	-101	620	0.195	155.8
299.2	30.5	2.909347	10.48345	5.5	2.070634	38.35897		519	-88	607	0.19	194.15
337.2	38	2.861417	13.28013	7.5	2.796681	43.23077		519	-78	597	0.19	237.4